INVESTIGATION
OF THE
FUNCTIONING OF A
LIQUEFIED-GAS MICRO-SATELLITE
PROPULSION SYSTEM

by

Robert Bernhard Weyer

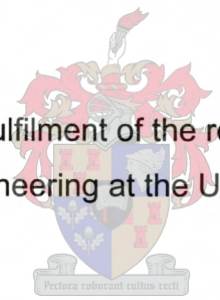

Thesis presented in partial fulfilment of the requirements for the degree
Master of Science in Engineering at the University of Stellenbosch

Thesis supervisor: R.T. Dobson

Thesis co-supervisor: K. van der Westhuizen

November 2003

DEPARTMENT OF MECHANICAL ENGINEERING

UNIVERSITY OF STELLENBOSCH

DECLARATION

I, Robert Bernhard Weyer, the undersigned, hereby declare that the work contained in this thesis is my own original work and has not previously, it its entirety or in part, been submitted at any university for a degree.

SUMMARY

The focus of this thesis is on the investigation of the functioning of a liquefied-gas thruster. Such a thruster could be used to provide secondary propulsion to a micro-satellite in orbit. A general overview of the need for thrusters in micro-satellites is put forward in the introduction. Motivation for deciding to investigate a liquefied-gas system is presented. Recent developments in the field of micro-satellites are discussed as well as their relevance to the project undertaken. Fundamental background theory relevant to the engineering problems associated with the development and analysis of such a system is also presented. Computer programs were written to simulate such a liquefied-gas thruster system. The experimental work carried out to analyse the system from a practical view-point is documented. Attention is also given to the measurement and calibration techniques used to obtain experimental data.

One-dimensional fully explicit transient mathematical models of the thruster system were developed to model the system using both compressed air and butane as propellants. These models were incorporated into computer programs used to simulate the transient behaviour of the system. Although it is intended to use butane as the propellant onboard a satellite, the reason for modelling and simulating a system using compressed air is because air is a convenient fluid to work with from both a theoretical and practical point of view.

An experimental model of a thruster system was designed, built and tested using air and butane as propellants. Most of the model was built using perspex to allow for the observation of the two-phase behaviour of the propellant inside the system. Locally purchased components were used for the solenoid and fill valves. Readily available butane lighter fluid was used for butane testing. Self-made heating elements were used to provide heat input to the propellant. Testing was done at different back pressures ranging from 100 kPa down to 20 kPa in a vacuum chamber.

Good comparison between theoretical and experimental results was obtained for air. Theoretical results for peak thrusts tended to over predict experimental results by

approximately 15 % for a system exhausting to a pressure of 100 kPa. Peak thrusts as high as 0.2 N were obtained for vacuum tests conducted at an absolute pressure of 20 kPa.

Peak thrusts of approximately 50 mN were achieved for experimental testing in atmospheric conditions using butane with a starting pressure of between 270 and 290 kPa. Typical average thrusts of between 20 mN and 30 mN were noted for butane testing with initial pressure of between 200 to 300 kPa. Peak thrusts of over 0.1 N were observed for vacuum testing at an absolute pressure of 20 kPa. An equation to correlate the experimentally determined average thrust as a function of pulse duration and starting pressure was developed. This correlated most of the experimental data to within ±25 %. Theoretical results for butane testing are able to predict peak thrusts within approximately 20 % for starting pressures in the range of 200 to 300 kPa.

Since the project was an exploratory investigation into a liquefied-gas thruster, some additional aspects relating to such systems were also given attention. The effect of liquid propellant motion or *sloshing* was considered and recommendations regarding the design and placement of the propellant tanks were made. The use of heat pipes as an alternative to electrical heating elements was investigated and some elementary design aspects are presented graphically. The management of the liquid propellant using surface tension devices was examined qualitatively.

Recommendations relating to future projects in the field of simple, low-cost propulsion systems for micro-satellites are put forward. More specifically these recommendations are with regard to: thermo-fluid modelling of the propellant, future experimental work to be done, techniques to measure small thrusts and vacuum chamber testing.

OPSOMMING

Die tesis ondersoek die funksionering van 'n vervloeidegas stuwer. So 'n stuwer kan gebruik word om sekondêre aandrywing aan 'n mikro-satelliet in 'n wentelbaan te verskaf. 'n Algemene oorsig oor die behoeftes van stuwers vir mikro-satelliete word voortgesit in die inleiding. Redes vir die gebruik van 'n vervloeidegas stuwer word bespreek. Onlangse ontwikkelinge in die veld van mikro-satelliet aandrywing word bespreek asook die toepaslikheid daarvan. Fundamentele teoretiese agtergrond verbonde aan die ontwikkeling en analise van so 'n stuwer stelsel word ook gegee. Rekenaarprogramme is geskryf om die gedrag van so 'n stuwer stelsel te simuleer. Eksperimentele werk is gedoen om die stelsel vanuit 'n praktiese oogpunt te analiseer. Aandag word ook gegee aan die metings- en kalibrasietegnieke soos toegepas vir die eksperimentele werk.

Eendimensionele volle eksplisiete wiskundige modelle is ontwikkel om die oorgangsgedrag van die stuwer-stelsel te simuleer met beide lug en butaan as dryfmiddel. Hierdie modelle is geïnkorporeer in die rekenaar programme om die stuwer stelsel te simuleer. Alhoewel dit beoog word om butaan as die dryfmiddel aan boord die satelliet te gebruik, is lug ook gebruik vir simulasie weens sy gerieflikheid as 'n vloeier uit beide 'n teoretiese en 'n praktiese oogpunt.

'n Eksperimentele model van die stuwer stelsel is ontwerp, gebou en getoets met beide lug en butaan as dryfmiddels. Die model is hoofsaaklik uit perspex gebou sodat die twee-fase gedrag van die butaan uitgebeeld kon word. Vrylik beskikbare butaan aansteker vloeistof is gebruik vir butaan toetsing. Selfvervaardigde verhittingselemente is gebruik om hitte aan die dryfmiddel te verskaf. Toetse is gedoen deur verskeie omgewingsdrukke varieërend van 100 kPa af tot 20 kPa in 'n vakuumtenk te gebruik.

Goeie ooreenstemming tussen die teoretiese en eksperimentele resultate vir die toetsing van lug is verkry. Die teoretiese resultate neig om die piek stukrag 15 % hoër te voorspel as die eksperimentele resultate vir 'n stelsel wat tot 'n omgewingsdruk van 100 kPa by die uitlaat. Piek stukragte van meer as 0.2 N is gekry vir vakuum toetse wat gedoen is by 'n omgewingsdruk van 20 kPa.

Tydens eksperimentele toetsing met butaan teen 'n aanvanklike druk tussen 270 en 290 kPa, in atmosferiese toestande, is piek stukragte van ongeveer 50 mN behaal. Tipiese gemiddelde stukragte van tussen 20 en 30 mN is waargeneem vir butaan toetsing teen 'n aanvanklike druk tussen 200 en 300 kPa. Piek stukragte van meer as 0.1 N is behaal vir vakuum toetse met 'n absolute druk van 20 kPa. 'n Vergelyking om die gemiddelde stukrag, wat eksperimenteel bepaal is, as 'n funksie van puls tydsduur en aanvanklike druk te korreleer, is ontwikkel. Die meeste eksperimentele data se afwyking van die korrelasie-vergelyking was minder as 25 %. Teoretiese resultate vir butaantoetse het piek stukragte binne 20 % van die eksperimenteel metings korrek voorspel vir aanvanklike drukke tussen 200 tot 300 kPa.

Weens die feit dat die projek 'n oorhoofse ondersoek in 'n vervloeidegas stuwer behels, is aandag ook gegee aan addisionele aspekte wat verband hou met sulke stelsels. Die effek van die vloeistof-dryfmiddel se onstabiele beweging in sy tenke is in ag geneem en voorstelle vir die ontwerp en plasing van die dryfmiddel tenke is gemaak. Die gebruik van hitte pype as 'n alternatief vir elektriese verhittingselemente is ondersoek. Verskeie ontwerp aspekte word grafies voorgestel. Die bestuur van die vloeistof-dryfmiddel deur van oppervlak spannings apparaat gebruik te maak, is kwalitatief ondersoek.

Voorstelle vir verdere navorsing in die veld van eenvoudige, lae-koste stuwer stelsels vir mikro-satelliete is gemaak. Meer spesifiek is hierdie voorstelle gerig op die termo-vloeidinamiese modellering van die dryfmiddel, verdere eksperimentele navorsing, tegnieke om klein stukragte te meet en vakuumtenk toetse.

ACKNOWLEDGEMENTS

The following people are thanked for their contributions towards this project, without which the completion of this project would not have been possible:

Robert Dobson – thesis supervisor

For your support, guidance and especially for your enthusiasm throughout the whole project and for helping me to "hang in there" when the going got tough.

Kobus van der Westhuizen – thesis co-supervisor

For your assistance with the measurement and control aspects and for persuading me to learn *LabVIEW*.

Cobus Zietsman – laboratory technician

For all the practical advice and "hands-on" assistance with the experimental work, but most importantly for your patience.

George Caroulissen – workshop artisan

For the manufacturing of the experimental apparatus, and for your patience and effort in attempting to understand my drawings.

DEDICATION

This thesis is dedicated to my parents to thank them for all their support, care and understanding shown to me throughout my life.

CONTENTS

NOMENCLATURE

Roman Symbols

A	Area [m^2]
A	Arbitrary variable
A	Arbitrary matrix
a	Speed of sound [m/s]
a	Constant in polynomials
a	Arbitrary vector
B	Arbitrary variable
b	Dimensionless constant
C	Constant
C	Effective exhaust velocity [m/s]
C_p	Constant pressure specific heat [J/(kg·K)]
C_v	Constant volume specific heat [J/(kg·K)]
D	Diameter [m]
d	Diameter [m]
d	Vector containing differences
E	Young's modulus of elasticity [N/m^2]
E	Energy [J]
f	Frequency [Hz]
f	Darcy friction factor
f	Function
F	Force [N]
g	Gravitational acceleration, 9.81 [m/s^2]
g	Vector of guessed values
H	Angular momentum vector
h	Enthalpy [J/kg]
h	height [m]
I	Impulse [N·s]
I	Moment of inertia [$kg·m^2$] or cross-sectional moment of inertia [m^4]
J	Bessel function
K	Strain gauge factor

K	Constant for fluid in analysing phase change
K	Wick permeability
K_P	proportionality constant
L	Length [m]
Ma	Mach number, V / a
M	Bending moment [N·m]
M	Molar mass [kg/mol]
m	Mass [kg]
m	Gradient
$\dot{m}$	Mass flow rate [kg/s]
p	Pressure [Pa]
$\dot{Q}$	Heat transfer rate [W]
R	Gas constant [J/(kg·K)]
R	Electrical resistance [Ω]
R	Thermal resistance
Re	Reynolds number, $\rho V d / \mu$
r	Radius [m]
T	Temperature [°C] or [K]
t	Time [s]
V	Velocity [m/s]
V	Voltage [V]
V	Volume [m^3]
$\mathcal{V}$	Volume [m^3]
u	Velocity in axial direction [m/s]
w	Deflection [m]
x	Mixture quality
x	Cartesian coordinate
y	Cartesian coordinate
z	Cartesian coordinate

Greek Symbols

β	Ratio of orifice to duct diameter

Δ	Difference
δ	Difference
ε	Strain
ε	Void fraction of wick
ε	Root of Bessel function of the first kind
σ	Stress [N/m^2]
σ	Condensation coefficient for fluid
σ	Surface tension
ρ	Density [kg/m^3]
λ	Body nutational frequency
π	Ratio circumference to diameter
ω	Natural frequency of vibration [rad/s]
ω	Angular velocity [rad/s]
γ	Specific heat ratio (= C_p/C_v)
θ	Hoop (circumferential) direction
θ	Arbitrary angle
θ	Nutation angle
μ	Viscosity
ν	Poisson's ratio
τ	Fluid shear stress at wall [N/m^2]
ζ	Damping ratio

Superscripts

*	Critical
T	Transpose of a matrix or vector

Subscripts

ad	Adiabatic
B	Back
CG	Constant group
c	Condenser
cap	Capillary
conv	Convection

D	Rearward resultant of external forces
E	East
e	Exit
e	Electrical
eff	Effective
f	Final
g	Gas
g	Gravitational
i	Inner or initial
l	Liquid
max	Maximum
norm	Normal
NP	Net propulsive
o	Stagnation condition, orbit or outer
p	Propellant
R	Restraining
RF	Rearward force
r	Radial
s	Spin or surface
sat	Saturated
sp	Specific
sub	Subsonic
sup	Supersonic
t	Throat or Transverse
T	Thrust measured in a test bench
v	Vapour
W	West
w	Wall or Wick
z	Axial

Dimensionless Variables (Roman)

c	Beam constant, $\sqrt{EI/\rho A}$
Bo	Bond number, $\rho g r_o^{\,2}/\sigma$

Ff	Fill fraction of tank
Fr	Froude number, $\omega^2 r_o / g$
k	constant relating friction factor, length and diameter, $f L / d$

Dimensionless Variables (Greek)

α	Amplification factor, $1/(1-K_P/(I_{xx}(\sigma-1)))$
β	Beam constant, $\sqrt[4]{\rho A \omega^2 / E I}$
σ	Inertia ratio, I_{yy} / I_{xx}

Abbreviations

CFD	Computational fluid dynamics
CV	Control volume
DAQ	Data acquisition
FE	Finite element
FEM	Finite element method / model
HAN	Hydroxyl ammonium nitrate
I/O	Input / output
LEO	Low earth orbit
MEMS	Microelectromechanical system
PC	Personal computer
PVC	Poly vinyl chloride

Notation

$\dot{x}$	Differentiation once with respect to time
$\ddot{x}$	Differentiation twice with respect to time
x'	Differentiation once with respect to length
x'	New x-axis
x''	Differentiation twice with respect to length
x'''	Differentiation three times with respect to length

LIST OF FIGURES

LIST OF TABLES

1 INTRODUCTION

Secondary propulsion systems on satellites refer to propulsion applied to the satellite whilst in its orbit. Such systems can be used on micro-satellites for orbit lifting, speed adjusting, gravitation compensation, station-keeping and attitude control (Zakirov et al. 2001). Orbit maintenance is also necessary as atmospheric drag can have a drastic effect on a satellite's orbit and can lead to orbit decay, which can result in the satellite re-entering the earth's atmosphere – as did the Skylab satellite in the late 1970s (Garrison and Stocky, 1988). Such propulsion systems are a common feature on virtually all larger geostationary satellites.

However, until recently small low-earth orbit (LEO), low-cost micro-satellites have flown without propulsion systems. For example: of the 19 small LEO satellites launched by the University of Surrey up until June 2001 only 2 of the 19 were equipped with propulsion systems, i.e. just over 10 %. However, this trend is expected to change and most future small spacecraft will contain propulsion systems (Gibbon and Underwood, 2001). Recent pioneering small satellite missions have ventured beyond experiments and have proved that high quality satellite imaging can be provided on a regular basis. The requirement for "frozen" orbits, with optimum lighting and atmospheric conditions in the area of regard have created a demand for low-cost effective secondary propulsion systems. If reliable, accurate systems can be developed at a low cost, proposed concepts of satellite clusters will become more feasible.

Traditionally, secondary propulsion requirements for LEO satellites have been fulfilled by cold gas systems in which the propellant is typically nitrogen stored at a very high pressure (in the order of 200 MPa) or hydrazine. Recently, attention has been given to the development of liquefied-gas thrusters (Gibbon and Underwood, 2001, Mukerjee et al., 2000 and Ye et al., 2001) where the propellant is stored in liquid phase, vaporised and expelled as a gas. The aim of this project is to investigate the functioning of a liquefied-gas thruster that could be used to provide secondary propulsion for a micro-satellite. The advantages of liquefied-gas systems are that they require minimal storage volume (micro-satellites are usually more constrained by volume than by mass) and the propellant does not need to be stored at a very high

pressure (when compared to systems where the propellant is stored as a compressed gas). An example of such a system, using butane as propellant, has already been space-proven by the University of Surrey on a nano-satellite and was shown to be simple, reliable and cost effective.

The performance of a thruster can be characterised by many different parameters such as thrust produced by the system, specific impulse achieved with the propellant, heating power required to vaporise the liquid propellant, duration for which a constant thrust can be maintained, mass and volume requirements of the system, pressures at which the propellant will be stored at and the financial cost of the system. Some values of these performance parameters achieved by the University of Surrey (Gibbon and Underwood, 2001) are known. Where possible the results obtained in this project will be compared to those obtained by the University of Surrey.

It is also intended to investigate a number of various other aspects relating to the design, development and testing of a liquefied-gas micro-satellite thruster system. These include the problem of sloshing of the liquid propellant, use of a heat pipe to provide heating power to the propellant and methods to measure the thrust delivered. It is expected that the experimental work will provide a starting point for gaining experience in the practical aspects of the construction of a thruster system.

At this stage no specifications will be laid down for mass, volume and power requirements of the system as this would require a detailed survey (and possible testing) of current products available, which is beyond the scope of this project. Cost estimations for the construction and testing of a thruster system will also not form part of this project.

2 OVERVIEW OF PREVIOUS WORK (LITERATURE STUDY)

A number of articles documenting secondary propulsion systems in small satellites were reviewed with the objective of gathering a base of information to be used in the design, analysis, testing and evaluation of a liquefied-gas butane propulsion system. Articles dealing specifically with liquefied-gas butane systems were given the most attention due to their obvious relevance to the project. In addition articles dealing with liquefied-gas systems using water as propellant were also reviewed. A number of the articles reviewed presented a more general overview of the design philosophy for propulsion systems. Articles focussing on practical aspects relating to experimental work (specifically thrust measurement methods and vacuum chamber testing) were reviewed. Finally, brief attention was given to promising modern propulsion technologies (in particular MEMS technology and plasma thrusters) that are beginning to establish themselves as viable options.

2.1 Design of Secondary Propulsion Systems

Zakirov et al. (2001) focus on the constraints and requirements of micro-propulsion systems. In addition attention is given to some of the performance characteristics and parameters that can be used when comparing different propulsion systems. A new modified form of the classical rocket equation is presented. The "system-specific impulse" I_{ssp} is suggested as a propulsion system performance parameter. The authors believe it to be a more accurate determination of the spacecraft propulsion performance parameter than the "thruster-specific impulse" I_{sp} used traditionally, since system-specific impulse takes into account the mass of the entire thruster system – i.e. accounts for the mass of components and propellant, whereas "thruster-specific impulse" only accounts for the mass of the propellant. These authors compared a number of current technologies against each other using some of the performance parameters discussed previously in the article. They conclude with a discussion on selection criteria for micro-satellites. The list of selection criteria is as follows:

- Space vehicle velocity change requirements
- System-specific impulse

- Propulsion envelope volume requirements
- Power requirements
- Cost
- Propellant storability, non-toxicity, non-flammability, non-explosiveness, compatibility and availability
- Restartability in orbit (if required)

Although these researchers recommend the use of liquefied gases as propellants for small satellites, they highlight a few of the difficulties associated with the application of liquefied gases. These are:

- Countermeasures are required against the liquid sloshing inside the tank
- Heat (power) is required to realise the phase change (latent heat)
- Self-pressurising systems can only support limited a propellant flow

Hansen (1999) gives a brief review of the need for onboard propulsion of a micro-satellite. It is also intended as a student project and outlines the typical steps and stages that a student undertaking such a project would have to consider. The article recommends the consideration of the following two substances as propellant: hydrogen peroxide (H_2O_2) and hydroxyl ammonium nitrate (HAN). Both of these substances are fairly low-toxic and non-flammable. The article suggests thrusts in the order of 10 to 100 mN for attitude control.

The article concludes by listing and briefly describing the steps that would be taken in carrying out their project. The steps listed are:

- Chemistry / catalyst (since the author is also considering thrusters that make use of chemically reacting propellants this is more relevant to their cause)
- Fluid mechanics – designing 2 types of thrusters (one for attitude control (0.01 to 0.1 N) and one for orbit control (1 to 10 N), design of a pressurised propellant feed system and design / selection of micro-valves for controlling thrusters (operating frequencies of valves in the range of tens of milliseconds are mentioned)
- Materials technology
- Control and monitoring – mention is made of commercially available equipment using remote radio control / monitoring systems. A sun-tracking

sensor is also mentioned. However, no attention is given to methods of measuring thrusts.

Cardin and Acosta (2000) discuss the design and testing of a cold-gas propulsion system for small satellites. The working gas used in the system is nitrogen. The pressure at which the nitrogen is stored is fairly high – 207 bar. Thrusters are designed to provide thrust of 0.5 N at 21 bar inlet pressure. At 207 bar inlet pressure approximately 5 N of thrust is delivered. Attention is given as to how thrusters should be positioned on a satellite when conducting manoeuvres – ideal orientation to minimise propellant and power requirements. Of interest is the system testing that the thrusters must be subjected to as part of safety regulations. Twelve check points are given without much detail as to what the checks actually involve. No details are given as to how to go about determining the actual thrust delivered. Most of the testing is effectively a quality control check to ensure that all components are functioning properly.

Gibbon et al. (2000) focus on the development of the butane liquefied-gas system developed at Surrey for use on the SNAP-1 nano-satellite. In general it is very similar to Gibbon and Underwood's (2001) article referenced in section 1 and discussed later in section 2.2. However, it does go into somewhat more technical detail such as the engineering specifications and the actual components used.

Thruster units incorporating MEMS components are discussed by Köhler et al. (2002), Bayt et al. (1997), Youngner et al. (2000) and Rhee et al. (2000). Köhler et al. (2002) discuss a hybrid cold gas microthruster system in which MEMS units are served by external electronics. Bayt et al. (1997) focus on the modelling, design and testing of micron scale Laval nozzles. Younger et al. (2002) investigate MEMS mega-pixel micro-thruster arrays in which a single thruster array contains a quarter of a million separate thrusters on a 33 mm by 33 mm silicon die. Each thruster has its own heater element which is co-axially aligned to a hollow fuel-filled cavity directly above it. Rhee et al. (2000) discuss the development of a mono-propellant thruster using hydrogen peroxide. Attention is given to the design and development of the of the micro-scale reactive catalyst necessary for the decomposition of the hydrogen peroxide.

2.2 Butane Thruster Systems

Gibbon and Underwood (2001) document the design and development of a butane propulsion system for a small satellite. Their main focus is on the in-orbit performance of the system used on the SNAP-1 nano-satellite. This system was space-proven in June 2000 when it was successfully used on a nano-satellite SNAP-1 (mass $\approx$ 6.5 kg). The system was equipped with 32.6 grams of butane, and succeeded the spacecraft's semi-major axis by over 3 km at a nominal orbit height of 625 km. The advantages of using butane as a propellant are:

- It can be stored as a liquid with a relatively high storage density
- It has a very low storage pressure (2 bar at 20 °C – and requires no pressure regulation
- Low power requirements to operate valves
- Low toxicity – reduces handling considerations, and the drawbacks are:
- Slightly lower specific impulse than nitrogen (the propellant traditionally used for micro-thrusters)
- The butane must be expelled as a vapour – a phase change must occur which requires heating
- It is highly flammable

The article describes the system and the components used in that system. Notable features are:

- The use of a 3/8" (9.52 mm) titanium pipe with a total storage volume of 65 cm^3 to store the butane, thus eliminating the use a qualified tank
- A 15 Ω resistor to heat the butane just before the nozzle entry
- Use of commercially available space qualified valves for the fill valve and solenoid valve
- The heater was switched on approximately 2 - 3 minutes before thrust commenced

The performance of the thrusters is discussed. The main results are that the sequence of firings was effectively able to raise the orbit of SNAP-1 by between 3.1 and 3.4 km – atmospheric drag effects taken into account. This related to an effective ΔV of

between 1.9 and 2.1 m/s – or a mission specific impulse of 43 s. The effective thrust was calculated to be 46 mN.

Notable differences are clear when comparing data from earlier and later firings:

- During early firings the butane was typically at a pressure of 1.6 bar and a temperature of 9 °C. After 2 minutes of heating the temperature and pressure rose to 24 °C and 1.88 bar. Simple calculations using Boyle's law as if vapour alone where being heated would give an expected pressure of 1.65 bar – much lower than the actual pressure rise. This would suggest that there is liquid boiling near the outlet causing this high pressure rise.
- Data is also presented of the last firing to be performed whilst there was still liquid left in the system. Prior to this firing the pressure and temperature in the tank were 1.8 bar and 17 °C. Both are significantly higher that what they were during the early firing. During the 3 minutes of heating the temperature increased to 42 °C, whilst the pressure only increased very slightly to 1.85 bar. After this firing only vapour remained and the pressure did not show its usual recovery.
- Data for a firing in the mid-life of the system is also presented. The conditions before firing were 9 °C and 1.62 bar. During the first 2.5 minutes of heating the pressure rose very slowly – an indication of vapour at the valve inlet. This was followed by a sudden increase in pressure coupled with a sudden temperature reduction. It is believed that this was due to a globule of butane floating near the valve. When the liquid touched the warm wall it would have vaporised rapidly – hence the pressure increase. The drop temperature would have been due to the energy required to vaporise the butane – which would have been drawn from the wall.

A plot of height gained against cumulative firing duration showed a steeper curve during the first 20 seconds of firing, after which the gradient decreases. This indicates that initially the spacecraft gained more altitude per second of firing than later. The likely reason for this was that some liquid phase propellant was being expelled – leading to a greater mass flow rate. This speculation is supported by plots of temperature and pressure that suggested that there was liquid butane near the manifold. It was estimated that in the region of 30-40% of the propellant was

expelled in liquid form. The conclusion drawn from this is that propulsion system had insufficient ullage (amount by which container under-filled) at the start of the mission.

A number of improvements are recommended for future butane thruster systems. One of the main challenges is to ensure that no liquid phase butane is expelled. Measures that could be taken are to ensure larger ullage at start of mission, increase heater power and design system layout such that liquid propellant settles away from tank outlet. The micro-thruster system described was for use on a very small satellite weighing only 6.5 kg. Surrey Space Centre intends to builds bigger satellites (100 kg) incorporating a butane propulsion system similar to that used on SNAP-1. The major changes recommended are:

- To dispense with the coiled tube arrangement and to make use of conventional tanks, and
- To perform the heating in a separate thrust chamber assembly, rather than to just heat the nozzle.

2.3 Thrust Measurements

The article by Ye et al. (2001) focuses on a micro-thruster using water as the propellant. The thruster is fabricated using MEMS technology and in general the technical aspects of the thruster that are discussed are not that relevant to this project as MEMS technology is not available locally. In addition Ye et al. (2001) describe the method used to measure the thrust delivered. The method used was to mount a cantilever beam with the free end aligned to the thruster. The displacement of the free-end of the beam was measured and recorded using a laser Doppler vibrometer. Typical parameters for which test results are given are a pulse width of 900 μs which is pulsed with a frequency of 30 Hz. However, the maximum thrust measured was only 2.9 μN. These thrust levels are too low for the application investigated in this thesis, but could be useful for differential drag correction during formation maintenance in LEO.

Mukerjee et al. (2000) focus on a thruster manufactured using MEMS technology. Results are given for the thruster using water as the working fluid. The article does

give details on the method used to measure the thrust. A force transducer and a fulcrum to determine the thrust delivered was used. The thrusts measured were typically in the order of 0.2 N. The thruster technology in this article is more "promising future technology" as opposed to "space proven technology" as at the time of publication the system had not yet been flown in space and the authors also mention that future work on chamber geometry, nozzle geometry and fuel choices will be done to optimise the system.

The thruster type considered by Ziemer et al. (1997) is a pulsed plasma thruster. The technical details of the thruster are very complicated but the article does give some details of the method used to measure the impulse produced. A *swinging-gate* was used to measure the thrust. Testing was done in a vacuum chamber. The measurement basically works by mounting the thruster in such a way that it can vibrate around a shaft and then when a pulse is produced the thruster will rotate. The angle through which the thruster rotates is monitored and this information is used to determine the impulse that must have been delivered by the thruster in order to cause the measured rotation.

Toyoda et al. (2001) report on results for the performance of a continuous-wave carbon dioxide laser thruster. Although this type of thruster considered is not relevant to the project, details regarding the thrust measurement are given. Thrust was measured by mounting the thruster on a small trolley with wheels. This trolley was connected to a load cell, and hence by measuring the force in the load cell the thrust was determined.

2.4 Thruster Procurement Requirements

In this section a draft specification for the design of a thruster system for a micro-satellite is considered (Muller, 2003).

A system schematic is required indicating the basic system layout, and containing details relating to the number and location of thrusters, number of propellant tanks, fill valves and other major components inherent to a thruster system. In deciding upon the number of thrusters and related components, attention must be given to

redundancy requirements – i.e. how many "spare" components will be available in the system? How will these spare components be incorporated? Attention to contamination restrictions affecting the system is required. An example of such a contamination restriction is the possibility of the plume geometry contaminating a camera lens on board the satellite. Leakage of the propellant is another contamination restriction.

The total impulse required from the thruster system must be calculated, based on the "delta-V" budget. Specific levels of thrust required must be decided upon. Thrust levels should be specified by force profiles indicating rise time, steady thrust and tail-off, as well as the tolerances and repeatability of these thrust levels. The use of heating to increase thrust levels can be considered. This is especially true when a liquefied-gas is used as propellant. The maximum continuous thrust period required is the key factor in determining the maximum heating input required. The shortest required thrust pulses need to be specified as they will be limited by the response times of the valves chosen. Targets for the maximum acceptable leakage rate of the propellant must be set as they will influence the design and purchase of components such as propellant tanks, piping, seals and valves. Propellant slosh in the propellant tank and piping must be considered as it can affect the design and placement of the propellant tank and piping. Finally, attention must be given to safety requirements of the thruster system.

A thuster system comprises many different components that interact with the rest of spacecraft. Consideration must be given to the mass and volume of all components and their contribution to the mass and volume budgets. The electrical components and the requirements that they place on the on-board energy resources must be taken into account. Examples of this are voltage requirements for control of valves and power requirements for propellant heating. The electronic circuitry required by sensors and valve drive electronics must fit in with the rest of the satellite's electrical system. In addition contamination effects of electro-magnetic fields generated by solenoid valves on other electronic circuits requires consideration.

The environment that the system could be exposed to and required to function under, must be known. This could be exposure to shock, vibration, and thermal effects.

Testing of individual components as well as of systems consisting of these components requires consideration. Examples of testing would be proof pressures, electrical systems, leakage, performance and environmental testing. Environmental testing refers to testing the ability of the system to withstand exposure to vibration, shock and thermal effects.

Proper standards of documentation, design and delivery reviews form part of the product assurance of a thruster system. A statement of work containing a programme schedule, hardware deliverables and documentation deliverables must also be defined.

3 THEORETICAL BACKGROUND

This section presents the background engineering fundamentals used in attempting to numerically simulate a thruster system. The fundamentals of propulsion are presented in section 3.1. The idealised gas dynamic theory required to calculate the values needed for the equations in section 3.1 are presented in section 3.2. The thruster system used a liquefied-gas as propellant and theory used in modelling the phase-change phenomena can be found in section 3.3. Details regarding the use of surface tension devices to manage liquid propellant heat transfer and flow are given in section 3.4. The development guidelines for the development of a micro-satellite thruster are given in section 3.5, and finally, the phenomena of propellant sloshing and its effect on the satellite are discussed in section 3.6.

3.1 Propulsion Fundamentals

Consider the simplified diagram in Figure 3.1 depicting a simplified rocket motor (Larson and Wertz, 1992).

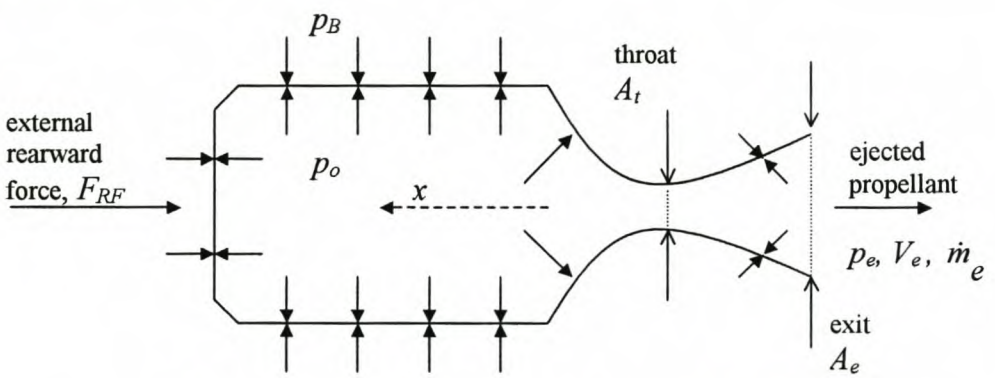

Figure 3.1 Schematic diagram of a simplified rocket motor

Figure 3.1 depicts a simplified rocket motor where the propellant at pressure p_o is being ejected against the back pressure p_B, at a mass flow rate of $\dot{m}_e$ and velocity V_e. In space p_B is essentially zero since there is no atmosphere. The rearward external forces acting on the rocket are denoted by F_{RF}. Applying the Reynolds transport theorem to the control volume in Figure 3.1 for the linear momentum in the x-direction yields:

$$p_e A_e + p_B A_B - F_{RF} = \frac{d}{dt}\left(\int_{\mathcal{V}} (\rho V) d\mathcal{V}\right) - \dot{m}_e V_e \tag{3.1}$$

where the first term on the right hand side of equation 3.1 represents the change in *x*-momentum in the control volume due to unsteady flow and can be replaced with $\frac{d}{dt}(mV)$, which using the product rule for differentiation can be expressed as $\dot{m}V + m\dot{V}$ where m and V denote the mass and velocity of the rocket respectively. The rate of change of the rocket $\dot{m}$ is equal to $-\dot{m}_e$. Hence equation 3.1 can be written as

$$m\dot{V} - \dot{m}_e V = \dot{m}_e V_e + p_e A_e - F_D \tag{3.2}$$

where $F_D = F_{RF} - p_B A_B$ is the rearward resultant of external surface forces. A_B is the difference between the total cross sectional area of the rocket and the exit area of the nozzle. The net propulsive force acting on the rocket F_{NP} is equal to the mass of the rocket times its acceleration, hence

$$m\dot{V} = \dot{m}_e V_e + p_e A_e + \dot{m}_e V - F_D = F_{NP} \tag{3.3}$$

In a bench test, in which the rocket is constrained from moving, the velocity of the rocket would be zero, i.e. $V = \dot{V} = 0$. The rearward resultant of external surface forces is equal to the measured thrust F_T plus the pressure force of the back pressure acting over the exit area, i.e. $F_D = F_T + p_B A_e$. Substituting the value for V and the expression for F_D into equation 3.3 and rearranging yields the following expression for the measured thrust F_T:

$$F_T = \dot{m}_e V_e + A_e(p_e - p_B) \tag{3.4}$$

This expression may be simplified by defining an *effective exhaust velocity* C

$$C \equiv V_e + \frac{A_e}{\dot{m}_e}(p_e - p_B) \tag{3.5}$$

Hence, equation 3.4 may be reduced to

$$F_T = \dot{m}_e C \tag{3.6}$$

The primary measure of propulsion performance system capability is the velocity change ΔV that it can produce. ΔV is given by the ideal rocket equation (Larson and

Wertz, 1992) and can easily be derived by considering equation 3.3. The mass of the rocket at time t is $m(t)=m_i-\dot{m}_e t$, where m_i is the initial mass of the rocket at time equal to zero. Hence equation 3.3 can be written as:

$$(m_i-\dot{m}_e t)\frac{dV}{dt}=F_{NP} \tag{3.7}$$

Equation 3.7 can now be rearranged as follows:

$$dV=\frac{F_{NP}}{m_i-\dot{m}_e t}dt \tag{3.8}$$

If F_{NP} and $\dot{m}_e$ are constant then the change in velocity, $\Delta V = V_f - V_i$, can be determined by integrating equation 3.8 from time zero to the final time t_f:

$$\Delta V=V_f-V_i=-\frac{F_{NP}}{\dot{m}_e}\ln\left(\frac{m_f}{m_i}\right)=\frac{F_{NP}}{\dot{m}_e}\ln\left(\frac{m_i}{m_f}\right) \tag{3.9}$$

A commonly used measured of rocket performance is specific impulse I_{sp}. I_{sp} is the ratio of thrust to the weight flow rate $\dot{m}_e g$ of the propellant. It is a measure of the velocity change that a rocket can produce and is given by

$$I_{sp}=\frac{F_{NP}}{\dot{m}_e g} \tag{3.10}$$

Expressing equation 3.9 in terms of I_{sp} gives the classic rocket equation

$$\Delta V=g\,I_{sp}\ln\left(\frac{m_i}{m_f}\right) \tag{3.11}$$

It must be borne in mind that equation 3.11 is idealised as it assumes zero losses due to atmospheric drag and gravity losses. The actual ΔV realised will be smaller than that predicted by equation 3.11.

However, for this project the only thrust that will be worked will be dealt with is F_T, the thrust measured in a test stand, and equation 3.11 is derived and presented for the sake of thoroughness. For purposes of this project the equation for specific impulse (equation 3.10) will be adjusted as follows

$$I_{sp} = \frac{\overline{F}_T}{\frac{\Delta m}{\Delta t} g} = \frac{\left(\int_o^t F_T dt \right) / \Delta t}{\frac{\Delta m}{\Delta t} g} \tag{3.12}$$

In order to predict the thrust using equation 3.4 the values of p_o, p_B, A_e and A_t will generally be known. Hence, it is necessary to determine $\dot{m}_e$, V_e and p_e. Unfortunately, the calculation of these values is fairly complicated. The methods used to determine $\dot{m}_e$, V_e and p_e are obtained from gas dynamic theory, which is dealt with in more detail in section 3.2.

3.2 Idealised Gas Dynamics

As mentioned in section 3.1, in order to compute the thrust it is necessary to be able to calculate the following exit properties: $\dot{m}_e$, V_e and p_e for use in equation 3.4. This section will present traditional gas dynamic theory (Anderson, 1990 and White, 1999). Simplified gas dynamics assumes a reservoir of gas that remains at constant pressure and temperature. The fluid velocity in the reservoir is assumed to be sufficiently low enough to regard the pressure and temperature as stagnation values p_o and T_o. A schematic layout of the problem to be solved is presented in Figure 3.2. Gas at stagnation conditions p_o and T_o flows through a nozzle (throat area A_t, exit area A_e) to a back pressure p_B. The exit conditions are V_e, p_e and T_e must be calculated.

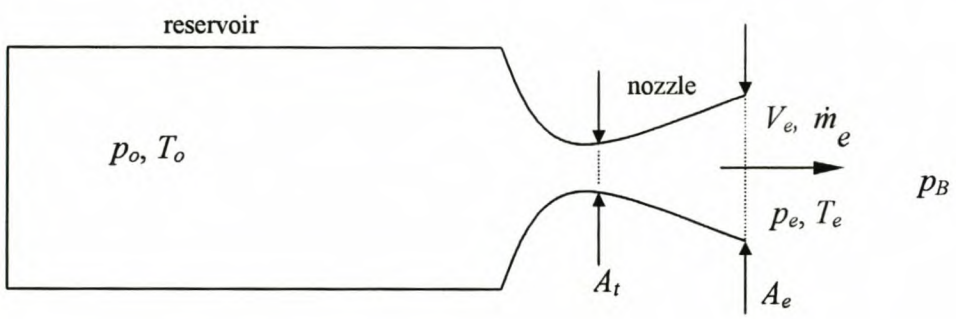

Figure 3.2 Sketch of a reservoir and nozzle

Simpliefied theory also makes the following assumptions regarding the flow of the fluid through the nozzle:

- the gas behaves as an ideal gas
- the gas is calorically perfect
- the flow is frictionless
- the flow is isentropic
- the flow is "frozen", i.e. no change (chemically) occurs after leaving the stagnation condition at the nozzle throat

An *ideal gas* is a gas whose properties (pressure p, temperature T and density ρ) can be described by the relation $p=\rho RT$, where R is a constant for a particular gas. The enthalpy h of a *calorically perfect* gas is a linear function of temperature only, i.e. $h=C_p\left(T-T_{ref}\right)$ where C_p is the specific heat at constant pressure and is a constant and T_{ref} the reference temperature. If the above assumptions can be made then the following relations hold for the flow of a gas through a quasi one-dimensional duct (Anderson, 1990):

$$\frac{T_0}{T}=1+\frac{\gamma-1}{2}Ma^2 \tag{3.13}$$

$$\frac{p_0}{p}=\left(1+\frac{\gamma-1}{2}Ma^2\right)^{\gamma/(\gamma-1)} \tag{3.14}$$

$$\frac{\rho_0}{\rho}=\left(1+\frac{\gamma-1}{2}Ma^2\right)^{1/(\gamma-1)} \tag{3.15}$$

where $\gamma \equiv C_p/C_v$ is the specific heat ratio. Ma represents the Mach number, which is defined as

$$Ma=\frac{V}{a} \tag{3.16}$$

where V is the velocity of the gas and a is the speed of sound in the gas, and is given by the equation

$$a=\sqrt{\gamma RT} \tag{3.17}$$

It is useful to make use of reference conditions when the flow is sonic, $Ma = 1$. These sonic, or critical, conditions are denoted by asterisks: T^*, p^*, a^* and ρ^*. They are ratios of the stagnation properties, derived from equations 3.13 to 3.15 with $Ma = 1$.

$$\frac{T^*}{T_0} = \left(\frac{2}{\gamma+1}\right) \tag{3.18}$$

$$\frac{p^*}{p_0} = \left(\frac{2}{\gamma+1}\right)^{\gamma/(\gamma-1)} \tag{3.19}$$

$$\frac{a^*}{a_0} = \left(\frac{2}{\gamma+1}\right)^{1/2} \tag{3.20}$$

$$\frac{\rho^*}{\rho_0} = \left(\frac{2}{\gamma+1}\right)^{1/(\gamma-1)} \tag{3.21}$$

For isentropic flow, all critical properties are constant; in adiabatic non-isentropic flow, a^* and T^* are constant, but p^* and ρ^* may vary. The critical velocity V^* equals the sonic sound speed a^* by definition and can be used as a reference velocity in isentropic or adiabatic flow

$$V^* = a^* = (\gamma R T^*)^{1/2} = \left(\frac{2\gamma}{\gamma-1} R T_0\right)^{1/2} \tag{3.22}$$

In order for the fluid to flow, it is necessary that the back pressure p_B be less than the stagnation pressure p_o. When a gas flows from a reservoir through a converging nozzle the gas accelerates. The velocity achieved by the gas depends on two parameters: the pressure required to increase the fluid velocity to the velocity of sound ($Ma = 1$) at the exit is denoted by p^*. Further reduction in the back pressure does not result in additional increases in the mass flow rate. Under these conditions the flow is *choked*. Under steady-flow conditions, the mass flow rate through the nozzle is constant and can be expressed as

$$\dot{m} = \rho u A = \left(\frac{p_o}{RT}\right) AMa\sqrt{\gamma RT} = p_o AMa\sqrt{\frac{\gamma}{RT}} \tag{3.23}$$

For space applications the pressure to which the thruster exhausts can be assumed to be close enough to zero. This means that shock waves will not take place in the

nozzle, since this would require that at some stage the absolute pressure of the propellant be negative – a physically impossible requirement. The minimum pressure that can be achieved in a vacuum chamber used for experiments will have some finite value, for this project approximately 20 kPa. In these cases the pressure to which the thruster exhausts to (referred to as back pressure p_B) must be taken into account in calculations.

The basic problem is (referring to Figure 3.2) as follows:
Given the information,

- stagnation conditions p_o and T_o
- exit and throat areas A_e and A_t
- back pressure p_B

calculate the following conditions at the exit plane of the nozzle:

- exit velocity V_e
- mass flow rate $\dot{m}_e$
- exit pressure p_e

Depending on the values of the variables given above, there are 7 possible flow scenarios that could occur:

a. no fluid flow (this would be for $p_o = p_B$)

b. subsonic flow throughout nozzle

c. sonic flow at throat, but subsonic flow throughout rest of nozzle

d. supersonic flow in divergent portion of nozzle with normal shockwave occurring before or at the exit plane

e. supersonic flow through divergent portion of nozzle with oblique shocks forming after nozzle exit

f. shock free supersonic flow in divergent portion of nozzle – the so called "design condition", with no oblique shocks or expansion waves occurring (fully expanded flow)

g. supersonic flow through divergent portion of nozzle with expansion waves forming after nozzle exit (under expanded flow)

For fluid to flow from the stagnation reservoir p_o to the exhaust reservoir p_B, one must have $p_o > p_B$. For a fixed A_e / A_t and fixed p_o, lowering of the back pressure will produce various flow scenarios. There are three pressures that need to be calculated in order to determine the flow condition.

- p_{sub} - value that will cause the flow to just barely go sonic at the throat, but subsonic everywhere else throughout the nozzle
- p_{norm} – the value that will result in a normal shock forming at the exit plane of the nozzle
- p_{design} – the back pressure value that will cause shock free supersonic flow in the divergent portion of the nozzle producing fully expanded flow

Procedure to Calculate p_{sub}, p_{norm} and p_{design}

Solve the area Mach number relation for the given area ratio. The area Mach number relation allows calculation of the Mach number at any location in a nozzle given the ratio of local duct to the sonic throat area. It is given by the following equation:

$$\left(\frac{A}{A^*}\right)^2 = \frac{1}{Ma^2}\left[\frac{2}{\gamma+1}\left(1+\frac{\gamma-1}{2}Ma^2\right)\right]^{(\gamma+1)/(\gamma-1)} \tag{3.24}$$

Equation 3.24 is not explicit in terms of Ma, and was solved iteratively using the method of bisection (refer appendix B.2). Since it is a quadratic equation, for a given area ratio there are two possible values for the Mach number – a subsonic and a supersonic value:

- $Ma_{sub} = Ma$ (where $Ma < 1$)
- $Ma_{design} = Ma$ (where $Ma > 1$)

The values of p_{sub} and p_{design} are obtained from the Mach number relations for pressure, i.e.

$$p_{sub} = \frac{p_o}{\left(1+\frac{\gamma-1}{2}Ma_{sub}^2\right)^{\gamma/(\gamma-1)}} \tag{3.25}$$

$$p_{design} = \frac{p_o}{\left(1+\frac{\gamma-1}{2}Ma_{design}^2\right)^{\gamma/(\gamma-1)}} \tag{3.26}$$

The value of p_{norm} is computed by assuming a normal shock of strength Ma_{design} at the exit plane. From normal shock relations:

$$p_{norm} = p_{design}\frac{1}{\gamma+1}\left(2\gamma Ma_{design}^2 - (\gamma-1)\right) \tag{3.27}$$

Hence, for a given back pressure p_B, the flow condition can be determined by comparing p_B to p_{sub}, p_{norm} and p_{design}, i.e.

$p_B > p_{sub}$ (scenario b)
subsonic flow in converging and diverging parts of nozzle, fully isentropic flow

$p_B = p_{sub}$ (scenario c)
subsonic flow in converging and diverging parts of nozzle, but with sonic flow in throat – i.e. choked flow

$p_{norm} \leq p_B < p_{sub}$ (scenario d)
subsonic flow in converging part of nozzle, sonic flow at throat, supersonic flow after throat, normal shock wave before or in exit plane, subsonic flow for the remaining length of diverging portion of nozzle

$p_{design} < p_B < p_{norm}$ (scenario f)
subsonic flow in converging part of nozzle, sonic flow at throat, supersonic flow after throat, supersonic flow in diverging portion of nozzle, oblique shock waves after exit plane

$p_B = p_{design}$ (scenario e)
subsonic flow in converging part of nozzle, sonic flow at throat, supersonic flow after throat, fully isentropic flow with no shock waves, fully expanded

$p_B < p_{design}$ (scenario g)

subsonic flow in converging part of nozzle, sonic flow in throat, supersonic flow after throat, expansion waves after exit plane, fully isentropic flow, under expanded

In the case of $p_B \leq p_{design}$, the method described in section 3.2 can be used to analyse the flow. However, if this is not the case other methods must be taken.

Case $p_B \geq p_{sub}$

In this case the flow is fully subsonic and isentropic throughout the nozzle. The analysis is similar to that for the case of $p_B \leq p_{design}$. The exit pressure p_e equals the back pressure p_B. Hence, the ratio p_o / p_e is known and can be substituted into the Mach number relation to determine the exit Mach number Ma_e,

$$Ma_e = \sqrt{\left[\left(\frac{P_o}{p_B}\right)^{\frac{\gamma-1}{\gamma}} - 1\right]\frac{2}{\gamma-1}} \tag{3.28}$$

The exit temperature T_e is determined from the temperature Mach number relation. Exit velocity is determined from $V_e = Ma_e \sqrt{\gamma R T_e}$, exit density is determined from $\rho_e = p_e / RT_e$ and mass flow rate $\dot{m}$ is calculated from $\dot{m} = \rho_e A_e V_e$.

Case $p_{norm} < p_B < p_{sub}$

This case is somewhat complicated by the presence of irreversibilities in the nozzle due to shock waves. The mass flow rate is the maximum value possible (choked) and is determined from the following equation

$$\dot{m} = \left(\frac{2}{\gamma+1}\right)^{(1/2)(\gamma+1)/(\gamma-1)} A_t \rho_o \sqrt{\gamma R T_o} \tag{3.29}$$

It is also known that the exit pressure p_e will be the same value as the back pressure p_B. The problem is as follows: given the stagnation conditions (p_o, T_o), the throat and exit areas and the exit pressure, solve for the exit conditions in order to determine the exit velocity. The mass flow rate at the exit is given by

$$\dot{m} = \rho_e A_e V_e \tag{3.30}$$

The mass flow rate is equal to the choked value given in equation 3.29. From the ideal gas equation the exit density ρ_e can be expressed as

$$\rho_e = \frac{p_e}{RT_e} \tag{3.31}$$

From the energy equation, the exit velocity V_e can be written as

$$V_e = \sqrt{2(h_o - h_e)} \tag{3.32}$$

Where the stagnation enthalpy h_o remains unchanged since the process is adiabatic, and the exit enthalpy h_e is a function calculated from the exit temperature T_e and pressure p_e. Substituting these various expressions, equation 3.30 can be rewritten,

$$\dot{m} = \frac{p_e}{RT_e} A_e \sqrt{2(h_o - h_e(p_e, T_e))} \tag{3.33}$$

The only unknown in the equation 3.33 is T_e, hence one can solve for T_e. If the gas is calorically perfect, i.e. $h = C_p(T - T_{ref})$ then the equation can be solved for T_e directly. However if $h = f(p,T)$ then it is necessary to solve for T_e by iteration. With T_e known, the velocity is easily solved by back substitution into equation 3.32

$$V_e = \sqrt{2(h_o - h(p_e, T_e))} \tag{3.34}$$

Case $p_{design} < p_B < p_{norm}$

In this case the pressure recovery occurs after the nozzle exit plane in the form of a series of complex oblique shock waves. Thus, the exit pressure p_e is lower than the back pressure p_B. In this case the conditions in the exit plane of the nozzle will be the same as for those of the case $p_B = p_{design}$ since the irreversibilities only occur after the flow has left the exit plane.

3.3 Boiling and Phase Changes

3.3.1 Liquid-Vapour Mass Transfer

When a fluid is at saturation conditions, saturated liquid and vapour co-exist at that saturation temperature and pressure. Should the pressure suddenly drop (for example due to the opening of a valve), phase change (evaporation) will occur as some of the liquid evaporates since the fluid is at a lower pressure than the saturation pressure corresponding to the temperature. The equation used to model this phase change phenomena resulting from lowering of the pressure is that given by Mills (1995) which describes the mass transfer across the liquid-vapour interface:

$$\dot{m} = A_{lv} K \left[\frac{p_s}{\sqrt{T_s}} - \frac{p_v}{\sqrt{T_v}} \right] \tag{3.35}$$

where $K = 2\sigma / \left((2-\sigma)\sqrt{2\pi R} \right)$, constant for a given fluid

p_v = pressure of the vapour adjacent to the liquid surface

$p_s = p_{sat@T\ell}$, saturation vapour pressure corresponding to liquid surface temperature

σ = condensation coefficient, value not known for butane, can be experimentally correlated

T_v = temperature of the vapour adjacent to the liquid surface

T_s = liquid surface temperature

A_{lv} = surface area of the liquid-vapour contact area

Note that a negative $\dot{m}$ in equation 3.35 implies that evaporation is occurring. This will happen if $p_v < p_s$.

3.3.2 Quasi–Equilibrium Conditions

Conventional thermodynamics makes the assumption of thermodynamic equilibrium, i.e. if a liquid and vapour are in contact with another and there is no heat or mass transfer between the two phases then they must be at the same pressure and temperature. In this case the fluid is referred to as being saturated, and it is typical to define the quality x of the mixture as follows:

$$x = \frac{m_v}{m_l + m_v} \tag{3.36}$$

where m_v and m_l are the masses of vapour and liquid in the control volume respectively. Figure 3.3 is a sketch of such a system. In this case it is assumed that there is no heat or mass transfer between the liquid and vapour, and there is no heat transfer between the system and its surroundings. Thus, the temperatures and pressures will be equal.

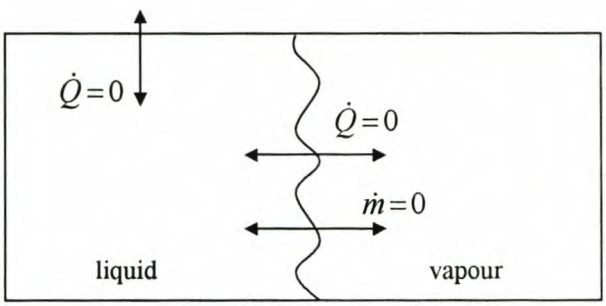

Figure 3.3 Liquid and vapour at thermodynamic equilibrium

It was found that for the purposes of modelling the phase change phenomena of the butane in the thruster system that the assumption of thermodynamic equilibrium was inappropriate. Instead a quasi-equilibrium condition was assumed. Mass transfer could take place between the liquid and vapour but the phases had to be at the same pressure. No heat transfer took place between liquid and vapour. However, both liquid and vapour could exchange heat with the surroundings, and energy transfer could occur due to the mass transfer, i.e. $\dot{m}h$. Since, the two control volumes were in contact with each other their pressures had to be equal. However, their temperatures did not have to be equal – thus the vapour could become superheated while before all the liquid had evaporated. Hence, non-thermodynamic equilibrium conditions were allowed to exist. The situation is depicted in Figure 3.4. In Figure 3.4 the liquid and vapour control volumes can be assumed to be connected by a *pressure equalising line*. For the quasi-equilibrium conditions assumed: $p_1 = p_2$ and $T_1 \neq T_2$.

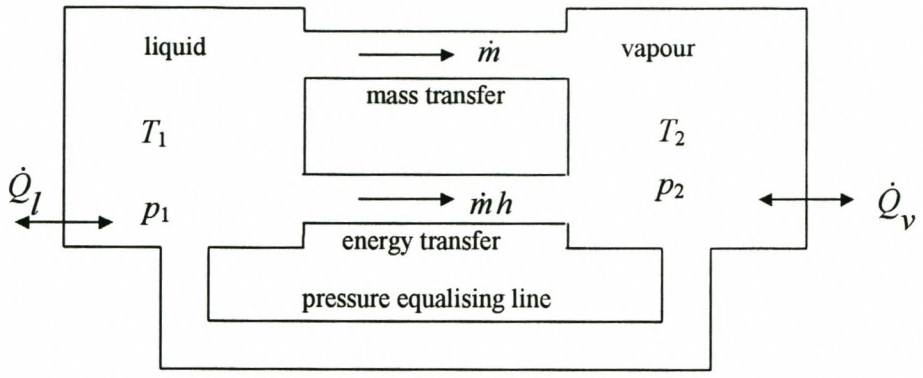

Figure 3.4 Schematic representation of the quasi-equilibrium conditions between liquid and vapour

3.4 Liquid Propellant Management

It is necessary to feed the liquid propellant to the heating chamber. Since the satellite will be operating in a micro gravity environment, it is not possible to rely on gravity. Positive expulsion systems using an active element (e.g. bladder, diaphragm, piston or bellows) can be used. However, under the circumstances it is preferable to passively manage the propellant, since bladders and diaphragm management systems require a supply of gas at high pressure. This can be achieved by making use of surface tension systems. These devices rely on surface tension forces to separate liquids from gases. Capillary pumping action arising from surface tension has been dealt with extensively in analyses of heat pipes.

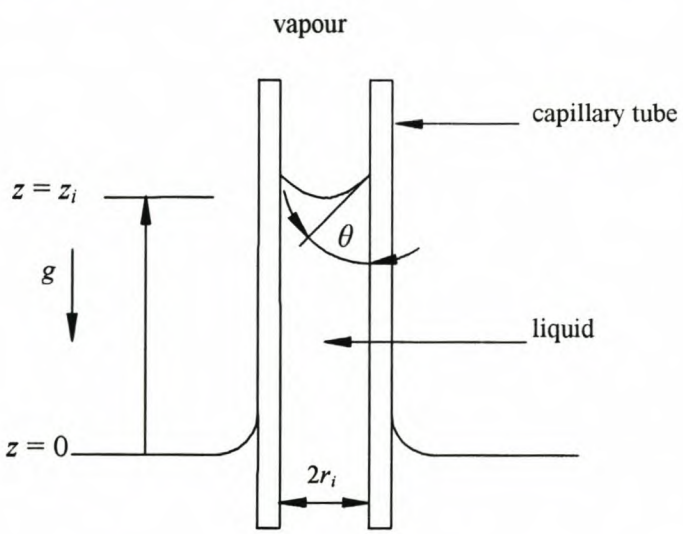

Figure 3.5 Rise of liquid in a capillary tube

Consider the capillary tube (inner radius r_i) immersed in a pool of liquid, shown in Figure 3.5. The tension force acting round the circumference is given by $2\pi r_i \sigma_l$. For equilibrium this must be balanced by the force due to the pressure acting across the surface $\Delta p \pi r_i^2$. Equating the two forces, and rearranging, an expression for the pressure difference Δp is obtained:

$$\Delta p = 2\sigma_l / r_i \tag{3.37}$$

If the surface has two radii of curvature at right angles, R_1, R_2, then (Carey, 1992)

$$\Delta p = \sigma_l \left(\frac{1}{R_1} + \frac{1}{R_2} \right) \tag{3.38}$$

Due to this pressure difference, if a vertical tube, radius r_i, is placed in an extensive pool of liquid with a free surface and the liquid is assumed to meet the wall at the contact angle $\theta < 90°$ (i.e. wets the material of the tube), the liquid will rise in the tube to a height z_i above the plane of the surface of the liquid, refer to Figure 3.5.

When $r_i << L_c$ where $L_c = \sqrt{\sigma_\ell / g(\rho_l - \rho_v)}$, the radius of curvature of the interface is approximately uniform and equal to $r_i / \cos\theta$. The condition for equilibrium is

$$(\rho_l - \rho_v) g\, z_i = 2\sigma \frac{\cos\theta}{r_i} \tag{3.39}$$

Solving for the equilibrium height of the liquid column, z_i:

$$z_i = 2\sigma \frac{\cos\theta}{(\rho_l - \rho_v) g\, r_i} \tag{3.40}$$

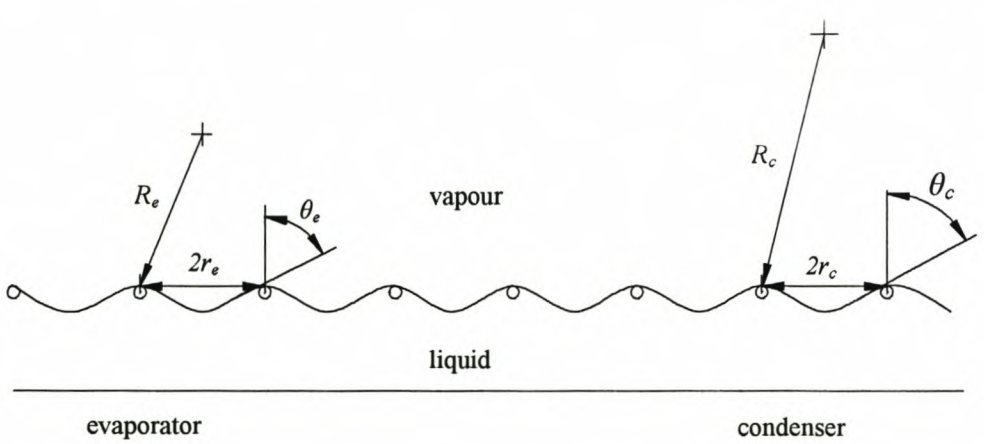

Figure 3.6 Cross section of heat pipe showing geometry

The sketch in Figure 3.6 depicts a cross-section of a heat pipe with the liquid along the wicked wall. From the geometry it is seen that $R\cos\theta = r_{eff}$. This gives the capillary head at the evaporator as

$$\Delta p = 2\sigma_l \frac{\cos\theta_e}{r_{eff,e}} \tag{3.41}$$

Similarly at the condenser

$$\Delta p_c = 2\sigma_l \frac{\cos\theta_c}{r_{eff,c}} \tag{3.42}$$

The resultant capillary head is

$$\Delta p_{cap} = 2\sigma_l \left(\frac{\cos\theta_e}{r_e} - \frac{\cos\theta}{r_c} \right) \tag{3.43}$$

Dunn and Reay (1994) set $\cos\theta = 1$ and $\cos\theta_c = 0$ to give the maximum value of Δp_{cap} as

$$\Delta p_{cap,\max} = \frac{2\sigma_l}{r_{eff,e}} \tag{3.44}$$

However, the derivation of the above equation is obtained by assuming the contact angles in the evaporator and condenser to conveniently equal to the values that will make the value of Δp_{cap} a maximum. One cannot say for certain that the contact angles in the evaporator and condenser will equal 0° and 90° respectively.

An alternative method given by Peterson (1994) utilises the concept of effective radius. Peterson suggests expressing the maximum capillary radius in terms of a single effective radius of curvature, r_{eff}. Hence, the maximum capillary pressure between the evaporator and condenser can be expressed as the difference between the capillary pressure across the meniscus at the condenser and the capillary pressure at the evaporator,

$$\Delta p_{cap,\max} = 2\sigma_l \left(\frac{1}{r_{eff,e}} - \frac{1}{r_{eff,c}} \right) \tag{3.45}$$

It can also be shown (Peterson, 1994) that the vaporisation occurring in the evaporator causes the liquid meniscus to recede into the wick, reducing the local capillary radius $r_{eff,e}$. In the condenser section, condensation causes flooding of the wick, increasing the local capillary radius $r_{eff,c}$. Due to the difference in the two radii of curvature a pressure results. Hence, pumping of the liquid from the condenser to the evaporator occurs. Under steady state conditions, it is generally assumed that the capillary radius in the condenser, $r_{eff,c}$, approaches infinity. Thus, the maximum capillary pressure under steady state conditions can be expressed as a function of the effective capillary radius of the evaporator wick only,

$$\Delta p_{cap,\max} = \frac{2\sigma_l}{r_{eff,e}} \tag{3.46}$$

This is the same result for the maximum capillary pressure obtained by Dunn and Reay (1994), except that in this case the effective radius of the wick structure is used. Values of the effective capillary radius for common wicking structures and methods to estimate effective capillary radius can be found in literature (for instance Chi, 1976 and Faghri, 1995). However, caution must be exercised when using such data, as the type of fluid used will also influence the effective capillary radius.

In order for the system to operate properly the pumping head provided by the capillary action musts be greater that the total pressure drop in the tube. This pressure drop is generally comprised of three components, namely

Δp_l = liquid pressure drop

Δp_v = vapour pressure drop

Δp_g = the gravitational pressure head

Since the system will operate in an environment where the effects of gravity are neglible, in this case the gravitational pressure head will be neglected. Thus,

$$\Delta p_{cap} \geq \Delta p_l + \Delta p_v \tag{3.47}$$

According to Dunn and Reay (1994) the flow regime in the liquid phase is almost always laminar. The liquid pressure drop is affected by the capillary geometry. For a homogenous wick (i.e. wick structures consisting of a porous structure made up of interconnecting pores, e.g. gauzes, felts and sintered wicks), a number of methods have been proposed to estimate the liquid pressure drop.

Both Faghri (1995) and Dunn and Reay (1994) propose the use of Darcy's Law for liquid flow in a porous medium. In differential pressure drop along the pipe axis is given by

$$\frac{dp_l}{dz} = -\frac{\mu_l \dot{m}_l}{\rho_l A_w K} \tag{3.48}$$

where A_w = wick cross sectional area [m^2]

K = wick permeability [m^2]

Dunn and Reay provide an equation for the total pressure drop Δp_l along the length of the tube by making use of an effective length rather than a geometric length:

$$l_{eff} = l_{ad} + 0.5\left(l_e + l_c\right) \tag{3.49}$$

where l_{ad} is the length of the adiabatic section and l_e and l_c are the evaporator and condenser lengths respectively. Assuming all values on the right hand side of equation 3.48 remains constant, direct integration along the effective length yields

$$\Delta p_\ell = \frac{\mu_\ell \, l_{eff} \, \dot{m}}{\rho_\ell \, K \, A} \tag{3.50}$$

One of the major difficulties in analysing liquid flow through a porous medium is to determine the permeability of the medium. Permeability is defined as the property of a porous material that describes the ability of the material to transmit the liquid under some applied pressure gradient. In general a specific model is needed to calculate the permeability for a specific type of wick structure, and often correlations must be made from experimental data. Faghri (1995) and Chi (1976) provide tables containing expressions that estimate wick permeability for different wick structures.

In addition Dunn and Reay (1994) mention the use of the Hagen-Poiseuille equation to describe the pressure drop occurring in the liquid due to flow through porous medium. The Hagen-Poiseuille equation for flow through porous media is (Dunn and Reay, 1994):

$$\Delta p_l = \frac{b \, \mu_l \, \dot{m} \, l_{eff}}{\pi \left(r_w^2 - r_v^2\right) \varepsilon \, r_c^2 \, \rho_l} \tag{3.51}$$

where r_w = wick radius

r_v = radius of the vapour space

r_c = radius in the condensing section

ε = fractional void of the wick

b = dimensionless constant between 10 and 20 used as a correction factor

However, equation 3.51 contains three constants b, ε and r_c which are difficult to measure in practice, and it is that method using Darcy's Law (equation 3.48) be used instead (Dunn and Reay, 1994).

In this section a qualitative overview has been given of the basic theory required to manage the liquid propellant making use of surface tension. Although this was not investigated quantitatively in this project, it would require consideration in the design of a liquefied-gas thruster system. Management of the liquid propellant is not only required to transport liquid to heating chamber, but also requires consideration due to the possible effects of liquid motion on the stability of the spacecraft. The effects of liquid motion on the satellite, termed *sloshing*, is the focus of section 3.6.

3.5 Micro-Satellite Thruster Procurement Philosophy

The following draft specification for a thruster for a micro-satellite was given by a potential client (Sunspace) to provide guidelines for the development of a thruster system.

Draft Specification for a Thruster System for a Micro-Satellite

System Design:

1. Spacecraft stabilisation method (spin/3-axis, gravity gradient)
2. Number and location of thrusters, propellant tanks, fill/drain valves, plus major components
3. Redundancy requirements
4. Contamination restrictions (refer also leakage) – plume geometry
5. System schematic

Performance:

1. Total impulse required (motivated from a "delta-V" budget for the spacecraft mission)
2. System life-cycle for "delta-V" budget
3. Thrust levels required – defined by a typical force profile (rise time/ steady/ tail-off
4. Repeatability of thrust levels
5. Maximum continuous thrust period, needed to determine heating requirements for some systems to ensure the propellant is vaporised
6. Shortest possible thrust pulse – trade off with valve opening times / operating pressure
7. Maximum acceptable leakage rate from valves, pipes and tank (refer e.g. contamination)
8. Constraints on thrust alignment (mechanical and gas-dynamic misalignment)
9. Propellant slosh or disturbance requirement in micro-gravity environment
10. Preheating requirement (if applicable)
11. Safety

Interfaces:

1. Mass limit
2. Envelope
3. Voltages
4. Power
5. Telemetry
6. Commands
7. Valve drive electronics
8. Electromagnetic interference (EMI)
9. Thermal (heat flux / temperature)

Environmental:

1. Vibration
2. Shock
3. Thermal
4. Radiation

Testing:

1. System acceptance tests – proof pressure, leakage, electrical, vibration and thermal tests
2. Component acceptance tests – proof pressure, leakage, performance, electrical tests, vibration, thermal

Product Assurance

1. Standards of documentation
2. Design reviews
3. Delivery review

Statement of Work

1. Programme schedule
2. Hardware deliverables
3. Documentation delivables

3.6 Sloshing

If it is intended to store propellant in liquid form there will be a significant amount of mass on board the satellite that will not be rigidly attached to the satellite structure leading to the phenomena known as *sloshing*. Sloshing refers to the free surface oscillations of a liquid in a partially filled tank. This liquid motion in the propellant tanks can have a significant influence on attitude dynamics, since sloshing of propellants may adversely affect the stability of a space vehicle and the integrity of the tank structure.

The objective of this section is to provide some basic background information necessary to perform a preliminary analysis of the influence of sloshing. In particular, it is shown how sloshing can play a role in determining the position of the propellant tanks within the satellite structure.

3.6.1 Gravitational Effects Relative to Surface Tension

The Bond number Bo is an indication of the size of the body forces (i.e. gravitational and acceleration fields) relative to the surface tension of the liquid. The Bond number is given by:

$$Bo=\frac{\rho g R_o^2}{\sigma} \tag{3.52}$$

Where ρ is the density of the liquid, σ is the surface tension, g is the gravitational or steady axial acceleration and R_o is the radius of the propellant tank.

According to Dodge and Garza (1967) very low-gravity fluid mechanics are characterised by $Bo < 1$, and high-gravity problems occurs for $Bo > 1000$. In general Bond numbers much larger than unity indicate that gravity forces dominate, while Bond numbers much less than unity indicate that surface tension forces dominate. It is recommended (Braslow, 1968) that surface tension effects only be ignored for Bond numbers less than 100.

Assuming liquid butane at a pressure of 200 kPa and temperature of 20 °C the density and surface tension are (ASHRAE Handbook, 2001) $\rho=578.4$ kg/m^3 and $\sigma=0.01241$

N/m. The radius of the propellant tank is taken to be 0.05 m. The Bond number for this situation is calculated on earth (g = 9.81 m/s^2) and in space (g = 10^{-5} m/s^2, value given by Dodge and Garza (1967))

$$Bo_{earth} = \frac{(578.4)(9.81)(0.05)^2}{0.01214} = 1168$$

$$Bo_{space} = \frac{(578.4)(10^{-5})(0.05)^2}{0.01214} = 0.0012$$

It can be seen that on earth, as expected, gravitational effects are dominant, whilst in space surface tension effects are dominant. Also, for a typical manoeuvre (a 50 mN thrust on a 150 kg satellite) producing an acceleration of 33.33×10^{-5}, the Bond number due the acceleration caused by the thrust, Bo_{thrust} would be

$$Bo_{thrust} = \frac{(578.4)(33.33\times10^{-5})(0.05)^2}{0.01214} = 0.040$$

indicating that surface effects would be dominant.

3.6.2 Sloshing Frequency

For lateral sloshing in a rigid cylindrical tank with a flat bottom, the frequency of free-surface motion in a gravity-dominated environment is given (Braslow, 1968) as

$$f_n = \sqrt{\varepsilon_n g R_o^{-1} \tanh\left(\varepsilon_n h R_o^{-1}\right)} \tag{3.53}$$

where

ε_n = the root of $\frac{d}{dx} J_1(x)\Big|_{x=\varepsilon_n} = 0$,

J_1 = a Bessel function of first kind and order

h = the height of the fluid surface

The value of the ε_n for the first slosh mode, i.e. ε_1, is 1.841. Using the data used for the calculation of the Bond numbers, a plot of the first sloshing mode as a function of the ratio of fluid height to tank radius is given in Figure 3.7. It can be seen that once the fluid height is greater than about 10 times the tank radius the sloshing frequency does not increase with further increases in fluid height and reaches a maximum value of approximately 2.2 Hz. It is desired to keep sloshing frequencies as high as possible as propellant forces due to sloshing are larger at lower frequencies as the sloshing masses are higher (Braslow, 1967). Thus, ideally the propellant tank should be cylindrical with a relatively small radius. Such a tank would have the advantage that

if the ratio of thickness to radius is sufficiently high, the tank could be considered a tube and not a pressure vessel. Pressure vessels for satellite applications would thus require significantly more analysis and testing to be done on the system as opposed to tube systems to comply with the development specifications and typical launch agency requirements.

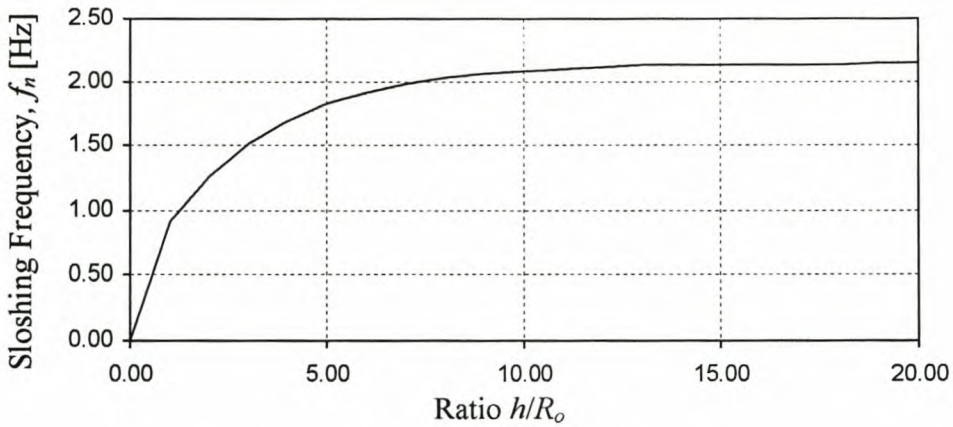

Figure 3.7 Frequencies of first sloshing mode

3.6.3 Low Gravity Sloshing

For low gravity sloshing the Bond numbers are low ($Bo << 1$). In these circumstances the surface tension forces in the liquid are more significant than the body forces due to gravity. According to Dodge and Garza (1967) the low-gravity sloshing mass is much less than for the high-gravity sloshing mass, since more of the liquid is in contact with the tank walls and thus cannot take part in free surface sloshing oscillations. Hence, the sloshing loads are small compared to the structural capability of the tank. However, sloshing under these circumstances is important as it can influence control stability and attitude dynamics. The influence is mainly due to two effects: energy dissipation due to liquid slosh and changes in the inertia properties of spacecraft.

3.6.3.1 Energy Dissipation Due to Liquid Slosh

This section discusses energy dissipation due to liquid sloshing inside the propellant tanks. Energy dissipation due to liquid slosh is an important aspect with regards to

the spin-stabilisation of a satellite. A qualitive overview of the method to analyse energy dissipation is presented (Agrawal, 1986).

Figure 3.8 depicts the motion of a symmetric satellite, with $I_{yy} = I_s$ and $I_{xx} = I_{zz} = I_T$. The spacecraft motion consists of the spacecraft rotation ω_s about its spin axis I_s and the spin axis rotating about the angular momentum vector **H** with angular velocity ω_n. The motion of the spin axis rotating about the momentum vector is called nutational motion and angle θ that the spin axis makes with the momentum vector is called the nutation angle.

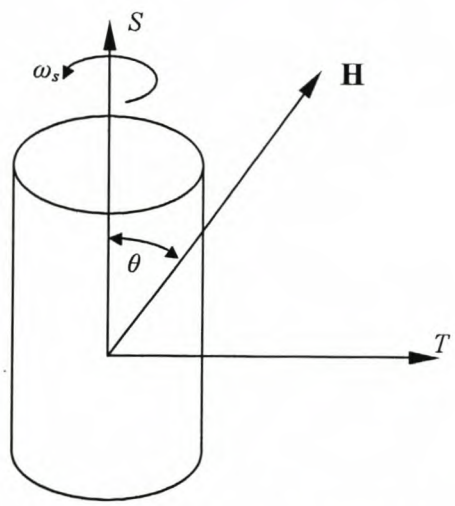

Figure 3.8 Motion of an axi-symmetric satellite

If the entire satellite were an entirely rigid structure then the nutation angle θ would be constant. However since the satellite has liquid on board, it is a non-rigid body due to the fact that the liquid can experience relative motion to the other components of the satellite structure. The oscillations experienced by the liquid will result in energy dissipation. In the case of energy dissipation, the nutation angle is not constant.

The nutation angle is assumed to have exponential growth or decay, i.e.

$$\theta = \theta_0 \, e^{t/\tau} \tag{3.54}$$

where τ is a time constant. The energy dissipation rate $\dot{E}$ is assumed to be a function of the spacecraft parameters in the following manner:

$$\frac{\dot{E}}{\theta^2} = n f(\omega, \lambda, m, \rho, \mu, R, d, z, s, g) \tag{3.55}$$

where n = number of tanks

ω = spin rate

λ = body nutational frequency

m = mass of fluid

ρ = density of fluid

μ = viscosity of fluid

R = radial distance of tank from spin axis

z = axial offset of tank centre from vehicle centre of mass

s = shape factor of tank

g = gravitational acceleration

d = diameter of tank

Analytical predictions for energy dissipation are very difficult to compute and are generally inaccurate. The recommended approach is to perform ground slosh tests and extrapolate the in-orbit energy dissipation from the ground tests using scaling techniques from dimensional analysis. Applying dimensional analysis to equation 3.55 the energy dissipation rate is expressed as a function of a group of dimensionless variables:

$$\frac{\dot{E}}{n\rho d^5 \omega^3 \theta^2} = f\left(Re, Fr, Ff, s, \sigma, d/R, z/R\right) \tag{3.56}$$

where $Re = \rho\omega d^2/\mu$ = angular velocity Reynolds number

$Fr = \omega^2 R/g$ = Froude number

Ff = fraction fill of the tank

σ = inertia ratio, I_s/I_t

The time constant group τ_{CG} is given by:

$$\tau_{CG} = \tau\frac{n d^5 \omega \rho}{I_T} = f\left(Re, Fr, Ff, s, \sigma, d/R, z/R\right) \tag{3.57}$$

This time constant group will be the same for both ground test and in-orbit conditions. This allows the in-orbit time constant to be extrapolated from the time constant determined from ground tests by the following relationship:

$$\tau_o = \frac{\tau_G \left(I_{To} / I_{Tg}\right)}{\left(n_o / n_g\right)\left(\rho_o / \rho_g\right)\left(d_o / d_g\right)^5 \left(\omega_o / \omega_g\right)} \tag{3.58}$$

It is useful to note from equation 3.58 that the geometrical properties of the satellite used in ground tests do not have be the same as those of the satellite in orbit, i.e. a scale model can be built for ground testing purposes.

3.6.3.2 Change in inertia properties of spacecraft

Liquid motion inside a spacecraft will lead to changes in the inertia properties of the spacecraft. Changes in inertia can cause stability problems. It is necessary to investigate how the placement of propellant tanks can affect the spacecraft stability. From rigid body dynamics, it is known that the nominal spin axis of a single-spinning body is aligned along the axis of maximum or minimum moment of inertia. In the absence of nutation, the spin axis will be coincident with the angular momentum and total angular velocity vectors. Hence, every point on the rotating body will experience pure rotation about the spin axis. The body is said to be dynamically stable if a small dynamic imbalance introduced into the body causes a bounded tilt on the spin axis (Agrawal, 1986). Consider the spacecraft depicted in Figure 3.9. The inertia matrix **I** of the spacecraft is (Baruh, 1999)

$$\mathbf{I} = \begin{bmatrix} I_{xx} & -I_{xy} & -I_{xz} \\ -I_{xy} & I_{yy} & -I_{yz} \\ -I_{xz} & -I_{yz} & I_{zz} \end{bmatrix} \tag{3.59}$$

Where I_{xx}, I_{yy} and I_{zz} are the moments of inertia about the x, y and z axis, and I_{xy}, I_{xz} and I_{yz} are the products of inertia.

In the absence of dynamic imbalance, the products of inertia are zero, and x, y and z will be the principle moments of inertia. However, if the products of inertia are non-zero, then the spin axis will be tilted with an angle θ from the y-axis. θ has components θ_x and θ_z along the x and z axes. The new coordinate system is given by $x'y'z'$, with the new spin axis being y'. Since y' is the spin axis, the products of inertia $I_{x'y'}$ and $I_{y'z'}$ are zero. $I_{x'y'}$ and $I_{y'z'}$ can be expressed in terms of the moments and products of inertia for the xyz axes system (Baruh, 1999):

$$I_{x'y'} = I_{xy}\cos 2\theta_z + \frac{I_{xx} - I_{yy}}{2}\sin 2\theta_z \tag{3.60}$$

$$I_{y'z'} = I_{yz}\cos 2\theta_x + \frac{I_{yy} - I_{zz}}{2}\sin 2\theta_x \tag{3.61}$$

Putting $I_{x'y'}$ and $I_{y'z'}$ equal to zero and solving for θ_x and θ_z:

$$\tan 2\theta_z = \frac{2I_{xy}}{I_{yy} - I_{xx}} \tag{3.62}$$

$$\tan 2\theta_x = -\frac{2I_{yz}}{I_{yy} - I_{zz}} \tag{3.63}$$

For small angles of θ_x and θ_z (which is the case here), the approximation of $\tan\theta \approx \theta$ can be made, thus:

$$\theta_z = \frac{I_{yz}}{I_{yy} - I_{zz}} \tag{3.64}$$

$$\theta_x = -\frac{I_{xy}}{I_{yy} - I_{xx}} \tag{3.65}$$

Consider the satellite spinning about the y-axis in orbit depicted in Figure 3.9. For the sake of simplicity it is assumed that the only non-zero product of inertia is I_{xy}, which may be represented by a *dumbbell*. In the absence of propellant motion, the spin axis will be tilted an angle θ_z as given in equation 3.64. If allowance is made for the propellant to deform, two types of motion will occur. Firstly, the liquid free surface will tilt in each tank parallel to the spin axis. Secondly, the propellant between interconnected tanks will migrate such that all points on the surface in both tanks will be equidistant from the spin axis. The propellant deformation will cause an added imbalance and affect the product of inertia. However, this imbalance will be proportional to the tilt angle $\bar{\theta}_z$. The final tilt angle with propellant motion, $\bar{\theta}_z$ is given by:

$$\bar{\theta}_z = \frac{I_{xx} + K_P\bar{\theta}_z}{I_{yy} - I_{xx}} \tag{3.66}$$

Where K_P is a positive proportionality constant to account for the added imbalance affecting the product of inertia I_{xy}. Solving for $\bar{\theta}_z$ in equation 3.66:

$$\bar{\theta}_z = \frac{I_{xy}}{I_{yy} - I_{zz}} \frac{1}{1 - K_P / (I_{yy} - I_{zz})} \tag{3.67}$$

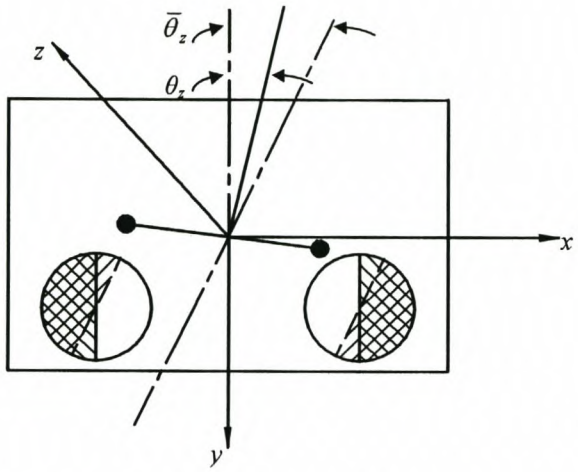

Figure 3.9 Dynamic imbalance due to liquid motion

Define the inertia ratio σ and amplification factor α as follows:

$$\sigma \equiv \frac{I_{yy}}{I_{xx}} \tag{3.68}$$

$$\alpha \equiv \frac{1}{1 - K_P / (I_{xx}(\sigma - 1))} \tag{3.69}$$

Recalling equation 3.66, the expression for θ_z in equation 3.64, and using the definitions of σ and α in equations 3.68 and 3.69, the tilt angle $\bar{\theta}_z$ is expressed as:

$$\bar{\theta}_z = \alpha \theta_z \tag{3.70}$$

Equations 3.68 and 3.70 show that the propellant motion will amplify the rigid body tilt if $\sigma > 1$. Static instability corresponds to an infinite amplification (i.e. $\alpha \rightarrow \infty$), which will occur if

$$\sigma = 1 + K_P / I_{xx} \tag{3.71}$$

Hence, the requirement for static stability is

$$\sigma > 1 + K_P / I_{xx} \tag{3.72}$$

For $\alpha < 1$, the propellant motion attenuates rigid body tilt. In this case static instability is not possible. In order to have $\alpha < 1$, one must have $\sigma < 1$. Hence, in order to make static instability not possible:

$$\frac{I_{yy}}{I_{xx}} < 1 \tag{3.73}$$

Methods of how to ensure that the condition laid down in equation 3.73 is met must be investigated. This can be achieved by design of the tank geometry and proper placement of the tank. The advantages of a cylindrical tank with small radius to height ratio are mentioned in section 3.6.2. From a stability point of view, such a tank also offers advantages, provided that it is properly placed. The moment of inertia about the centreline axis of such a tank is very small, and is generally negligible in comparison to the moments of inertia about the axis perpendicular to the centreline axis. Consider the two possible placements of a cylindrical fuel tank, depicted in Figure 3.10 and Figure 3.11.

Figure 3.10 depicts a well-placed fuel tank since I_{yy} of the tank is very small compared to I_{xx} of the tank. Hence, if the values of I_{xx} and I_{yy} without the fuel tank were similar, the placement of the fuel tank will increase the dynamic stability of the satellite in orbit, since the I_{xx} of the satellite will increased significantly more than I_{yy}, satisfying the requirement given in equation 3.73.

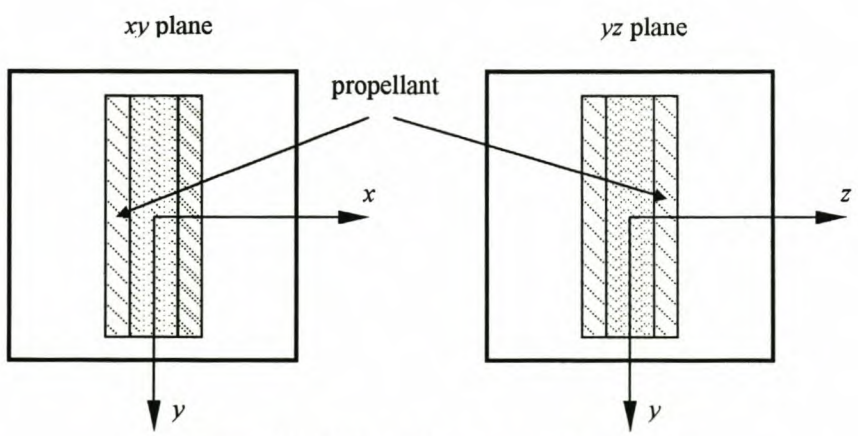

Figure 3.10 Well placed propellant tanks

Figure 3.11 is an example of a poorly placed tank. The tank's axis is aligned to the x-axis and is at right angles to the y-axis, with the result that I_{yy} is much larger than I_{xx}. Additionally, due to the spin about the y-axis the fluid moves to the ends of the tank to form a dumbbell, creating an even larger I_{yy} since the mass is at the furthest possible distance from the y-axis. The positioning of the propellant tank just on the inside of the satellite structure (the yz-plane in Figure 3.11) also has the effect of increasing the value of I_{yy}, since the mass is further from the y-axis.

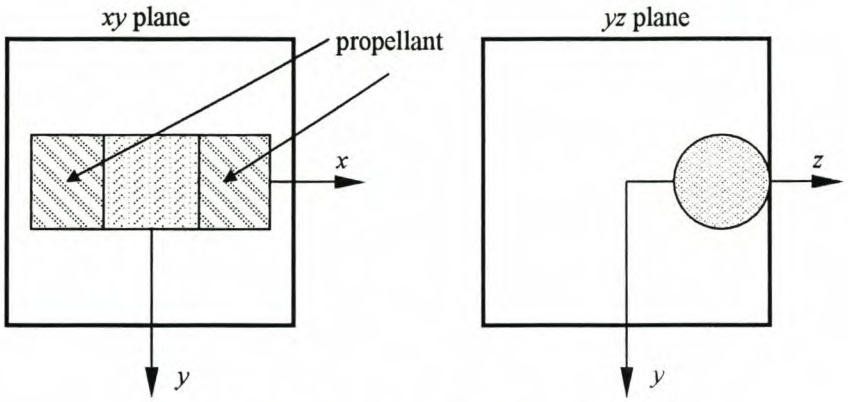

Figure 3.11 Poorly placed propellant tanks

An overview of sloshing has been given, since sloshing plays an important role in spacecraft where liquid is stored onboard. The effect of gravitational environment on the significance of sloshing was discussed and the Bond number was defined as a parameter indicating whether the sloshing problem being dealt with can be classed as a low or high gravity fluid mechanics problem. An equation to calculate lateral sloshing frequency in a cylindrical tank was presented as well as a graph indicating the effect of cylinder geometry on sloshing frequency. Energy dissipation occurring due to sloshing was discussed and a qualitative overview was given as to how one would go about extrapolating the in-orbit energy dissipation rate using data obtained from tests on earth. Finally, it was shown how the movement of liquid in the tanks can affect the inertial properties and hence the dynamics of a satellite in orbit. Based on this, simple guidelines relating to the placement of propellant tanks were given.

4 THERMO-FLUID MODELLING OF THE SYSTEM

The numerical modelling of a thruster system in order to predict the thrust delivered based on the conditions of the propellant is important. It is important because it allows the effect of changes in various system parameters (e.g. propellant pressure and temperature, nozzle geometry, heat input) to be predicted before doing laboratory testing. Therefore, computer programs have been developed to serve as an analytical tool in the design of a thruster system.

The system was approximated as being one-dimensional and the control-volume approach was taken. In addition the time-dependence of the system was taken into account, i.e. the transient behaviour was modelled. Three simulation programs were written in *Visual Basic 6.0*, one modelling a system using air as propellant (*AirSim.exe*) and the other two (*ButaneSim_A.exe* and *ButaneSim_B.exe*) using butane as propellant. The only difference between *ButaneSimA.exe* and *ButaneSim_B.exe* is in the method used in analysing the flow through the nozzle. *ButaneSim_B.exe* made use of the idealised gas dynamic theory presented in section 3.2, whereas *ButaneSim_A.exe* made use of the three governing equations (continuity, energy and momentum) directly as will be shown in section 4.2.

4.1 Numerical Simulation of a One-Dimensional Transient System

The simulations conducted modelled the system as one-dimensional (some cases, for example the nozzle, required the modelling of a quasi one-dimensional system – refer to section 4.2). Consider the simple one-dimensional system depicted in Figure 4.1, consisting of a control volume i between two control volumes i -1 and i + 1:

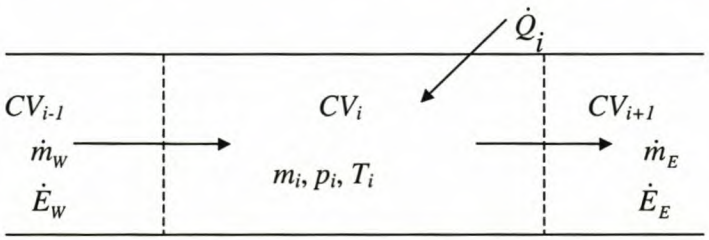

Figure 4.1 One-dimensional control volume

The principles of continuity and conservation of energy are applied to the system giving:

$$\frac{dm_i}{dt} = \dot{m}_W - \dot{m}_E \tag{4.1}$$

$$\frac{dE_i}{dt} = \dot{E}_W - \dot{E}_E + \dot{Q}_i \tag{4.2}$$

The derivatives are replaced by first order finite difference approximations using a finite time step Δt:

$$\frac{m_i^{new} - m_i^{old}}{\Delta t} = \dot{m}_W - \dot{m}_E \tag{4.3}$$

$$\frac{E_i^{new} - E_i^{old}}{\Delta t} = \dot{E}_W - \dot{E}_E + \dot{Q}_i \tag{4.4}$$

The above equations can be rearranged to give explicit equations for the new values of mass and energy

$$m_i^{new} = m_i + (\dot{m}_W - \dot{m}_E)\Delta t \tag{4.5}$$

$$E_i^{new} = E_i + (\dot{E}_W - \dot{E}_E + \dot{Q}_i)\Delta t \tag{4.6}$$

Hence, the new mass and energy of the control volumes are *explicitly* determined from the old values alone. The algorithm for this mathematical model can be found in appendix E.1.

4.2 Numerical Method to Solve for Steady State Quasi One-Dimensional Nozzle Flow

Traditional gas dynamic theory often makes a number of convenient assumptions in order to provide straight-forward analytical solutions to solve for the flow of a compressible fluid in a nozzle. These assumptions were discussed in section 3.2.

However, if the gas is generated by the evaporation (or boiling) of liquid propellant, it might not be substantially superheated and thus the ideal gas equation might not hold. Fortunately for the range of pressures and temperatures that the butane was subjected

to, it was found that the ideal gas equation was reasonably accurate, refer to appendix A.1 for more details. However, the assumption of a calorically perfect gas, $h=C_p\left(T-T_{ref}\right)$, where C_p is constant, was not valid. Additionally, it is likely that the exit state could be in the two-phase region with the possibility of condensation of liquid droplets. However, for sufficiently high flow velocities there will not be sufficient time for the formation of liquid droplets and the associated heat transfer process (Potter et al., 2002).

The objective is to devise a scheme in order to solve for the flow through a nozzle without having to rely on the idealised gas dynamic theory presented in section 3.2. Thus, it is necessary to start from the fundamental governing equations used to describe the system, i.e. conservation of mass, momentum and energy. Consider the control volume depicted in Figure 4.2, where u denotes velocity in the axial (x) direction and τ_w is the frictional shear stress acting on the fluid.

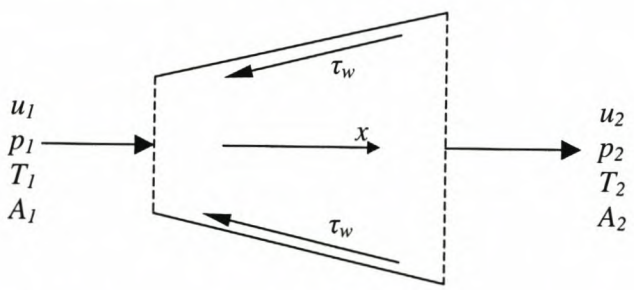

Figure 4.2 Finite control volume for quasi one-dimensional flow

4.2.1 Governing Equations

The governing equations describing the system are (Anderson 1990):
continuity

$$\rho_1 u_1 A_1 = \rho_2 u_2 A_2 \tag{4.7}$$

momentum

$$p_1 A_1 + \rho_1 u_1^2 A_1 + \int_{A_1}^{A_2} p\, dA = p_2 A_2 + \rho_2 u_2^2 A_2 + \int_{x_1}^{x_2} \pi D \tau_w\, dx \tag{4.8}$$

energy

$$h_1 + \frac{u_1^2}{2} = h_2 + \frac{u_2^2}{2} \tag{4.9}$$

If the inlet conditions at the throat of the nozzle are known, then the nozzle can be subdivided into n control volumes moving downstream from node 0 to node n.

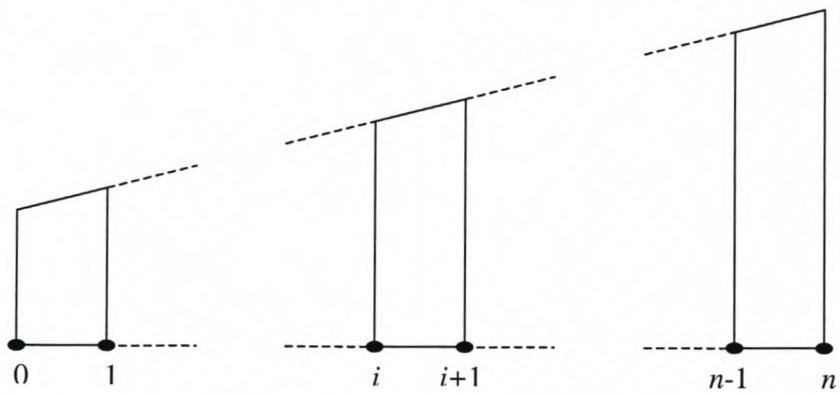

Figure 4.3 Subdivision of nozzle into finite control volumes

The first integral term in the momentum equation equation 4.8 represents the pressure force on the sides of the control surfaces between locations 1 and 2. The second integral term in the momentum equation is to account for viscous friction between the fluid and the nozzle walls. By assuming a linear variation in pressure over the control volume (a reasonable assumption if the control volume is sufficiently small), the integral terms in the momentum equation can be evaluated.

Evaluation of $\int_{A_{in}}^{A_{out}} p\, dA$

The differential area dA can be expressed as

$$dA = 2\pi r\, dr \tag{4.10}$$

Approximating the pressure variation as linear, yields the following expression for pressure as a function of radius

$$p(r) = p_{in} + \frac{p_{out} - p_{in}}{r_{in} - r_{out}}(r - r_{in}) \tag{4.11}$$

Substituting for p and dA

$$\int_{A_{in}}^{A_{out}} p\,dA = \int_{r_{in}}^{r_{out}} \left(p_{in} + \frac{p_{out} - p_{in}}{r_{out} - r_{out}} (r - r_{out}) \right) 2\pi r\,dr \tag{4.12}$$

Carrying out the integration and substituting the upper and lower integration limits:

$$2\pi \left[\frac{1}{2} p_{in} \left(r_{out}^2 - r_{in}^2 \right) + \frac{p_{out} - p_{in}}{r_{out} - r_{in}} \left(\frac{1}{3} \left(r_{out}^3 - r_{in}^3 \right) - \frac{1}{2} \left(r_{in}\, r_{out}^2 - r_{in}^3 \right) \right) \right] \tag{4.13}$$

Evaluation of $\int_{x_1}^{x_2} \pi D \tau_w\,dx$

The frictional shear stress τ_w can be expressed in terms of the Darcy friction factor f:

$$\tau_w = \frac{1}{8} \rho u^2 f \tag{4.14}$$

The properties D, ρ and u all vary with the distance x along the nozzle. However, since the distance between control volumes is very small, the properties can be approximated as being piecewise linear, i.e.:

$$D(x) = 2r(x) = 2 \left(r_{in} + \frac{r_{out} - r_{in}}{x_{out} - x_{in}} (x - x_{in}) \right) \tag{4.15}$$

$$\rho(x) = \rho_{in} + \frac{\rho_{out} - \rho_{in}}{x_{out} - x_{out}} (x - x_{in}) \tag{4.16}$$

$$u(x) = u_{in} + \frac{u_{out} - u_{in}}{x_{out} - x_{in}} (x - x_{in}) \tag{4.17}$$

Making use of the ideal gas relation $\rho = p/RT$, the equation for density variation (equation 4.16) is written as

$$\rho(x) = \frac{p_{in}}{RT_{in}} + \frac{p_{out}/RT_{out} - p_{in}/RT_{in}}{x_{out} - x_{in}} (x - x_{in}) \tag{4.18}$$

For convenience, the following gradients are defined:

$$m_r = \frac{r_{out} - r_{in}}{x_{out} - x_{in}} \tag{4.19}$$

$$m_\rho = \frac{p_{out}/RT_{out} - p_{in}/RT_{in}}{x_{out} - x_{in}} \tag{4.20}$$

$$m_u = \frac{u_{out} - u_{in}}{x_{out} - x_{in}} \tag{4.21}$$

Hence, it is necessary to evaluate the following integral:

$$\int_{x_{in}}^{x_{out}} \frac{1}{4}\pi f\left(r_{in} + m_r\left(x - x_{in}\right)\right)\left(\frac{p_{in}}{RT_{in}} + m_\rho\left(x - x_{in}\right)\right)\left(u_{in} + m_u\left(x - x_{in}\right)\right)^2 dx \tag{4.22}$$

The expression above (equation 4.22) will be referred to as the frictional term, f_{fric_term}. Carrying out the integration and substituting the upper and lower integration limits, the expression for f_{fric_term} becomes:

$$f_{fric\_term} =$$

$$\frac{1}{4}\pi f\left[C_o\left(\Delta x\right) + \frac{1}{2}C_1\left(\Delta x\right)^2 + \frac{1}{3}C_2\left(\Delta x\right)^3 + \frac{1}{4}C_3\left(\Delta x\right)^4 + \frac{1}{5}C_4\left(\Delta x\right)^5\right] \tag{4.23}$$

Where

$$\Delta x = x_{out} - x_{in} \tag{4.24}$$

$$C_0 = r_{in}\,\rho_{in}\,u_{in}^2 \tag{4.25}$$

$$C_1 = r_{in}\,m_\rho\,u_{in}^2 + \rho_{in}\,m_r\,u_{in}^2 + 2\,r_{in}\,\rho_{in}\,m_u \tag{4.26}$$

$$C_2 = m_r\,m_\rho\,u_{in}^2 + 2\,r_{in}\,m_\rho\,m_u + 2\,m_u\,m_r\,\rho_{in} + r_{in}\,\rho_{in}\,m_u^2 \tag{4.27}$$

$$C_3 = 2\,m_r\,m_\rho\,m_u + r_{in}\,m_\rho\,m_u^2 + \rho_{in}\,m_r\,m_u^2 \tag{4.28}$$

$$C_4 = m_r\,m_\rho\,m_u^2 \tag{4.29}$$

4.2.2 Mathematical Solution Method

The basic problem statement is as follows: given all inlet conditions into a control volume (i.e. A_{in}, u_{in}, T_{in}, p_{in}) as well as the area at the exit of the control volume, determine the exit conditions of the fluid (i.e. u_{out}, T_{out}, p_{out}). Hence, the three governing equations (continuity, momentum and energy) must be solved simultaneously for each control volume. They compromise a system of non-linear equations that can be solved by iteration.

The method used to solve the set of 3 simultaneous non-linear equations is Newton's method applied to systems of non-linear equations (Gerald and Wheatley, 1999). The method is as follows:

Given 3 equations ($f_1(x,y,z), f_2(x,y,x), f_3(x,y,z)$), rewrite them in the form

$$f_1(x,y,z)=0$$
$$f_2(x,y,x)=0$$
$$f_3(x,y,z)=0$$

In this case f_1, f_2 and f_3 represent the continuity, momentum and energy equations respectively and x, y and z represent p_{out}, T_{out} and u_{out}. Thus,

f_1: continuity equation

$$\frac{p_{in}}{RT_{out}}u_{in}A_{in}-\frac{p_{out}}{RT_{out}}u_{out}A_{out}=0 \tag{4.30}$$

f_2: momentum equation

$$\begin{aligned}&p_{in}A_{in}+\frac{p_1}{RT_1}u_{in}^2A_{in}+\\&2\pi\left[\frac{1}{2}p_{in}\left(r_{out}^2-r_{in}^2\right)+\frac{p_{out}-p_{in}}{r_{out}-r_{in}}\left(\frac{1}{3}\left(r_{out}^3-r_{in}^3\right)-\frac{1}{2}\left(r_{in}r_{out}^2-r_{in}^3\right)\right)\right]\\&-p_2A_2-\frac{p_2}{RT_2}u_{out}^2A_{out}-\int_0^L\frac{1}{8}\pi D\rho u^2 f\,dx=0\end{aligned} \tag{4.31}$$

f_3: energy equation

$$h_{in}+\frac{u_{in}^2}{2}-h_{out}^2-\frac{u_{out}^2}{2}=0 \tag{4.32}$$

It is necessary to find the partial derivatives of all the functions with respect to each of the variables. Fortunately, analytical expressions could be obtained for most of the partial derivatives. Where this was not possible, the partial derivatives were obtained numerically by recalculating the functions with small perturbations δ to each of the variables. The partial derivatives of the functions were

$$(f_1)_{p_{out}} = \frac{\partial f_1}{\partial p_{out}} = -\frac{u_{out} A_{out}}{R T_{out}} \tag{4.33}$$

$$(f_1)_{T_{out}} = \frac{\partial f_1}{\partial T_{out}} = \frac{p_{out} u_{out} A_{out}}{R T_{out}^2} \tag{4.34}$$

$$(f_1)_{u_{out}} = \frac{\partial f_1}{\partial u_{out}} = -\frac{p_{out} A_{out}}{R T_{out}} \tag{4.35}$$

$$\begin{aligned}(f_2)_{p_{out}} = \frac{\partial f_2}{\partial p_{out}} &= \frac{2\pi}{r_{out} - r_{in}}\left(\frac{1}{3}\left(r_{out}^3 - r_{in}^3\right) - \frac{1}{2}\left(r_{in}\, r_{out}^2 - r_{in}^3\right)\right) \\ &\quad - A_{out} - \frac{A_{out} u_{out}^2}{R T_{out}} - \\ &\quad \frac{f_{fric\_term}(p_{out} + \delta, T_{out}, u_{out}) - f_{fric\_term}(p_{out}, T_{out}, u_{out})}{\delta}\end{aligned} \tag{4.36}$$

$$\begin{aligned}(f_2)_{T_{out}} = \frac{\partial f_2}{\partial T_{out}} &= \frac{p_{out} A_{out} u_{out}^2}{R T_{out}^2} \\ &\quad - \frac{f_{fric\_term}(p_{out}, T_{out} + \delta, u_{out}) - f_{fric\_term}(p_{out}, T_{out}, u_{out})}{\delta}\end{aligned} \tag{4.37}$$

$$\begin{aligned}(f_2)_{u_{out}} = \frac{\partial f_2}{\partial u_{out}} &= -\frac{2\, p_{out} A_{out} u_{out}}{R T_{out}} \\ &\quad - \frac{f_{fric\_term}(p_{out}, T_{out}, u_{out} + \delta) - f_{fric\_term}(p_{out}, T_{out}, u_{out})}{\delta}\end{aligned} \tag{4.38}$$

$$(f_3)_{p_{out}} = \frac{\partial f_3}{\partial p_{out}} = \frac{f_3(p_{out} + \delta, T_{out}, u_{out}) - f_3(p_{out}, T_{out}, u_{out})}{\delta} \tag{4.39}$$

$$(f_3)_{T_{out}} = \frac{\partial f_3}{\partial T_{out}} = \frac{f_3(p_{out}, T_{out} + \delta, u_{out}) - f_3(p_{out}, T_{out}, u_{out})}{\delta} \tag{4.40}$$

$$(f_3)_{u_{out}} = \frac{\partial f_3}{\partial u_{out}} = -u_{out} \tag{4.41}$$

Note that δ represents a small finite value used when determining a derivative numerically. The root vector **r** is the vector containing the roots to the system of equations, i.e.

$$\mathbf{r} = [p_{root}\ T_{root}\ u_{root}]^T \tag{4.42}$$

where

$$f_1(p_{root}, T_{root}, u_{root}) = f_2(p_{root}, T_{root}, u_{root}) = f_3(p_{root}, T_{root}, u_{root}) = 0 \tag{4.43}$$

The guessed vector **g** containing the values of the guessed values of p_{out}, T_{out} and u_{out} is

$$\mathbf{g} = [p_{out,i}\ T_{out,i}\ u_{out,i}]^T \tag{4.44}$$

The difference vector **d** contains the differences between the root and guessed value for an iteration

$$\mathbf{d} = [p_{root} - p_{out,i}, T_{root} - T_{out,i}, u_{root} - u_{out,i}]^T \tag{4.45}$$

The partial derivatives are arranged into a matrix **A** as follows:

$$\mathbf{A} = \begin{bmatrix} \frac{\partial f_1}{\partial p_{out}} & \frac{\partial f_1}{\partial T_{out}} & \frac{\partial f_1}{\partial u_{out}} \\ \frac{\partial f_2}{\partial p_{out}} & \frac{\partial f_2}{\partial T_{out}} & \frac{\partial f_2}{\partial u_{out}} \\ \frac{\partial f_3}{\partial p_{out}} & \frac{\partial f_3}{\partial T_{out}} & \frac{\partial f_3}{\partial u_{out}} \end{bmatrix} \tag{4.46}$$

The solution equation is

$$\mathbf{A}\,\mathbf{d} = -\mathbf{g} \tag{4.47}$$

The above equation represents a linear system containing 3 simultaneous equations that must be solved for **d**. Once **d** has been solved for, the guess values to be used for the next iteration are calculated by adding **d** to the vector of previous iterations, i.e.

$$\mathbf{g}_{i+1} = \mathbf{g}_i + \mathbf{d}_i \tag{4.48}$$

The guess vector containing the new values $\mathbf{g}_{i+1}$ is used in the next iteration. This process is repeated until all elements in **g** are sufficiently close to 0. The solution of equation 4.47 was complicated by the fact that **A** tended to be *ill-conditioned* due to the fact that the governing equations had different units (continuity: kg/s, momentum: N, energy J). Mathematical techniques (*partial pivoting* and *scaling*) were employed to make it possible to solve equation 4.47. A discussion on the problem of ill-conditioning, partial pivoting and scaling can be found in appendix B.2.

4.2.3 Sonic Conditions in Throat

In order to use the method described in the section 4.2.2, it is necessary to know the sonic flow conditions in the nozzle throat. These are obtained by solving the momentum and energy equations between the stagnation conditions and the throat. The continuity equation is not used since the velocity of the flow under stagnation is taken to be zero. Hence, since one of the governing equations is not used, and it is still necessary to solve for 3 variables (p_{out}, T_{out}, u_{out}) another equation is required. The equation describing the speed of sound in an ideal gas was used. This is acceptable since it is shown (refer appendix A.1) that in the range worked in, butane behaves well as ideal gas. The speed of sound a in an ideal gas is given by

$$a = \sqrt{\gamma RT} \tag{4.49}$$

However, since it is known that in the throat the fluid velocity is Mach 1, i.e. the speed of sound in the fluid, the speed of sound a can be replaced with the sonic velocity u^* (= u_{out}). Doing this and rearranging so that the equation is in the form $f(x,y,z) = 0$ gives a new governing equation f_1 to replace the continuity equation:

f_1: sonic fluid velocity

$$u_{out} - \sqrt{\gamma R T_{out}} \tag{4.50}$$

The problem that needs to be solved can be stated as follows: given the stagnation conditions as the inlet conditions ($p_{in} = p_o$, $T_{in} = T_o$, $u_{in} \approx 0$) determine the sonic conditions (Mach number equal to 1) at the throat ($u_{out} = u^*$, $T_{out} = T^*$, $u_{out} = u^*$). The same iterative method for solving 3 simultaneous non-linear equations as described in section 4.2.2 previously was used. However, in this case the continuity equation (f_1)

was replaced by equation 4.50. For starting iterations the idealised equations presented in section 3.2 were used.

4.2.4 Supersonic Design Solution

Shock free supersonic flow through the diverging portion of the nozzle is referred to as the supersonic design solution. If the sonic flow conditions in the throat have been determined using the method described in section 4.2.3, then the supersonic design solution is obtained using the method described in section 4.2.2, and *marching* downstream from the nozzle throat to the exit. The starting conditions to use are the sonic conditions in the throat (refer section 4.2.3). However, it must be borne in mind that there are two sets of solutions that will satisfy the set equations describing the flow through the nozzle – a subsonic and supersonic solution. For the supersonic solution the pressure and temperature of the fluid must decrease in the diverging portion of the nozzle after the throat, whilst the velocity must increase. Thus, it is necessary to judiciously guess the values of p_{out}, T_{out} and u_{out} for the first iteration, otherwise the subsonic solution might be obtained instead of the supersonic solution. The following values were found to work well:

$$p_{out} = 0.9 \times p_{in} \tag{4.51}$$

$$T_{out} = 0.9 \times T_{in} \tag{4.52}$$

$$u_{out} = 1.1 \times u_{in} \tag{4.53}$$

4.2.5 Shock Wave Solution

4.2.5.1 Governing Equations for Shock Wave

A normal shock wave is assumed to occur over a very thin region, i.e. it occurs at a node and there are no area changes through the shock, i.e. $A_{in} = A_{out}$. The same governing equations for quasi one-dimensional flow (equations 4.7 to 4.9) apply, except that the area remains constant. Hence, the governing equations (equations 4.7 to 4.9) become:

continuity:

$$\rho_{in} u_{in} = \rho_{out} u_{out} \tag{4.54}$$

momentum:

$$p_{in} + \rho_{in} u_{in}^2 = p_{out} + \rho_{out} u_{out}^2 \tag{4.55}$$

energy:

$$h_{in} + u_{in}^2 / 2 = h_{out} + u_{out}^2 / 2 \tag{4.56}$$

Making use of the ideal gas approximation, the equations are rewritten in the form $f(x,y,x) = 0$:

$$f_1 = \frac{p_{in} u_{in}}{RT_{in}} - \frac{p_{out} u_{out}}{RT_{out}} = 0 \tag{4.57}$$

$$f_2 = p_{in} + \frac{p_{in} u_{in}^2}{RT_{in}} - p_{out} - \frac{p_{out} u_{out}^2}{RT_{out}} = 0 \tag{4.58}$$

$$f_3 = h_{in} + u_{in}^2 / 2 - h_{out} - u_{out}^2 / 2 = 0 \tag{4.59}$$

This results in a system of three non-linear equations that must be solved for p_{out}, T_{out} and u_{out}. This is done using the method discussed previously in section 4.2.2. In order to ensure convergence, reasonable guesses for the first iterations were required. The following values for the first iteration were found to work well:

$$p_{out} = stagnation\ pressure, p_o$$

$$T_{out} = stagnation\ temperature, T_o$$

$$u_{out} = 0.2\sqrt{\gamma R T_o}$$

4.2.5.2 Determining the position of shock wave

Consider the diagram in Figure 4.4. It is known that the flow in the throat is supersonic, there is a normal shock wave between the throat and the exit plane, and the flow at the exit plane is subsonic with the exit pressure equal to the back pressure. It is required to determine the position of the normal shock. With the position of the shock wave known the exit conditions can be calculated and hence the thrust estimated.

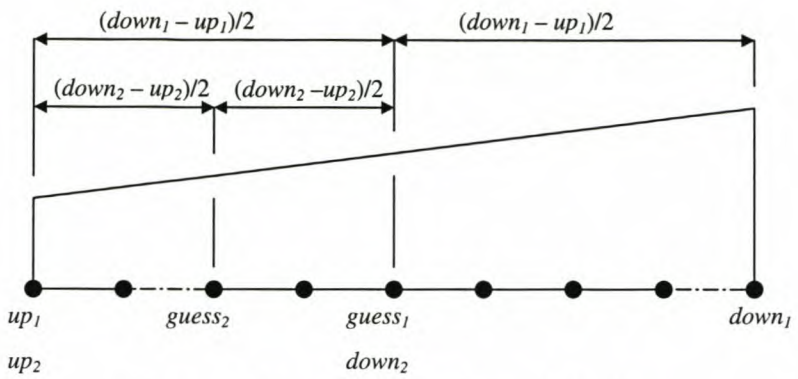

Figure 4.4 Determining position of shock wave

The position of the shock wave was determined iteratively using a type of bisection method. The diverging portion of the nozzle is divided into a number of equi-spaced nodes, with node 1 being at the throat (upstream node) and node n being at the exit (downstream node). These are set as the limits for the first iteration – up_1 and $down_1$ in Figure 4.4. It is guessed that the shock wave occurs halfway between these two nodes. The supersonic fluid properties at the node are known from the supersonic design solution (refer section 4.2.4). Using these properties, the properties after the shock are determined using the procedure described in section 4.2.5. This gives the subsonic properties after the shock. The remaining subsonic flow is solved for using the procedure described in section 4.2.6, in order to get the exit pressure. If this calculated exit pressure is less than the back pressure then the shock must occur further upstream. Thus, the downstream node for the next iteration ($down_{i+1}$) must be set equal to the guessed node of the current iteration ($guess_i$). If the calculated exit pressure is greater than the back pressure, then the shock must occur further downstream. Thus, the upstream node for the next iteration (up_{i+1}) must be set equal to the guessed node of the current iteration ($guess_i$). This process is repeated until the upstream and downstream nodes are adjacent to each other. The exit flow is then solved starting from both of these two nodes. The node that gives the closest exit pressure is taken to be the position at which the shock wave occurs. The exit velocity will also be solved for by a procedure that evaluates the subsonic flow downstream of the shock wave. The mass flow rate is still equal to the choked mass flow rate (section 4.2.3 discusses the calculation of the choked mass flow rate). Hence, the thrust can be calculated.

4.2.6 Subsonic Flow in Diverging Part of Nozzle

This procedure is used to solve for the subsonic flow in a diverging nozzle. Given the properties at a node, it *marches* downstream to the exit plane and solves the flow at each node. Since, it is exactly the same governing equations (continuity, momentum and energy) that are used to solve for the flow, the exact same procedure that was used to solve for the design condition is used. The only requirement is that the first iteration values for pressure, temperature and velocity must be judiciously chosen so that the subsonic case is solved for. Since, for subsonic flow in a diverging nozzle, pressure and temperature increase and velocity deceases, the starting values used were as follows:

$$p_{out} = 1.1 \times p_{in} \tag{4.60}$$

$$T_{out} = 1.1 \times T_{out} \tag{4.61}$$

$$u_{out} = 0.9 \times u_{in} \tag{4.62}$$

4.2.7 Procedure For Solving Fully Subsonic Flow Throughout Nozzle

If the back pressure is not sufficiently low to induce supersonic flow for a given nozzle at a given stagnation pressure (or conversely if the stagnation pressure is not high enough to induce supersonic flow for the given nozzle and back pressure) the flow will be subsonic throughout the nozzle. The case for fully subsonic flow was solved using one control volume. Given the stagnation conditions, the exit conditions were solved for directly without analysing the flow at any points between stagnation and exit. It is known the exit pressure must equal the back pressure. Hence, the only two unknowns are the exit temperature and velocity. Thus, two governing equations are required. The momentum and energy equations were used. These yielded a system of two simultaneous non-linear equations that were solved iteratively using the method discussed in section 4.2.2.

4.3 Transient Simulation Using Air as Propellant

Due to the many difficulties arising when attempting to simulate a thruster system employing butane as working fluid (phase changes and non-calorically perfect gas), initial simulations were conducted using air as the working fluid. Due to the fact that air can be accurately modelled using idealised gas dynamics, as well as the fact that phase changes were not expected in the regions it would be operating in, a one-dimensional transient simulation program using air as working fluid (*AirSim.exe*) was written. The results of this program could then be compared to experimental results.

4.3.1 Numerical Model

The thruster system was modelled as 3 separate control volumes (refer to Figure 4.5). The three control volumes were storage tank (1), accumulator (2) and valve chamber 3). In order to solve for the system the principles of conservation of mass and energy were applied to each control volume for each time step.

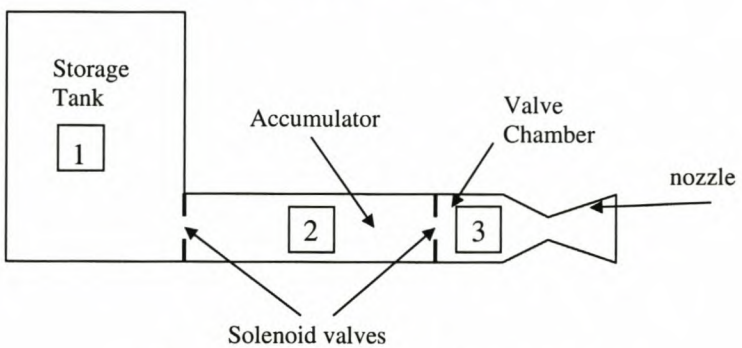

Figure 4.5 Schematic of thruster system

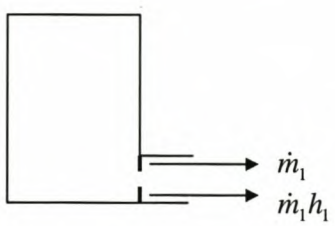

Figure 4.6 Control volume 1

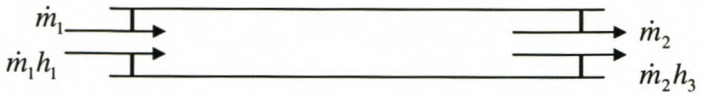

Figure 4.7 Control volume 2

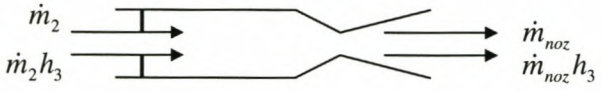

Figure 4.8 Control volume 3

The basic equations of conservation of mass and energy are (refer to equations 4.1 to 4.2 and assume adiabatic control volumes):

$$\frac{dm}{dt} = \dot{m}_{in} - \dot{m}_{out} \tag{4.63}$$

$$\frac{dE}{dt} = \dot{E}_{in} - \dot{E}_{out} \tag{4.64}$$

The derivatives are replaced by first order finite difference approximations using a finite time step Δt, hence:

$$\frac{m^{new} - m^{old}}{\Delta t} = \dot{m}_{in} - \dot{m}_{out} \tag{4.65}$$

$$\frac{E^{new} - E^{old}}{\Delta t} = \dot{E}_{in} - \dot{E}_{out} \tag{4.66}$$

Equations 4.65 and 4.66 can be rearranged to give explicit equations for the new values of mass and energy

$$m^{new} = m^{old} + (\dot{m}_{in} - \dot{m}_{out})\Delta t \tag{4.67}$$

$$E^{new} = E^{old} + (\dot{E}_{in} - \dot{E}_{out})\Delta t \tag{4.68}$$

Applying the above 2 equations to the system, and ignoring kinetic energy and potential energy, the energy E is given as mu, where u is the specific internal energy and is given by $u = C_v(T - T_{ref})$, the following set of equations describing the system are obtained:

conservation of mass (continuity equations)

$$m_1^{new} = m_1^{old} - \dot{m}_1 \, \Delta t \tag{4.69}$$

$$m_2^{new} = m_2^{old} + (\dot{m}_1 - \dot{m}_2)\Delta t \tag{4.70}$$

$$m_3^{new} = m_3^{old} + (\dot{m}_2 - \dot{m}_{noz})\Delta t \tag{4.71}$$

Conservation of energy

$$u_1^{new} = (m_1^{old} u_1^{old} - \dot{m}_1 h_1 \Delta t) / m_1^{new} \tag{4.72}$$

$$u_2^{new} = (m_2^{old} u_2^{old} + (\dot{m}_1 h_1 - \dot{m}_2 h_2)\Delta t) / m_2^{new} \tag{4.73}$$

$$u_3^{new} = (m_3^{old} u_3^{old} + (\dot{m}_2 h_2 - \dot{m}_{noz} h_3)\Delta t) / m_3^{new} \tag{4.74}$$

4.3.2 Calculation of Valve and Nozzle Mass Flow Rates

Before the new masses in the various control volumes can be calculated, it is necessary to calculate the various mass flow rates to and from the control volumes, i.e. $\dot{m}_1$, $\dot{m}_2$ and $\dot{m}_{noz}$. The first two are the flow rates through the solenoid valves. The method suggested by White (1999) for modelling flow through small orifices was used. This method assumes incompressible steady flow and also employs Bernoulli's equation. For flow through an orifice of diameter d, in a duct of diameter D, β is defined as:

$$\beta = \frac{d}{D} \tag{4.75}$$

For an upstream pressure p_1 and a downstream pressure p_2, and assuming incompressible flow with constant density ρ, the mass flow rate through an obstruction of throat area A_t is given by

$$\dot{m} = \rho C_d \, A_t \left[\frac{2(p_1 - p_2)/\rho}{1 - \beta^4} \right]^{1/2} \tag{4.76}$$

Where C_d is the dimensionless discharge coefficient and accounts for the discrepancies in the approximate analysis. For the simulations performed the value of C_d was taken as 0.6 (White, 1999).

For the flow through the nozzle, idealised gas dynamic theory (of section 3.2) was used to compute the mass flow. The exit Mach number can be computed from the known area ratios and area Mach number relation (equation 3.24):

$$\left(\frac{A_e}{A_t}\right)^2 = \frac{1}{Ma^2}\left[\frac{2}{\gamma+1}\left(1+\frac{\gamma-1}{2}Ma^2\right)\right]^{(\gamma+1)/(\gamma-1)} \tag{4.77}$$

This equation is not explicit in terms of *Ma* and hence had to be solved iteratively using bisection (refer to appendix B.2). With the exit Mach number known, the exit pressure, temperature, density and density could be calculated using Mach number relations (equations 3.13 to3.15). The speed of sound in the gas was calculated using the standard relation for sonic speed in an ideal gas,

$$a_e = \sqrt{\gamma R T_e} \tag{4.78}$$

From the definition of Mach number the exit velocity V_e is determined,

$$V_e = a_e\, Ma \tag{4.79}$$

Finally the mass flow rate through the nozzle is calculated,

$$\dot{m}_{noz} = \rho_e\, A_e\, V_e \tag{4.80}$$

The thrust delivered by the system is then

$$F_T = \dot{m}_{noz}\, V_e + A_e\left(p_e - p_B\right) \tag{4.81}$$

4.3.3 Basic Algorithm for Program

The basic algorithm for each time step of the simulation program was as follows:

1. Determine the mass flow rates through the solenoid valves and nozzle using equations 4.76 and 4.80 *old* properties.
2. Determine the new masses of propellant in the various control volumes from the continuity equations (equations 4.69 to 4.71)
3. Calculate the new specific internal energies of the control volumes from the energy equations (equations 4.72 to 4.74)
4. Determine the new temperatures of the control volumes from the specific internal energies calculated in 3

5. Determine the new densities of the various control volumes by dividing the new masses by the known volumes.
6. Calculate the new pressures in the control volumes from the ideal gas relation, $p = \rho RT$
7. Calculate the enthalpies of the control volumes from the temperatures (assume that energy and enthalpy are functions of temperature only)

4.4 Two-Phase Propulsion System Model

A mathematical model was developed in order to simulate the operation of a two-phase propulsion system. This system was similar to that described by Gibbon and Underwood (2001) in that the propellant (butane) was stored as a liquefied gas. The system was modelled as three separate control volumes, liquid (in storage tank), vapour (in contact with liquid in storage tank, accumulator (where vapour is superheated) and valve-chamber (the volume between the 2nd solenoid valve and the nozzle throat). A schematic diagram of the system is shown in Figure 4.9.

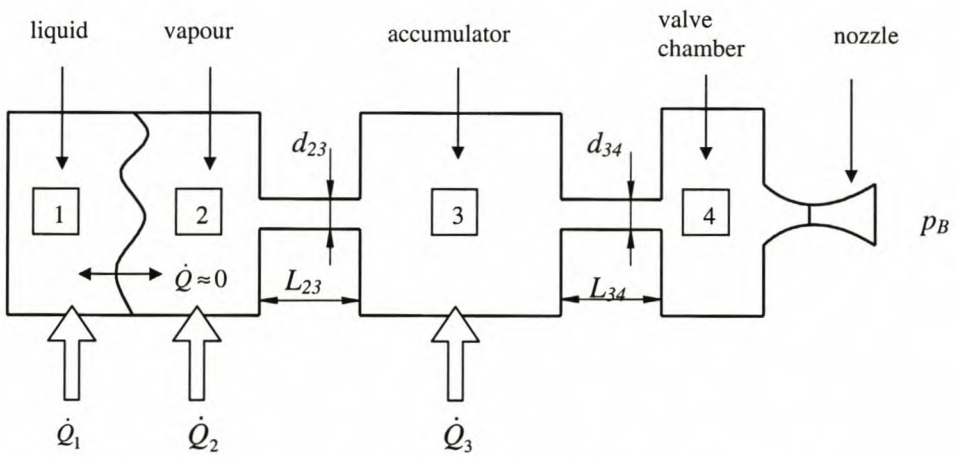

Figure 4.9 Diagram of two-phase propulsion system

The basic functioning of the system is as follows: the propellant is stored as a mixture of liquid and vapour propellant. Heating input to the storage tank ($\dot{Q}_1$ and $\dot{Q}_2$) provides energy to evaporate the liquid $\dot{Q}_1$ and some superheating of the vapour $\dot{Q}_2$, i.e. superheated vapour is allowed to co-exist with saturated liquid propellant without heat transfer between the two, and thus a state of non-thermodynamic equilibrium

exists. This phenomenon was discussed earlier in section 3.3. The vaporised propellant is fed to the accumulator control volume (3) where additional heat input $\dot{Q}_3$ can be provided to further superheat the propellant. The propellant is fed to the nozzle through a solenoid valve. The volume between the nozzle throat and solenoid valve is also modelled as a control volume (4) and is referred to as the valve chamber. The pressure builds up inside the valve chamber and flows through the nozzle to exhaust to the back pressure p_B. The two solenoid valves are modelled as tubes with diameters d_{23} and d_{34} (equal to that of the valve orifices). Lengths L_{23} and L_{34} are effective lengths used to account for the pressure drop over the solenoid valves.

4.4.1 Liquid Control Volume

A schematic diagram showing all mass and energy flows affecting the liquid control volume (1) is shown in Figure 4.10. It is assumed that there is no heat transfer between the liquid and vapour control volumes. Further it is assumed that the contact area between liquid and vapour A_{lv}, can be taken as the cross-sectional area of the tube in which the propellant is stored.

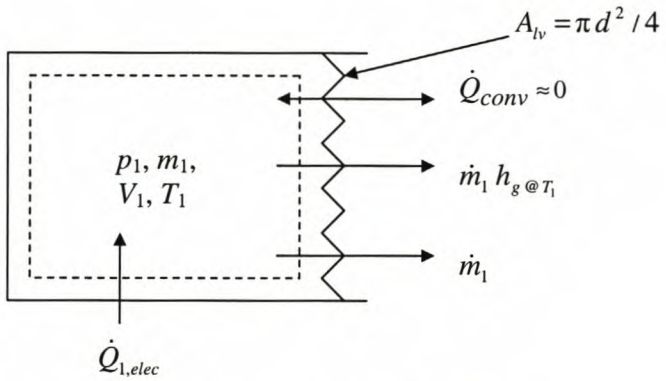

Figure 4.10 Analysis of liquid control volume

The mass transfer from the liquid to the vapour is due to phase change. This process was modelled as a non-equilibrium process, in which superheated vapour and sub-cooled liquid could co-exist at different temperatures without heat transfer taking place. This is discussed in more detail in section 3.3, where equation 3.35 is given to describe the mass transfer between liquid and vapour,

$$\dot{m}_1 = A_{lv}\, K\left[\frac{p_s}{\sqrt{T_s}} - \frac{p_v}{\sqrt{T_v}}\right] \tag{4.82}$$

Employing the numbering for control volumes indicated in Figure 4.9, equation 4.82 can be rewritten as

$$\dot{m} = A_{lv}\, K\left[\frac{p_{sat\,@\,T_1}}{\sqrt{T_1}} - \frac{p_2}{\sqrt{T_2}}\right] \tag{4.83}$$

For evaporation to occur, the vapour pressure p_v (or p_2) must be less than the saturation vapour pressure p_s ($p_{sat@T1}$), i.e. for $p_v > p_s$ equation 4.82 will be positive, implying that evaporation is occurring. The energy equation (equation 4.68) gives the new temperature of the liquid, T_1^{new}

$$T_1^{new} = T_1 + \frac{\Delta t}{m_1\, C_{vl_1}}\left(\dot{Q}_{1,elec} - \dot{m}_1\, h_{g\,@\,T_1}\right) \tag{4.84}$$

The new volume of the system is determined by simply dividing the mass of the system by its density,

$$V_1^{new} = m_1^{new} / \rho_{l\,@\,T_z^{new}} \tag{4.85}$$

4.4.2 Vapour Control Volume

The vapour control volume is adjacent to the liquid control volume, and under normal operation mass would enter the control volume from the liquid and exit the control volume through the solenoid valve. A schematic drawing of the vapour control volume is shown in Figure 4.11.

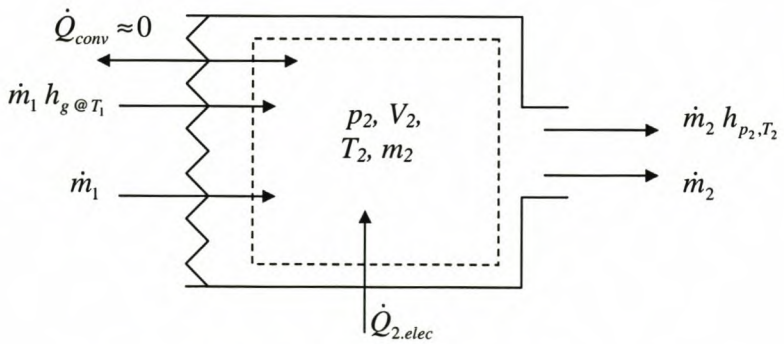

Figure 4.11 Analysis of vapour control volume

From continuity

$$m_2^{new} = m_2 + \Delta t\left(\dot{m}_1 - \dot{m}_2\right) \tag{4.86}$$

Note that $\dot{m}_2$ is the mass flow rate through the solenoid valve and the method used to determine it is discussed in section 4.4.3. From the energy equation, the new temperature of the vapour in the control volume is

$$T_2^{new} = T_2 + \frac{\Delta t}{m_2\, C_{v_2}}\left(\dot{m}_1\, h_{g\,@\,T_1} + \dot{Q}_{2.elec} - \dot{m}_2\, h_{p_2,T_2}\right) \tag{4.87}$$

The new volume is determined by subtracting the volume of control volume 1 from the total volume of control volumes 1 and 2

$$V_2^{new} = \left(V_1 + V_2\right)_{@\,t=0} - V_1^{new} \tag{4.88}$$

The ideal gas equation of state is used to calculate the new pressure of the control volume. The assumption was shown to be reasonable for the range of temperatures and pressures worked in (refer appendix A.1).

$$p_2^{new} = \frac{m_2^{new}\, R\, T_2^{new}}{V_2^{new}} \tag{4.89}$$

The density is determined by dividing the mass by volume

$$\rho_2^{new} = \frac{m_2^{new}}{V_2^{new}} \tag{4.90}$$

Due to the fact the control volumes 1 and 2 are adjacent to each other without any barrier between them, it follows that they must be at the same pressure, therefore

$$p_1^{new} = p_2^{new} \tag{4.91}$$

4.4.3 Accumulator

The control volume between the two solenoid valves is referred to as the accumulator. Its purpose was to provide more control over the state of the butane releasing the butane gas by opening the second solenoid valve. Heat input $\dot{Q}_3$ was provided to the control volume to increase the temperature (and hence the pressure) of the butane. A diagram of the control volume is presented in Figure 4.12.

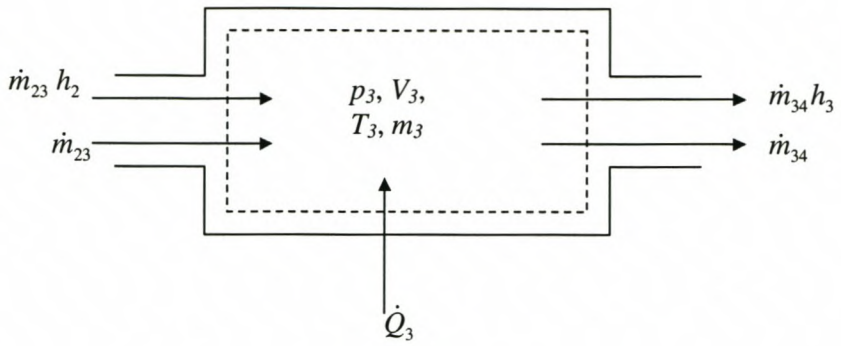

Figure 4.12 Accumulator control volume

From continuity

$$m_3^{new} = m_3 + \Delta t \left(\dot{m}_{23} - \dot{m}_{34} \right) \tag{4.92}$$

The new temperature of the control volume is determined from the conservation of energy principle (equation 4.68):

$$T_3^{new} = T_3 + \frac{\Delta t}{m_3 C_{v3}} \left(\dot{m}_{23} h_2 + \dot{Q}_3 - \dot{m}_{34} h_3 \right) \tag{4.93}$$

The ideal gas equation of state can be used to calculate the new pressure of the control volume:

$$p_3^{new} = m_3^{new} R T_3^{new} / V_3 \tag{4.94}$$

4.4.4 Valve Chamber

The valve chamber (control volume 4) is the final control volume through which the propellant passes before being expelled to the atmosphere. Propellant enters the valve chamber through the second solenoid valve and leaves through the nozzle throat. A schematic diagram of the valve chamber is shown in Figure 4.13, where $\dot{m}_{34}$ is the mass flow in through the solenoid valve and $\dot{m}_{noz}$ is the mass flow rate through the nozzle.

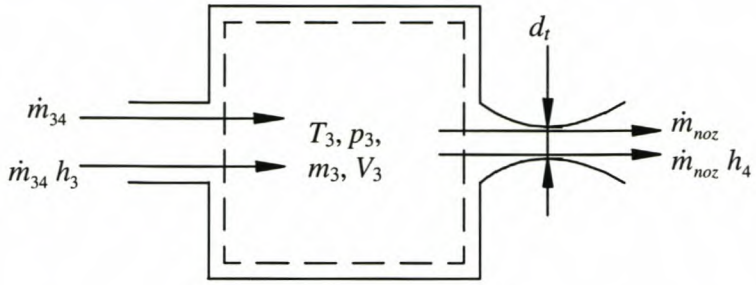

Figure 4.13 Analysis of valve chamber

The governing equations are obtained from the principles of conservation of mass and energy applied to a one dimensional explicit transient model (as discussed in section 4.1).

Hence, from continuity:

$$m_4^{new} = m_4 + \Delta t\left(\dot{m}_{34} - \dot{m}_{noz}\right) \tag{4.95}$$

Note that $\dot{m}_{noz}$ is the mass flow rate through the nozzle (throat diameter d_t) exhausting to the environmental back pressure, p_B, from the stagnation conditions inside the valve chamber. $\dot{m}_{noz}$ is a fairly complicated property to determine. Details of methods used to determine $\dot{m}_{noz}$, as well as the other exit properties are discussed in section 4.2. From the conservation of energy the new temperature of the control volume is:

$$T_4^{new} = T_4 + \frac{\Delta t}{m_4\, C_{v4}}\left(\dot{m}_{34}\, h_3 - \dot{m}_{noz}\, h_4\right) \tag{4.96}$$

Since the volume remains constant, with the new mass known, the density is easily obtained:

$$\rho_4^{new} = m_4^{new} / V_4 \tag{4.97}$$

4.4.5 Valves

Although the valve was not modelled as an actual control volume itself, it played an important role in the transfer of mass, momentum and energy between the accumulator and valve-chamber. A schematic diagram of the valve between control volumes 2 and 3 is depicted in Figure 4.14 (the analysis of the valve between control volumes 3 and 4 would be exactly the same). Note that the diameter d_{23} is a function

of time, and that the length of the valve L_{23} is not a physical length, but rather an effective length used to model the pressure drop over the valve.

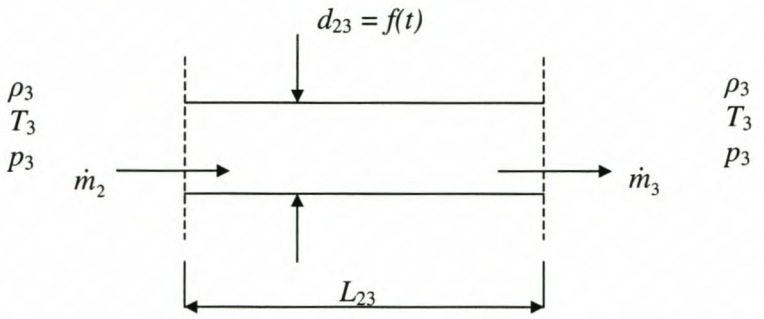

Figure 4.14 Analysis of valve

From continuity, and since it is assumed that no mass can be accumulated in the valve, the mass flow in must equal the mass flow out:

$$\dot{m}_2 = \dot{m}_3 = \dot{m}_{23} \tag{4.98}$$

The mass flow rate through the valve can also be expressed as the product of average density, velocity and area:

$$\dot{m}_{23} = \rho_{23}\, u_{23}\, A_{23} \tag{4.99}$$

where

$$A_{23} = \frac{\pi}{4} d_{23}^2 \tag{4.100}$$

The velocity through the valve is approximated by a correlation for viscous, incompressible flow in a tube:

$$V_{23} = \sqrt{\frac{2|p_2 - p_3|}{k\,\rho_{23}}} \tag{4.101}$$

It is important to note that the possibility of flow in both directions must be taken into account. Flow from volume 2 to volume 3 is defined as positive u_{23} and from volume 3 to volume 2 as negative u_{23}, i.e.

if $p_2 \geq p_3$ then $u_{23} = +u_{23}$

if $p_2 < p_3$ then $u_{23} = -u_{23}$

The average density is simply obtained by taking an average of the densities in volumes 2 and 3:

$$\rho_{23} = (\rho_2 + \rho_3)/2 \tag{4.102}$$

k is a dimensionless value used to account for the frictional and other pressure drops taking place over the valve:

$$k = f\, L_{23} / d_{23} \tag{4.103}$$

f is the Darcy friction factor, which is equal to 4 times the Fanning friction factor C_f. The equations used for estimating C_f depend on the value of the Reynolds number, Re. The value of the transition Reynolds number Re_{tr} is taken as 1209.76358. The reason for retaining so many decimal places for Re_{tr}, is to avoid possible convergence problems that could arise when the flow is very close to the transition point. From Whalley (1987) the expressions for C_f are:

Laminar flow (Re $\leq$ 1209.76358):

$$C_f = 16/Re \tag{4.104}$$

Turbulent flow (Re > 1209.76358):

$$C_f = 0.078\, Re^{-0.25} \tag{4.105}$$

The Reynolds number is given by the standard equation for calculating Re based on pipe diameter:

$$Re = \frac{\rho_{23}\, u_{23}\, d_{23}}{\mu_{23}} \tag{4.106}$$

μ_{23} is the average viscosity in the valve and is taken to be a function of the average temperature in the valve:

$$\mu_{23} = f(T_{23}) \tag{4.107}$$

where $T_{23} = (T_2 + T_3)/2$

4.4.6 Heat Input to Propellant

In the practical work conducted the heat input was provided by applying a voltage V over an electrical heating element, and the resulting heat generation was equal to V^2/R, where R is the resistance of the heating element. However, there are advantages in considering the use of a heat pipe to provide the necessary heat input. These advantages are discussed in section 8.8. A simple mathematical model of a heat pipe was used in the simulation to provide heat input to the propellant. Figure 4.15 depicts the use of a heat pipe in the storage tank: a heat pipe (diameter d) with the heated end at temperature T_{hot} is placed in the tank of butane at temperature T_{butane}, and the resulting heat transfer to the butane is $\dot{Q}$. The heat pipe is subdivided into three lengths: and evaporator section L_e where heat is transferred to the heat pipe, and adiabatic section L_{ad} where no heat transfer to or from the heat pipe occurs and a condenser section L_c where heat transfer from the heat pipe to the butane occurs.

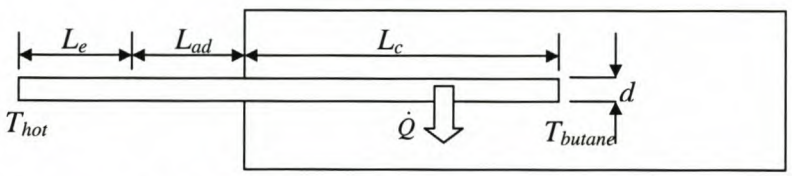

Figure 4.15 Use of a heat pipe in storage tank

The thermal resistance diagram for the situation depicted in Figure 4.15 is shown in Figure 4.16, where R_e and R_c are the thermal resistances of the evaporator and condenser sections respectively, h_e and h_c are the convective heat transfer coefficients of the heat pipe with the heat source and the butane, and A_e and A_c are the heat transfer surface areas of the evaporator and condenser areas.

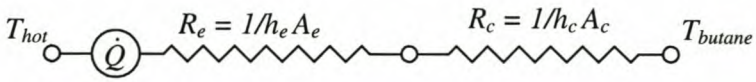

Figure 4.16 Thermal resistance diagram of heat pipe

The heat transfer rate to the butane $\dot{Q}$ is given by

$$\dot{Q} = \frac{\Delta T}{\sum R} = \frac{T_{hot} - T_{butane}}{1/h_e A_e + 1/h_c A_c} \tag{4.108}$$

where $A_e = \pi d_e L_e$ and $A_c = \pi d_c L_c$. d_e and d_c are the diameters of the heat pipe at the evaporator and condenser sections respectively. L_e and L_c are the lengths of the evaporator and condenser sections respectively. Typical values of h_e and h_c can be taken of being in the order of $h_e \approx h_c \approx 1000$ W/m^{2}K (Dobson and Scowby, 2003).

5 THRUST MEASUREMENT

Accurate determination of the thrust delivered was an important aspect of the experimental work. Due to the fact that thrust produced is relatively small (order of magnitude as low as 0.01 N) special consideration had to be given to the method used to measure the thrust as conventional methods to measure thrusts of much larger magnitudes are not appropriate because the resolution of such measurements is too coarse for the accuracy required. Some of the methods that have been used previously were discussed in section 2.3. The method that was employed is similar to that used by Ye et al. (2001) in that a cantilevered beam was used. However, whereas Ye et al. (2001) had the thruster firing onto the tip of the cantilevered beam, for the laboratory work conducted for this project the thruster was physically mounted to the end of the cantilevered beam. In addition the cantilever beam was the propellant tubing, similar to the method used by Mukerjee et al. (2000). The method that was used is described in more detail in section 5.1 which focuses on static thrust measurement. However, since the cantilevered tubing will be free to vibrate, attention to vibration characteristics is discussed in section 5.2. Sections 5.3 and 5.4 focus on practical aspects of the experimental work, strain gauge configuration and calibration.

5.1 Description of Method Used

The method used to measure thrust was to cantilever the tube carrying the propellant to the nozzle, and to measure the induced strain due to bending when the thrusters were fired. A schematic diagram of this measurement technique is shown in Figure 5.1. The tube carrying the propellant is cantilevered on one end. The other end is fitted with an elbow fitting causing a 90° change in direction of the propellant. Thus, the thrust force is at right angles to the cantilevered tube. This produces a tip load on the cantilevered tube resulting in a bending moment at the support of the cantilevered tube. Hence, the set-up is modelled as a cantilevered beam subjected to a tip load. By mounting a strain gauge on the cantilevered end the strain can be measured. The magnitude of the tip load that would have produced the strains measured can be determined using either traditional solid mechanics or by calibration.

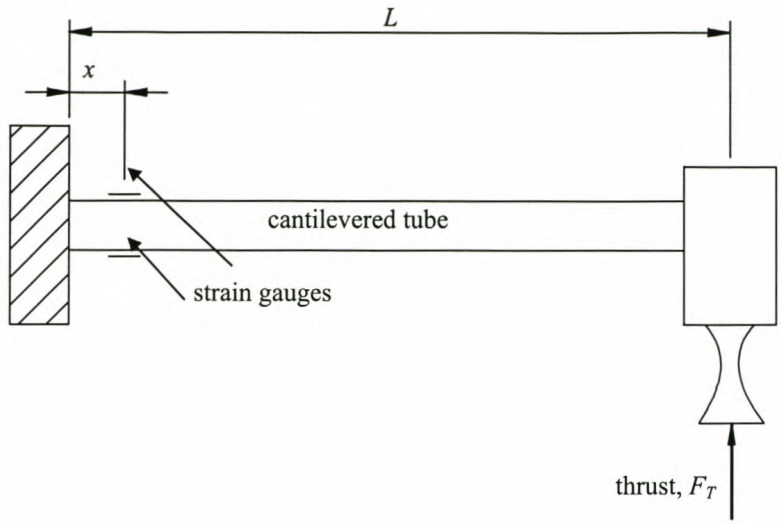

Figure 5.1 Method to measure thrust using cantilevered tube

The general equation for the bending moment M a distance x away from the fixed end, resulting from a tip load F on a cantilever of length L is:

$$M = F(L - x) \tag{5.1}$$

The resulting normal stress σ_x (in the axial direction) on the surface of the tube is:

$$\sigma_x = \frac{-M\,y}{I_{yy}} \tag{5.2}$$

where y is the distance from the neutral axis to the outer surface of the tube, and I_{yy} is the area moment of inertia about the y-axis.

From stress-strain relations (Benham, et al., 1999) the strain in the x-direction is given by:

$$\varepsilon_x = \frac{1}{E}\left(\sigma_x - \nu\left(\sigma_z + \sigma_y\right)\right) \tag{5.3}$$

where E is the Young's modulus of the material. For the moment the transverse stresses σ_z and σ_y will not be dealt with. However, due to the pressure inside the tube they will be present and thus would be regarded as a *contamination* effect on the thrust measurement. This is dealt with in section 5.4. Neglecting σ_z and σ_y, equation 5.3 reduces to

$$\varepsilon_x = \frac{\sigma_x}{E} \tag{5.4}$$

Re-arranging the above equations gives the following expression for the thrust force as a function of the strain:

$$F = \frac{-\varepsilon_x I_{yy} E}{(L-x)y} \tag{5.5}$$

Special considerations need to be taken into account when designing a measurement system that used equation 5.5. These include the effect of the tubing stiffness on the strain resolution and the approximations made in modelling the thrust force.

Effect of tubing stiffness on strain resolution

Due to the fact that the thrust is expected to be of a very small order of magnitude, careful consideration must be given to the parameters determining the stiffness of the measurement structure. The parameters affecting the bending stiffness of the tubing are the material, length and sectional inertia properties. The smallest strain that can be registered by a strain gauge is typically in the region of 0.5×10^{-6}. Choosing to have 10 data points requires that the strain developed be in the order of 5×10^{-6}. It is important to ensure that the set-up is not so stiff that no strain is registered when the thrust is produced. On the other hand it is also important that the set-up be stiff enough that the natural frequency of the cantilevered tube is not near to the frequency with which the solenoid valves are operated. This will be dealt with in more detail later on in section 5.2. The following sample calculation determines the expected bending strain ϵ_x for a thrust F_T of 0.01 N. The cantilevered tube is made from Perspex ($E = 3\times10^9$ N/m^2, with length $L = 0.14$ m, outside diameter $d_o = 0.013$ m, inside diameter $d_i = 0.010$ m). The strain gauge is mounted a distance x of 0.015 m from the cantilevered end.

Sectional moment of inertia: I_{yy}

$$I_{yy} = \pi\left(d_o^4 - d_i^4\right)/64 = \pi\left(0.013^4 - 0.01^4\right)/64 = 911.110\cdot10^{-12}\,[\mathrm{m}^4] \tag{5.6}$$

Expected strain, ϵ_x:

$$\varepsilon_x = -\frac{F(L-x)y}{I_{yy}E} = -\frac{(0.01)(0.14-0.015)(-0.0065)}{(911.110\times10^{-12})(3\times10^{9})} \tag{5.7}$$

$$= 2.973\cdot10^{-6} \quad [\text{m/m}]$$

Thus for a thrust of 0.01 N the expected strain using a single strain gauge to measure axial strain would be 2.973 μm/m, a value of almost 6 times higher than the minimum strain that strain gauges can measure. By using more than one active strain gauge in the bridge better resolution can be obtained. More details relating to the strain gauge bridge used are discussed in section 5.3.

Load approximations

The equations presented for the strain developed by a tip-loaded cantilever beam assume a point load – i.e. a load that acts on an infinitely small length of the beam. However, the diameter of the nozzle exit is finite, i.e. the thrust is distributed over a finite distance of the beam. The approximation of a tip-load is made. If more accuracy is required then the thrust may be modelled as a distributed load.

5.2 Vibration Characteristics

From solid mechanics it is known that a tip load suddenly applied and released to and from a cantilever beam will cause the beam to vibrate. Thus, performing thrust measurements as a function of time, one would expect to see a cyclic nature present in the measurements caused by the vibration of the cantilevered beam. Hence, it is necessary to determine the expected natural frequency of vibration in order to be able to compare it to experimental data. This was done in three ways:

- solution using analytical beam vibration theory,
- finite element solution using a FE package (Nastran), and
- experimental measurements.

5.2.1 Analytical Solution

An idealised model of the system is depicted in Figure 5.2. The elbow fitting, solenoid valve and nozzle were all modelled as a single lumped mass on the free tip of the cantilevered beam. It was required to find the lowest natural mode of vibration in the plane of the paper (the *xy*-plane in Figure 5.2).

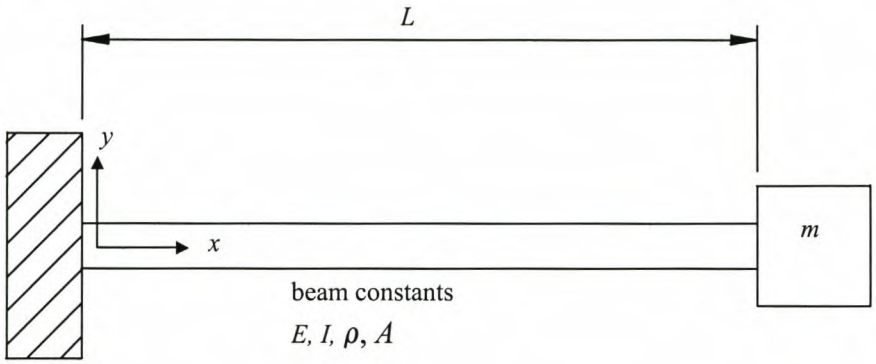

Figure 5.2 Idealised model of cantilever with tip mass

The theory dealing with the modelling of the bending vibration of a beam can be found in Inman (1995). The cantilevered beam will be modelled as an Euler-Bernoulli beam. The assumptions used in formulating this model are that the beam be:

- Uniform along its span and slender,
- Composed of a linear, homogeneous, isotropic elastic material without axial loads,
- Such that plane sections remain plane,
- Such that the plane of symmetry of the beam is also the plane of vibration so that rotation and translation are decoupled,
- Such that rotary inertia and shear deformation can be neglected.

It can be shown (Inman, 1995) that for a beam with constant E and I the free vibration is governed by

$$\frac{\partial^2 w(x,t)}{\partial t^2} + c^2 \frac{\partial^4 w(x,t)}{\partial x^4} = 0 \tag{5.8}$$

where E is Young's modulus of elasticity, I is the moment of inertia about the z-axis, w is the deflection in the y-direction, A is the cross-sectional area of beam and $c=\sqrt{EI/\rho A}$.

The free vibration equation (equation 5.8) contains four spatial derivatives and hence requires four boundary conditions in order to calculate a solution. The presence of the two time derivatives requires that two initial conditions, one for the displacement and one for the velocity be specified.

A separation-of-variables type solution is assumed – leading to a spatial and temporal equation. The boundary conditions required to solve the spatial equation are obtained by examining the deflection $w(x,t)$, the slope of the deflection $\partial w(x,t)/\partial x$, the bending moment $EI\partial w^2(x,t)/\partial x^2$, and the shear force $\partial[EI\partial^2 w(x,t)/\partial^2 x]/\partial x$. In this case a clamped-free configuration is being dealt with.

At the clamped end ($x = 0$) the deflection w and the slope must be equal to zero:

$$w(0,t)=0 \tag{5.9}$$

$$\frac{\partial w(0,t)}{\partial x}=0 \tag{5.10}$$

At the free end (with the point mass) the deflection and slope are unknown and one must examine the bending moment and shear force in order to obtain boundary conditions. If the mass moment of inertia of the tip mass at the free end ($x = L$) is negligible then the bending moment at the tip can be assumed to be zero, hence. This assumption of the mass moment of inertia being negligible will be made for the time being for convenience sake, but will be investigated both numerically using a finite element package and experimentally (refer Table 5.3).

$$EI\frac{\partial^2 w(L,t)}{\partial x^2}=0 \tag{5.11}$$

The expression for the shear force acting on the free end requires more careful consideration. Had there not be a mass at the free end the 2nd boundary condition would have been that the shear force is zero. However, since there is a mass at the free end, use must be made of Newton's 2nd law in order to determine the shear force,

based on the acceleration $\ddot{w}$ of the tip of the beam. From the separation-of-variables type solution assumed

$$\ddot{w}=X(x)\ddot{T}(t) \tag{5.12}$$

Since the T is a simple harmonic function

$$\ddot{T}(t)=-\omega^2 T(t) \tag{5.13}$$

Hence, from Newton's 2nd law

$$V(L,t)=EI\frac{\partial^3(L,t)}{\partial x^3}T(t)=m\ddot{w}=-m\omega^2 X(L)T(t) \tag{5.14}$$

Thus, the 2nd boundary condition at the free end is

$$EI\frac{\partial^3 w(L,t)}{\partial x^3}+m\omega^2 X(L)=0 \tag{5.15}$$

Two initial conditions (in time) must also be specified – these are normally the initial deflection and velocity profiles:

$$w(x,0)=w_0(x) \tag{5.16}$$

$$\frac{\partial w(x,0)}{\partial t}=\dot{w}_0(x) \tag{5.17}$$

A separation-of-variables type solution of the form $w(x,t) = X(x)T(t)$ is assumed. This leads to two equations – a temporal and spatial equation. The temporal equation is:

$$\ddot{T}(t)+\omega^2 T(t)=0 \tag{5.18}$$

This equation has a solution of the form

$$T(t)=A\sin\omega t+B\cos\omega t \tag{5.19}$$

where ω is the natural frequency of vibration. Constants A and B will be determined by the specified initial conditions.

The spatial equation is a fourth order equation:

$$X''''(x)-\left(\frac{\omega}{c}\right)^2 X(x)=0 \tag{5.20}$$

This equation has a solution of the form

$$X(x)=a_1 \sin \beta x+a_2 \cos \beta x+a_3 \sinh \beta x+a_4 \cosh \beta x \tag{5.21}$$

where

$$\beta^4=\frac{\omega^2}{c^2}=\frac{\rho A \omega^2}{EI} \tag{5.22}$$

The value for β and three of the four constants of integration a_1, a_2, a_3 and a_4 must be determined from boundary conditions. The fourth constant becomes combined with the constants A and B from the temporal equation, which are then determined from the initial conditions.

Substituting the boundary conditions at the clamped end (equations 5.9 and 5.10) yields

$$\begin{aligned} &X(0)=0 \Rightarrow a_2+a_4=0 \\ &X'(0)=0 \Rightarrow \beta(a_1+a_3)=0 \end{aligned} \tag{5.23}$$

The boundary conditions at $x = L$ result in

$$\begin{aligned} &EIX''(L)=0 \Rightarrow \\ &\beta^2\left(-a_1 \sin \beta L-a_2 \cos \beta L+a_3 \sinh \beta L+a_4 \cosh \beta L\right)=0 \end{aligned} \tag{5.24}$$

and

$$\begin{aligned} &EIX'''(L)+m\omega^2 X(L)=0 \Rightarrow \\ &a_1\left(-EI\beta^3 \cos \beta L+m\omega^2 \sin \beta L\right)+a_2\left(EI\beta^3 \sin \beta L+m\omega^2 \cos \beta L\right)+ \\ &a_3\left(EI\beta^3 \cosh \beta L+m\omega^2 \sinh \beta L\right)+ \\ &a_4\left(EI\beta^3 \sinh \beta L+m\omega^2 \cosh \beta L\right)=0 \end{aligned} \tag{5.25}$$

From the definition of β (equation 5.22) equation 5.25 becomes

$$\begin{aligned} &a_1\left(-\cos \beta L+D \sin \beta L\right)+a_2\left(\sin \beta L+D \cos \beta L\right)+ \\ &a_3\left(\cosh \beta L+D \sinh \beta L\right)+a_4\left(\sinh \beta L+D \cosh \beta L\right)=0 \end{aligned} \tag{5.26}$$

where

$$D=\frac{m\beta}{\rho A} \tag{5.27}$$

The four spatial boundary conditions yield four equations for the four unknown coefficients, writing in matrix-vector form

$$\mathbf{A}\,\mathbf{a}=\mathbf{0} \tag{5.28}$$

where

$$\mathbf{A}=\begin{bmatrix} 0 & 1 & 0 & 1 \\ \beta & 0 & \beta & 0 \\ -\beta^2\sin\beta L & -\beta^2\cos\beta L & \beta^2\sinh\beta L & \beta^2\cosh\beta L \\ \begin{pmatrix}-\cos\beta L \\ +D\sin\beta L\end{pmatrix} & \begin{pmatrix}\sin\beta L \\ +D\cos\beta L\end{pmatrix} & \begin{pmatrix}\cosh\beta L \\ +D\sinh\beta L\end{pmatrix} & \begin{pmatrix}\sinh\beta L \\ +D\cosh\beta L\end{pmatrix} \end{bmatrix} \tag{5.29}$$

$$\mathbf{a}=\left[a_1\ a_2\ a_3\ a_4\right]^T \tag{5.30}$$

Equation 5.28 can only have a nonzero solution for the vector if the coefficient matrix is singular. Hence, it is necessary to determine the values of β for which det(**A**) will be zero. It is possible to obtain an analytical expression for the det(**A**) = 0 and then to solve the problem numerically. However, in order to avoid the tedious algebra that this would entail, a Matlab routine (refer Appendix E.2) was used to solve for the values of β. The values of the following parameters were set as follows (Table 5.1):

Table 5.1 Parameters used for vibration analysis

Parameter	Value	Units
E	3×10^{9}	N/m^2
I	911.111×10^{-12}	m^4
A	54.1925×10^{-6}	m^2
m	0.2	kg
ρ	1.2	kg/m^3
L	0.14	m

Using the values shown in Table 5.1, the first value of β that satisfied the relation det(**A**) = 0, is $\beta_1=0.8645$.

Although there are an infinite number of values that will satisfy the relation det(**A**) = 0, only the first mode of vibration is of interest since only this mode is excited. Recalling, the definition of β given by equation 5.22, the first natural frequency is $f_1 = 24.31$ Hz.

5.2.2 Finite Element Solution

The first natural mode of vibration was also determined using a finite element package (*Nastran for Windows*). This was done in two ways. For the first way a simple cantilever beam with a point mass on the tip was used, i.e. the structure was modelled exactly the same as for the analytical solution. Hence, it was expected that the results between the two would be very close. The second model was more complicated and attempted to model the actual physical structure as accurately as possible. The structure was modelled using shell elements (*Nastran's plate elements*) to model the cantilevered tube. Solid elements were used in modelling the elbow, solenoid valve and nozzle. The natural frequency obtained from this model was expected to be the closest to that determined experimentally. The second FE model used is depicted in Figure 5.3.

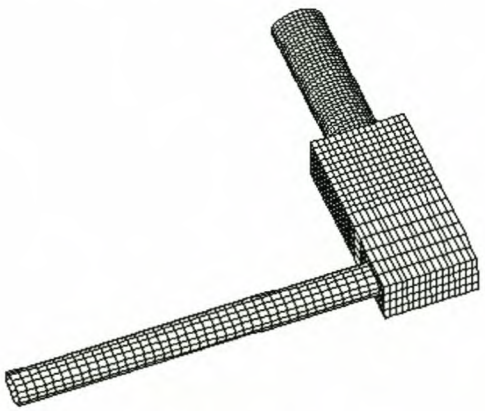

Figure 5.3 Complex FE model of set-up

The natural frequencies obtained by both FE models are presented in Table 5.2.

Table 5.2 Natural frequencies obtained using FEM

	First Natural Frequency [Hz]
Simple FE model	24.18
Complex FE model	20.23
Analytical calculation	24.31

It is seen that the results for the simple FE model and the analytical calculation are almost identical.

5.2.3 Experimental Result for First Vibration Mode

The first mode of vibration was determined experimentally by giving the structure an initial impulse (or deflection) and then by sampling the resulting measurements on the strain gauges. The number of cycles occurring in a certain time period could then be counted. Dividing the number of cycles completed by the time period during which they occurred would give the natural frequency:

$$f = \frac{Number\ of\ Cycles}{Time\ Period} \quad [\text{Hz}] \tag{5.31}$$

$$\omega = 2\pi f \quad [\text{rad/s}] \tag{5.32}$$

A graph depicting the resulting normalised strain in the cantilever against time following an impulse is shown in Figure 5.4. It can be seen that between time 0.50 and 1.00, 10 cycles occurred. Hence, the natural frequency of vibration can be determined:

$$f = \frac{10}{0.5} = 20 \quad [\text{Hz}]$$

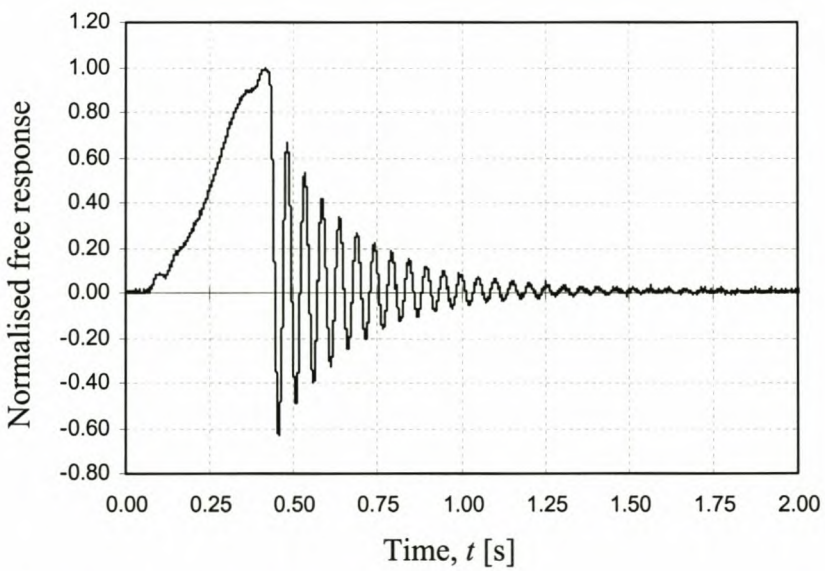

Figure 5.4 Free response of beam, model I

Comparing this result to those obtained analytically and numerically (Table 5.3) indicates excellent agreement between the complex FE model and the experimental result. It can be seen by the relatively large difference (approximately 20 %) between the results obtained using analytical calculation and simple FE model compared to the complex FE model and the experimental verification. The analytical calculation and the simple FE model did not account for the mass moment of inertia whereas the complex FE model and the experimental model did. Hence, it is clear that the assumption made in equation 5.11 and in the simple FE model (that the mass moment of inertia of the tip mass is negligible) was inaccurate.

Table 5.3 Comparison of results for 1st natural frequency

	First Natural Frequency [Hz]
Experimental	20
Analytical	24.31
Simple FE	24.18
Complex FE	20.23

5.2.4 Structural Damping

By examining the graph in Figure 5.4 it is seen that the amplitude of vibration decreases rapidly with time. This decaying amplitude is due to the damping present in the material. It is this damping which causes the vibration to ultimately terminate. In this case the amplitude of vibration has been normalised so that the amplitude at time equal to zero is equal to unity, and dividing all amplitudes by the actual measured value at time equal to zero. The amplitude A of a damped response is given by

$$A(t) = A_0 \, e^{-\zeta \omega t} \tag{5.33}$$

Where A_0 is the initial amplitude at time equal to zero, ω is the natural frequency vibration in [rad/s] and ζ is the damping coefficient. The value of the damping coefficient was determined by making use of the logarithmic decrement δ, defined as:

$$\delta = \ln\left(x(t) / x(t + nT)\right) \tag{5.34}$$

where T is the period of oscillation and n as a positive integer. It can be shown (Meirovitch, 1967) that if the value δ is known, then ζ can be calculated using the following equation:

$$\zeta = \frac{\delta}{\sqrt{4\pi^2 n^2 + \delta^2}} \tag{5.35}$$

The damping coefficient ζ is determined using equations 5.34 and 5.35 as well as the graph in Figure 5.4. The value of the first negative peak (-0.60) is used as the value of $x(t)$. The value of the 10th peak after this one (-0.07) is used as the value of $x(t + nT)$, where n equals 10. Using equation 5.34, the value of δ is:

$$\delta = \ln(-0.60/-0.07) = 2.148$$

The value of ζ is determined from equation 5.35:

$$\zeta = \frac{\delta}{\sqrt{4\pi^2 n^2 + \delta^2}} = \frac{2.148}{\sqrt{3952.45}} = 0.034$$

This value of the damping coefficient can be used in a FE package when conducting a modal transient analysis to simulate the behaviour of the cantilevered thruster structure. The natural frequency at which this damping coefficient occurs is known (refer to sections 5.2.1 to 5.2.3). It can be assumed that this damping coefficient is valid in a range of natural frequencies that includes the first natural mode of vibration. The calculated value of ζ can be incorporated into the FE model using a modal damping table. However, this was not done for this project.

5.3 Strain Gauge Configuration

Thrust measurements were made by cantilevering the accumulator tube and attaching strain gauges onto the tube. Two strain gauges were attached opposite each other in order to form a temperature compensated half bridge.

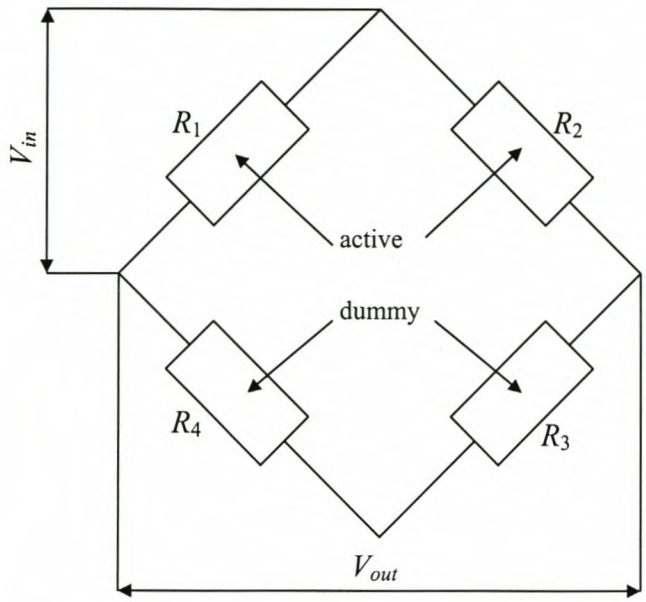

Figure 5.5 Strain gauge configuration to measure thrust

A diagram of a half bridge configuration is depicted in Figure 5.5. Note that only R_1 and R_2 are active strain gauge resistances. R_3 and R_4 are merely additional resistances (within the bridge amplifier) used to complete the Wheatstone bridge.

The general equation for the output voltage V_{out} given a change in the resistances ΔR of the strain gauges, for an input voltage V_{in} applied over the bridge is (Boctor et. al, 1997):

$$\frac{V_{out}}{V_{in}} = \frac{1}{4}\left[\frac{\Delta R_1}{R_1} - \frac{\Delta R_2}{R_2} + \frac{\Delta R_3}{R_3} - \frac{\Delta R_4}{R_4}\right] \tag{5.36}$$

The basic strain gauge equation is given by

$$\frac{\Delta R}{R} = K\varepsilon \tag{5.37}$$

where K is the gauge factor (equal to 2 for the strain gauges used). In the bridge considered, resistors R_3 and R_4 do not take part in the deformation, and equation 5.36 becomes:

$$\frac{V_{in}}{V_{out}} = \frac{K}{4}\left[\varepsilon_1 - \varepsilon_2\right] \tag{5.38}$$

Gauges 1 and 2 were mounted directly opposite each other on the cantilevered tube, hence they experienced the same magnitude of strain in the axial direction but of different sign, i.e.:

$$\varepsilon_1 = -\varepsilon_2 = \varepsilon_x \tag{5.39}$$

Hence, the ratio of input over output voltage would be:

$$\frac{V_{out}}{V_{in}} = \frac{K}{4}[2\varepsilon_x] = \frac{K}{2}\varepsilon_x \tag{5.40}$$

It is easily shown that this bridge is temperature compensated. Assume a strain due to bending of the cantilever of $\varepsilon_1 = \varepsilon_x$ and $\varepsilon_2 = -\varepsilon_x$. Additionally assume a strain induced due to temperature of ϵ_T in both gauges. Hence, the strains experienced in gauge 1 and 2 are as follows:

$$\varepsilon_1 = \varepsilon_x + \varepsilon_T \tag{5.41}$$

$$\varepsilon_2 = -\varepsilon_x + \varepsilon_T \tag{5.42}$$

Substituting the above two expressions into equation 5.38 gives the following expression, which is exactly the same as that given in equation 5.40:

$$\frac{V_{in}}{V_{out}} = \frac{K}{4}[(\varepsilon_x - \varepsilon_T) - (-\varepsilon_x + \varepsilon_T)] = \frac{K}{2}\varepsilon_x \tag{5.43}$$

An additional advantage of this bridge is that it compensates for axial strains experienced due to internal pressure inside the Perspex tube. An internal pressure in the tube will create an axial force equal to the product of the tube area and the internal pressure. The exact same method that was used to show that the bridge is temperature compensated can be used to show that the bridge is pressure compensated, by replacing ϵ_T (thermal strain) with ϵ_p (pressure strain) in the derivation. This would be the case if it were possible to align the gauges perfectly with the axis of the tube. However, in practice there will be some slight misalignment meaning that when the tube has an internal pressure there will be an induced output voltage over the bridge, despite thrust being applied to the cantilevered tube. This effect was examined and calibrated experimentally – for details refer to section 5.4. For the strain gauges used, the gauge factor K is equal to 2, therefore equation 5.40 becomes:

$$\frac{V_{out}}{V_{in}} = \varepsilon_x \tag{5.44}$$

For the bridge amplifier used the voltage applied across the bridge V_{in} equals one Volt, and hence the expression for output voltage V_{out} becomes:

$$V_{out} = \varepsilon_x \tag{5.45}$$

The theory presented in this section would be used if it was required to calculate the value that the calibration signal on the bridge amplifier must be set to. The calculations for determining the calibration factor can be found in appendix C.1. However, for the experimental work conducted in this project the calibration signal was set to the maximum value of 10 V and the cantilevered arm was calibrated by hanging mass pieces from it – refer to section 5.4.

5.4 Calibration of Thrust Force

The previous section presented a theoretical method to calibrate the thrust measurement strain gauges. However, due to inevitable experimental errors the actual calibration was done experimentally. The experimental errors could be due to slight misalignment of strain gauges – the gauges may not be aligned perfectly with the beam axis, might not be exactly opposite each other and might not be exactly at right angles to the thrust. Additional errors could be due to slight local stress concentrations on the material to which the strain gauges were attached. The strain gauges were attached by fusing them to the perspex using a chloroform solution.

Experimental calibration was done by hanging mass pieces from a string that was aligned as accurately as possible to the nozzle axis. The force was calculated by multiplying the mass of the mass piece by the gravitational acceleration g (9.81 m/s^2). The resulting strain was measured for each applied force and a plot was made of force against the recorded output voltage. A straight line was obtained by performing a least squares fit on the data to give the calibration equation. The plot of force against voltage can be seen in Figure 5.6 along with the calibration equation. The calibration equation for the thrust F_T in N as a function of voltage V in V was:

$$F = 0.4385 \cdot V - 0.0006 \qquad [\text{N}] \tag{5.46}$$

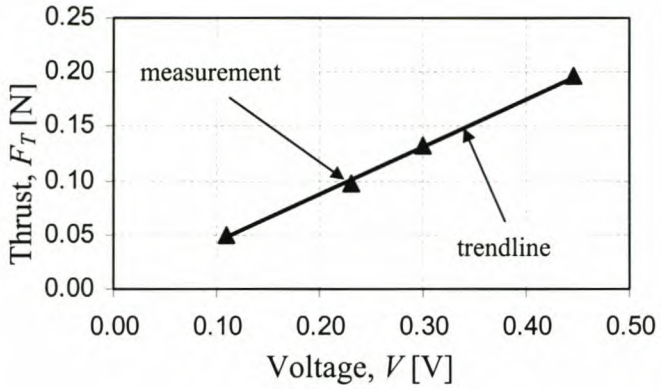

Figure 5.6 Thrust calibration graph

It is also useful to check the error between experimental and theoretical results for the strain gauges by calculating the calibration factor using the theory presented in section 5.3. The calibration factor on the strain gauge is set to this value and then known forces are applied to the cantilever, the results are recorded and compared to what was expected theoretically. This was done in appendix C.1 and the results can be found in Table C.2.

It was mentioned in section 5.3 that although for the bridge configuration used, theoretically axial strains due to internal pressure should cancel each other out, a certain amount of alignment error was expected with the implication that internal pressure might possibly contaminate thrust measurements. Fortunately this problem could be alleviated by calibration of this effect. In order to do this the system was pumped full of air to a pressurised state. The fill valve was left slightly open so as to allow the pressure to drop. No forces were applied to the cantilevered tube. While the pressure was being released both the output voltages for the pressure and thrusts-sensing bridges were sampled. A plot was then made of V_{out} of the thrust-sensing bridge versus the internal pressure in the tube. A least squares fit was then done on the data in order to provide an equation correlating the error in the thrust-sensing bridge V_{out_error} with the internal pressure p_i inside the tube. The graph showing the data points from which this correlation was obtained is shown in Figure 5.7. The following equation was obtained:

$$F_T = 3.460 \times 10^{-5} p - 0.0007 \quad [\text{N}] \tag{5.47}$$

The units for p must be kPa. The induced thrust value due to internal pressure was of the opposite sign to the thrust resulting from gas flow through the nozzle, i.e. – an internal pressure in the accumulator would result in a lower thrust reading. Note that in Figure 5.7 that the pressure reading is in fact the difference pressure increase above the pressure at which the strain gauge on the cantilever arm was zeroed. For a bridge zeroed at 100 kPa ambient pressure, a 200 kPa increase (i.e. an internal pressure of 300 kPa) would result in a error thrust reading of approximately 0.005 N. For the butane results presented in section 7.4 it can be seen that the maximum pressure increase or decrease ever experienced in the accumulator was not much more than 100 kPa (see for example Figure 7.13, Figure 7.14 and Figure 7.16. It can be seen from the graph in Figure 5.7 that a 100 kPa internal pressure change would result in a change 0.0025 N. This value is typically only about 5 % percent of the peak thrust (and the peak thrust would occur at the time of maximum pressure increase in the accumulator). Hence, the effect of internal pressure on thrust was ignored as it was decided that the additional effort in adjusting the calibration equation was not worth a maximum of 5 % increase in experimental accuracy. In addition it can be seen in Figure 5.7 the experimental data used to generate the trendline is scattered about the trnedline with an amplitude of approximately 0.002, indicating a significant amount of variance in the data.

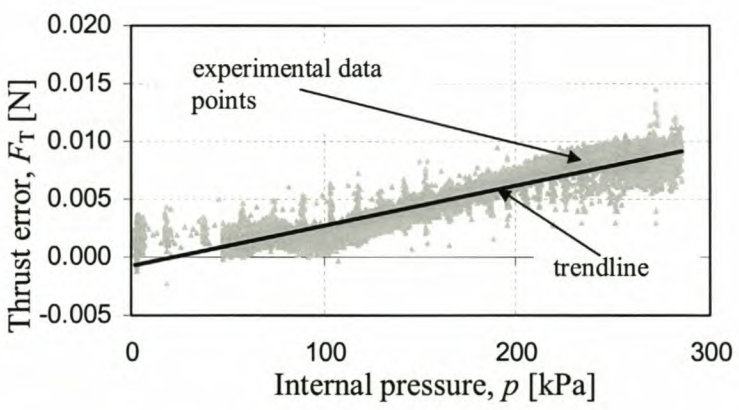

Figure 5.7 Effect of internal pressure on thrust

6 EXPERIMENTAL WORK

6.1 Description of Experimental Work

The design, manufacture and testing of a breadboard model was done in order to verify thruster performance. This would make it possible to compare theoretical predictions with experimental results. Tests were carried out under both ambient and near-vacuum conditions in a vacuum chamber. Most of the model was constructed from perspex to make it possible to observe the propellant behaviour inside the tank and tubing. In particular it was desired to observe the boiling and two-phase flow behaviour of the working fluid. A schematic of the experimental model is shown in Figure 6.1.

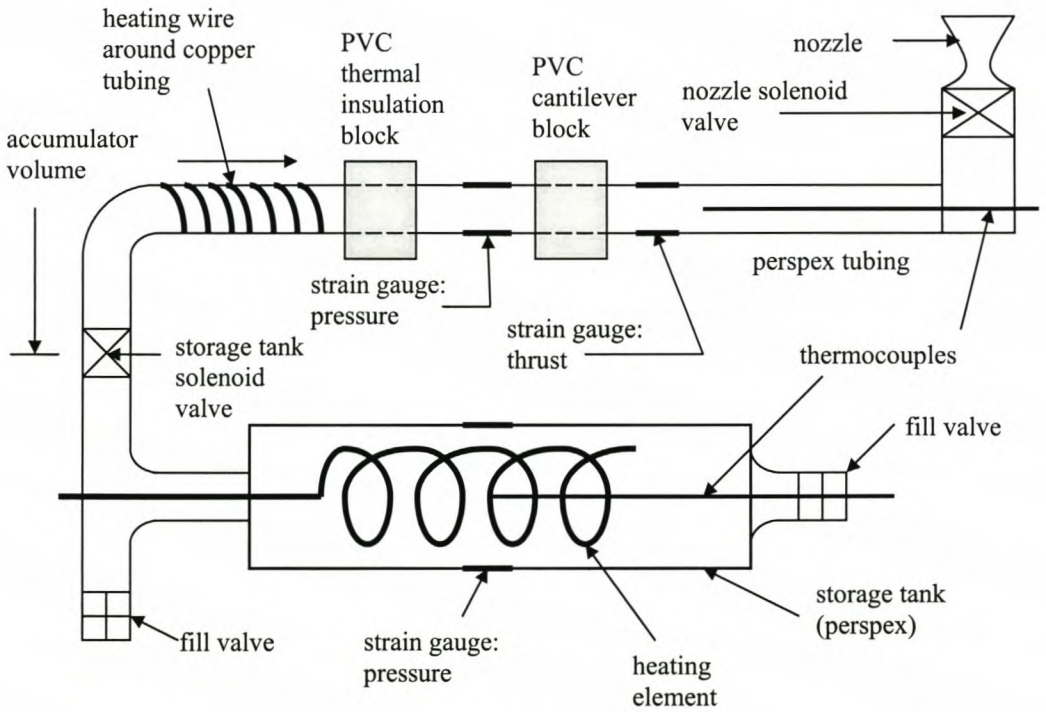

Figure 6.1 Schematic diagram of experimental model

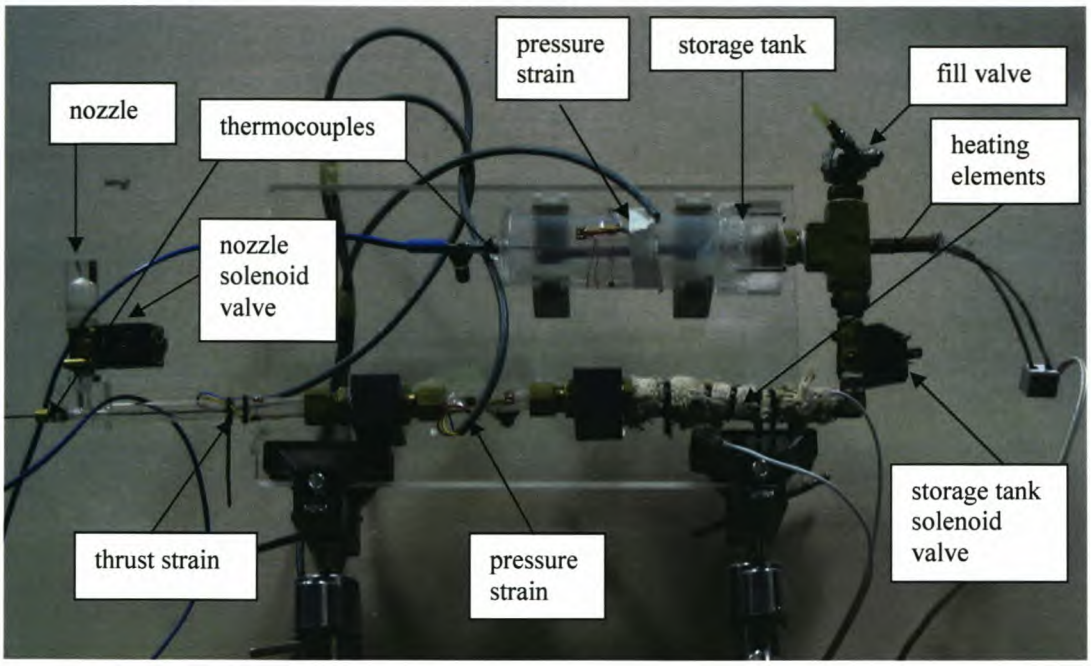

Figure 6.2 Photograph of experimental model

The basic operation of the system was as follows. The storage tank was filled with liquid butane. The first solenoid valve was opened and liquid fed to the heating chamber (accumulator) – usually until the pressures in the heating chamber and storage tank equalised. The saturation temperatures of butane are relatively low (compared to water) - at 200 kPa the saturation temperature is 20 °C and at 300 kPa it is 32 °C. The typical room temperature at which testing was conducted was 20 °C. Thus, for the butane at a pressure lower than approximately 200 kPa, boiling would commence due to heat transfer from the surrounding air to the butane. When the propellant was fed to the accumulator chamber it resulted in a decrease in pressure (due to an increase in volume) that further lowered the saturation temperature. The model was fitted with two sources of electrical heating energy. A heating element was placed inside the storage tank. The first heating element was constructed by placing a length of resistance heating wire inside a copper tube. A hole was drilled into the tee-piece connected to the storage tank. The heating element was pushed through this hole and soldered to the tee-piece. The second heat element was made by winding resistance heating wires around the copper tubing through which the propellant was fed. The resistance heating wires were electrically insulated from the copper using ceramic beads. In addition the resistance heating wire on the outside of the copper tube was thermally insulated from the environment using asbestos insulation tape. Both heating elements were connected to a variable power supply.

Hence, the heat input to the system can be controlled. The boiling propellant resulted in an increase in temperature and pressure that were monitored. Superheating of the vapour also occurred depending on the amount of heat input and the vapour pressure. Once a satisfactory state of pressure had been reached the second solenoid valve was opened, allowing the propellant to flow out the nozzle creating a thrust on the tube in the opposite direction to that of the flow.

Operation of the system and data capturing was done on a personal computer through computer programs developed in *LabVIEW* (refer to appendix D for more details). The normally closed solenoid valves required a 24 V direct current power supply to facilitate opening. The valve used for the nozzle solenoid valve was a *Sirai* (*direct acting, normally closed, 1/8") solenoid valve* with an orifice diameter of 1.6 mm (type Z610A). The storage tank solenoid valve was a *Parker (direct acting, normally closed, 1/8") solenoid valve* with an orifice diameter of 2.8 mm (type VE 131 – VE 161). Both valves were fitted with teflon seals since these would not be adversely affected by butane. Control of the valves is discussed in section 6.2.1.

It was necessary to measure and record the following data:

- Temperature and pressure in the storage tank
- Temperature and pressure in the accumulator
- Thrust delivered by the system

Measurements of thrust were discussed in section 5. Temperature measurements are discussed in section 6.2.2 and pressure measurements in section 6.2.3.

6.1.1 Initial Calibrations and Experiments

Before accurate testing and measurement of the system could begin, a number of calibrations and experiments were carried out in order to determine some of the physical parameters of the system as well as to check the accuracy of the measurements recorded.

The physical parameters experimentally investigated were the following:

- stiffness of the cantilevered thruster structure
- natural frequency and damping of the cantilevered thruster structure

The calibration experiments performed were the following:

- calibration of thrust force (refer section 5.4)
- calibration of strain gauge bridges to measure pressure (refer section 6.2.3)
- effect of opening and closing the solenoid valves on the system, i.e. observing what strains were recorded when the solenoid valves were opened and closed with no propellant inside the system (refer section 6.3.1)
- effect of DAQ card on temperature and strain measurements (refer section 6.2.4 and 6.2.5)

6.1.2 Use of Strain Gauges

Strain gauges were used for the measurement of thrust and internal pressure. Although the use of strain gauges is commonplace, due to the fact that the material on which the strain gauges were mounted was perspex, a number of additional considerations had to be taken into account. The strain gauges could not be glued to the perspex as would normally be done with steel. Rather, the strain gauges had to be fused to the perspex using chloroform. Additionally, due to the fact that perspex is a poor conductor of heat, consideration was given to the possibility of adverse effects due to localised heating resulting from the electrical heating input to the strain gauges. Strain gauges with a high resistance (350 Ω) were used in order to minimise Joule heating effects. Additionally, relatively small strain gauges could not be used, as the heat generation would occur over a very small area. A larger gauge would spread the heat input over a bigger area and decrease the effect of a local hot spot at the point where the strain gauge is attached. A local hot spot would occur if the electrical heat input to the strain gauge could not be removed from the strain gauge by conduction and convection.

6.2 Measurement and Control

Experimental work required accurate measurement and control of the system through a personal computer (PC). It was also required to control the opening and closing of valves with accuracy of under 10 ms. All measurement and control through the PC were done using commercially available data acquisition hardware and software. The input / output (I/O) hardware used was a *National Instruments PCI-6014 basic multifunction DAQ board* (serial number 188626D-01). The software used for communication with the I/O device was *LabVIEW 6.1*.

6.2.1 Control of Solenoid Valves

The solenoid valves used required a 24 V direct current voltage to open. The power input terminals of the valves were connected to a relay board. The relay board was supplied with an input of 24 V direct current from a power supply. The power supply was plugged into a 220 V alternating current wall socket. The relay switches required a 5 V signal to send power to a valve. This 5 V signal was sent to the relay board from the multifunction I/O card in the personal computer. A diagram of the control system is shown in Figure 6.3. The power rating of the valves was 6 W, thus typical current drawn by the valves was about 0.25 A.

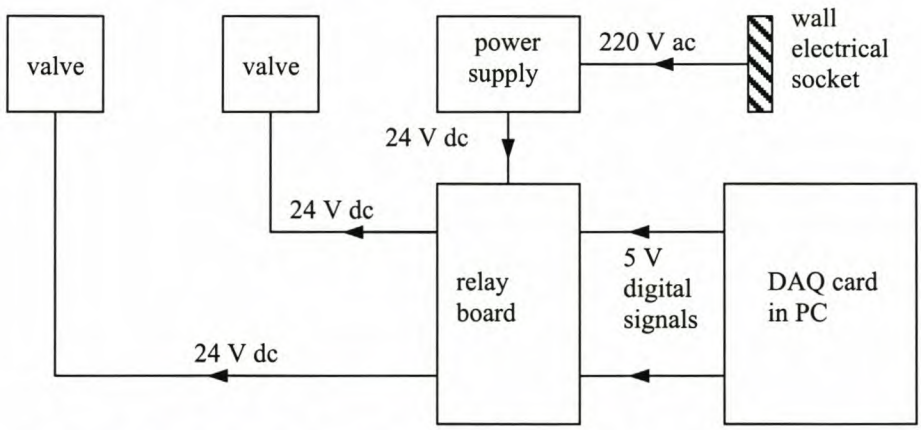

Figure 6.3 Diagram of valve control system

The valve control sequence developed in LabVIEW allowed the user to operate the valves in a pulsed fashion. The user would need to specify how many cycles were required, the "on-time" during each cycle and the "off-time" during each cycle. Refer

to Figure 6.4 for a sketch of a pulsed thrust along with the terminology used. Code for the control algorithm can be found in appendix D.

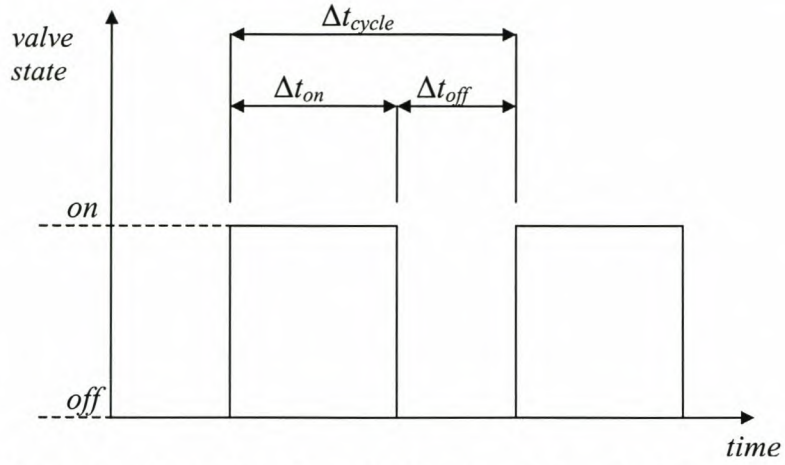

Figure 6.4 Illustration of terminology used for pulsed-thrust operation

6.2.2 Temperature Measurement

Copper-constantan (type T) thermocouples were used for conducting measurements. Although the use of thermocouples is fairly standard, special attention had to be given to the wiring out of the vacuum chamber. Feed-throughs were manufactured which accommodated both copper and constantan wires, to avoid creating a new thermocouple at the junction point. The voltage difference was read in as a differential voltage on one of the channels of the I/O card using the configuration software that was supplied with the card to automatically convert the voltage differences to temperature units °C. An ice-bucket was used as to create a reference point at 0 °C for one of the junctions since the software required that one junction be at a known temperature. Refer to Figure 6.5 for a photograph of the feed-throughs and ice-bucket.

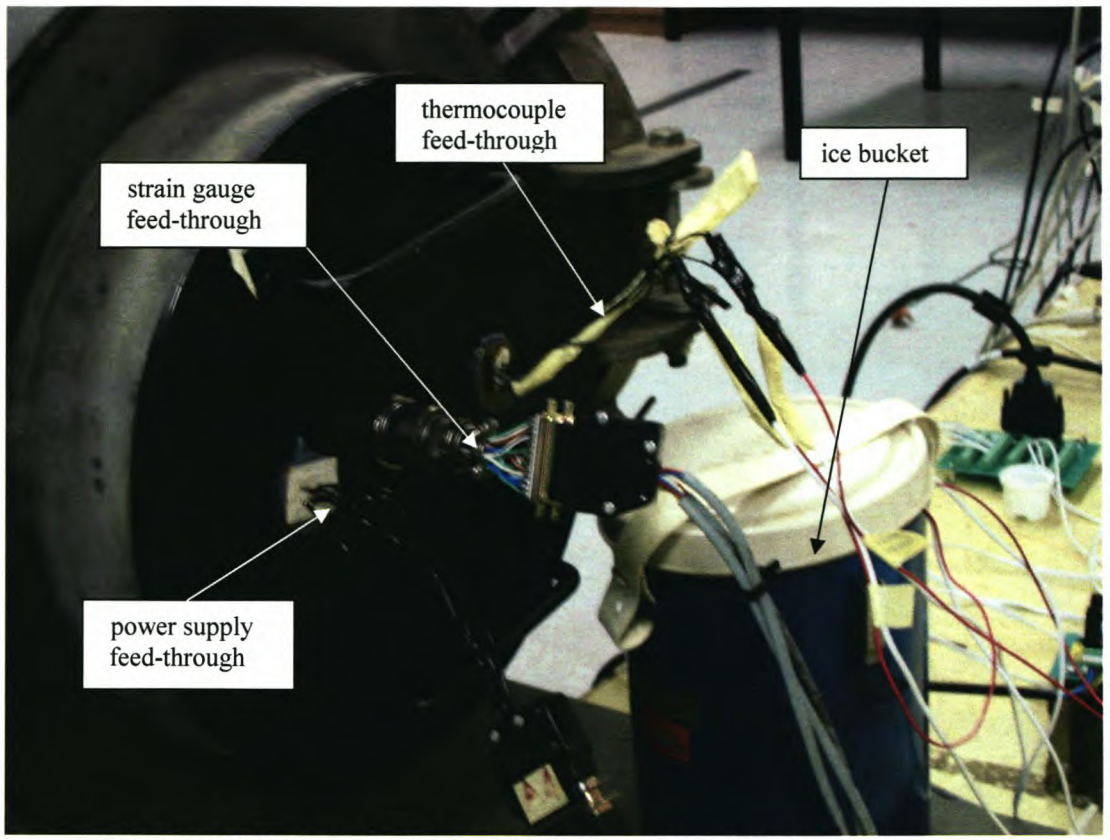

Figure 6.5 Photograph showing feed-throughs and ice bucket

6.2.3 Pressure Measurement

Pressure measurements were made using strain gauges on both the storage cylinder and accumulator. Although pressure transducers could also have been used, their use would have required that connection ports be drilled and fitted onto the storage tank and accumulator. This would have created potential leakage problems. Additionally, pressure gauges are much more expensive that strain gauges. Strain gauges provided a simpler and cheaper option with minimal loss of accuracy. By knowing the strain in a cylindrical pressure vessel, the internal pressure can be determined in the following ways:

- Analytically – i.e. thick walled pressure vessel theory
- Numerically – using a commercially available finite element package
- Experimentally – calibrating the strain versus pressure experimentally using known pressures

All of these methods were given attention, but only the experimental calibration results were used to convert measured strains into pressures. This was because the calibration results would account for possible misalignment of the strain gauges.

Calibration of the strain gauges was done by filling the system with air and recording the strain and pressure. The pressure transducer used was *Hottinger Baldwin Messtechnik absolute pressure transducer*, type P3MA, model number B14622.

6.2.3.1 Strain gauge bridge

Four strain gauges per pressure measurement were used in a somewhat unorthodox bridge arrangement – two gauges to measure the hoop strain and two to measure the axial strain. These were wired up to form a full bridge. However, due to the fact that both axial and hoop gauges will experience a positive strain when the cylinder is pressurised the gauges would have the effect of reducing the output signal. Fortunately this did not matter because the hoop strain is much larger than the axial strain and is the dominant strain. Consider the diagram shown in Figure 6.6. Strain gauges 1 and 3 are mounted to measure hoop strain, and gauges 2 and 4 are mounted to measure axial strain.

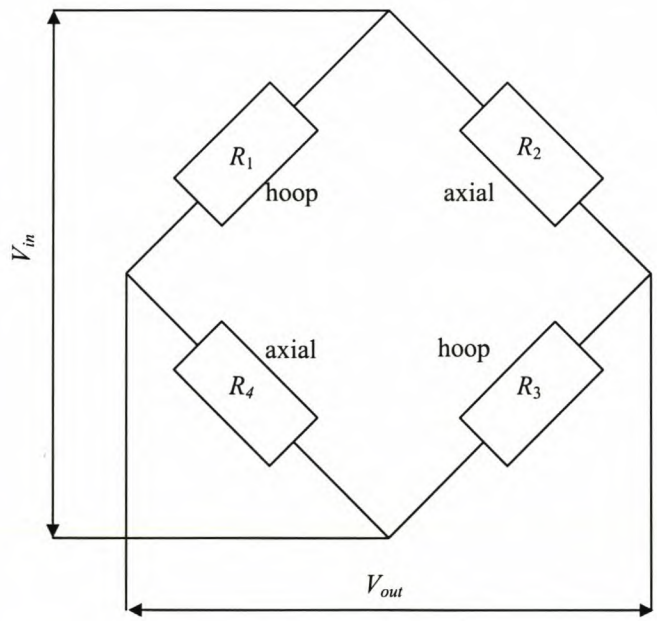

Figure 6.6 Strain gauge configuration for pressure measurement

The general equation for the output voltage V_{out} given a change in the resistances ΔR of the strain gauges is

$$\frac{V_{out}}{V_{in}} = \frac{1}{4}\left[\frac{\Delta R_1}{R_1} - \frac{\Delta R_2}{R_2} + \frac{\Delta R_3}{R_3} - \frac{\Delta R_4}{R_4}\right] \tag{6.1}$$

Substituting the basic strain gauge equation $\Delta R / R = K\varepsilon$ where K is the gauge factor (equal to 2 for the strain gauges used), the following equation is obtained:

$$\frac{V_{out}}{V_{in}} = \frac{K}{4}\left[\varepsilon_1 - \varepsilon_2 + \varepsilon_3 - \varepsilon_4\right] \tag{6.2}$$

The bridge configuration was wired up such that ϵ_1 and ϵ_3 were the hoop strains and ϵ_2 and ϵ_4 were the axial strains. If it is assumed that the strain gauges were accurately positioned, then it can be said that $\varepsilon_1 = \varepsilon_3 = \varepsilon_\theta$ and $\varepsilon_2 = \varepsilon_4 = \varepsilon_x$. Hence,

$$\frac{V_{out}}{V_{in}} = \frac{K}{2}\left[\varepsilon_\theta - \varepsilon_x\right] \tag{6.3}$$

Critically, it can be seen that the two different strains subtract from each other – resulting in weaker output voltage, poorer resolution and lower accuracy. Should the axial strain equal the hoop strain then the output will be zero, despite the fact that the cylinder is subjected to a pressure. However, in general the hoop strain is generally higher than the axial strain. The main reason for using the above mentioned configuration is that it is temperature compensated. To illustrate this point consider that the cylinder experiences strain due to both pressure and temperature. The strain experienced by the gauges will be as follows:

$$\varepsilon_1 = \varepsilon_3 = \varepsilon_\theta + \varepsilon_T \tag{6.4}$$

$$\varepsilon_2 = \varepsilon_4 = \varepsilon_x + \varepsilon_T \tag{6.5}$$

Substituting equations 6.4 and 6.5 and above into equation 6.2 yields:

$$\begin{aligned}\frac{V_{out}}{V_{in}} &= \frac{K}{4}\left[\varepsilon_\theta + \varepsilon_T - \left(\varepsilon_x + \varepsilon_T\right) + \varepsilon_\theta + \varepsilon_T - \left(\varepsilon_x + \varepsilon_T\right)\right] \\ &= \frac{K}{2}\left[\varepsilon_\theta - \varepsilon_x\right]\end{aligned} \tag{6.6}$$

Which is exactly the same result as given in equation 6.3, indicating that the output voltage will not be affected by any thermally induced strains, since thermal strains cancel each other out. Thus, accuracy and resolution has been sacrificed for the convenience of not having to be concerned with thermal strains.

6.2.4 Filtering of Temperature Data

Figure 6.7 is a graph depicting temperature versus time recorded in a stable temperature environment of approximately 17 °C. It can be seen that the data appears very erratic with variations of about 1 °C either side of the average. These temperatures were sampled using a type-T thermocouple. The channel with which the temperature was sampled was set to maximum resolution in the range of –1.749 to 2.468 mV, corresponding to a temperature range of -20 to 60 °C. The specified noise level on the card for this level is approximately 50 μV. From thermocouple calibration tables it is known that a 1 °C change in temperature corresponds to a voltage change of approximately 40 μV. The thermocouple was directly connected to the DAQ card with no pre-amplification, thus it is clear that the noise occurring in the readings is from the DAQ card, since the levels of the noise are what should to be expected when sampling in the voltage range of –1.749 to 2.468 mV. This undesirable noise effect could be alleviated by filtering the data through a low-pass filter in order to remove the high frequency noise. A number of numerical filters are available in *LabVIEW*, and a second order Butterworth low-pass filter with a cut-off frequency of 10 Hz was used to filter temperature readings. The graph in Figure 6.8 depicts the same data shown in Figure 6.7, but after it has been filtered through a second order Butterworth low-pass filter with a cut-off frequency of 10 Hz.

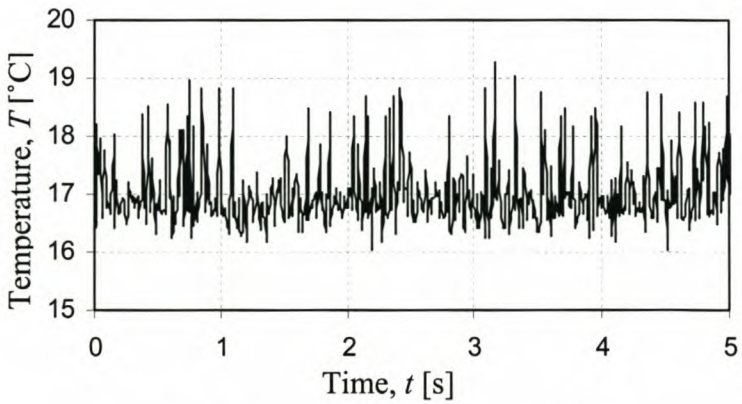

Figure 6.7 Temperature data - unfiltered

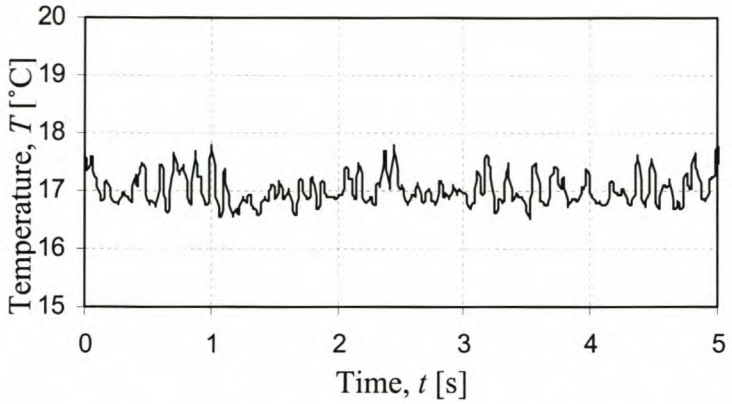

Figure 6.8 Temperature data – filtered

6.2.5 Filtering of Strain Data

Figure 6.10 depicts the thrust (measured by the strain gauges) against time while no forces were applied to the cantilevered measurement structure. It can be seen that despite that fact that the structure was totally isolated and no external or internal forces were applied to it, the thrust value does not remain constant but fluctuates between a minimum and maximum. It can be seen that the amplitude of the strain is approximately 0.02 N. From the calibration equation used, a thrust of 0.02 N corresponds to a voltage of approximately 40 mV. The voltage range of the sampling channel was from –10 to 10 V. In this range, the amplitude of the noise to be expected from the DAQ card is approximately 10 mV, which corresponds to a thrust of approximately 0.005 N. Since the amplitude of the measured noise (40 mV) is 4 times higher than the DAQ card noise (10 mV), not all of the noise can be attributed to the DAQ card, and there must also be another reason for the noise. In this case it is suspected that the bridge amplifier is responsible for providing the noise in the signal. As was the case with temperature, the problem of high frequency noise could be alleviated (to a certain extent) by filtering the data. Figure 6.10 presents the data of Figure 6.9 after being filtered using a second order Butterworth low-pass filter, with a cut-off frequency of 12 Hz.

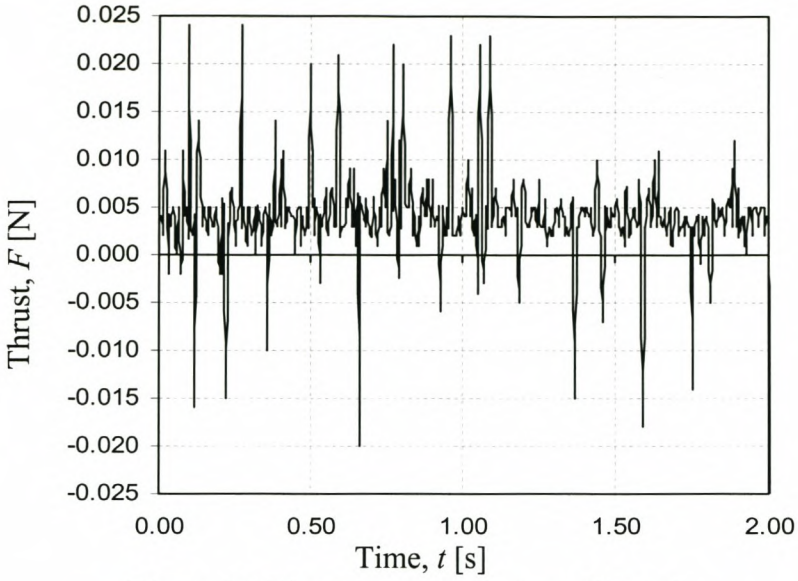

Figure 6.9 Thrust measurement - unfiltered

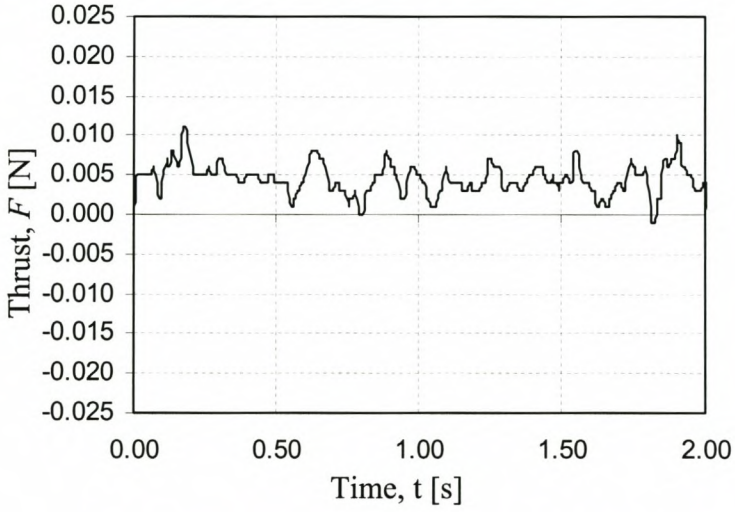

Figure 6.10 Thrust measurement - filtered

6.3 Calibration Experiments

6.3.1 Effect of Valve Operations

The solenoid valves used functioned by activating a spring mechanism that would allow fluid to flow through the valve creating an impulse. It was necessary to observe what effect these valves added to the higher than expected noise levels. An experiment was conducted in which the nozzle solenoid valve was opened and closed with no propellant inside the system. The output voltages from the thrust strain gauge and from the pressure strain gauge on the accumulator were sampled and plotted on a graph against time.

6.3.1.1 Effect on thrust strain

It is expected that the nozzle solenoid valve would have an effect on the thrust measurement strain gauges, due to the fact that the set-up had been designed to allow these strain gauges to pick up strain for very small thrust impulses. This was indeed the case as can be seen in Figure 6.11 in which the strain is plotted against time. The first large spike is the valve opening. The second large spike is the valve closing. It can be seen that the second spike is somewhat larger that the first one. In both cases the spikes are followed by oscillating behaviour, similar to the damped free vibration response discussed in section 5.2. The period of these vibrations was the same as that determined experimentally in section 5.2.3.

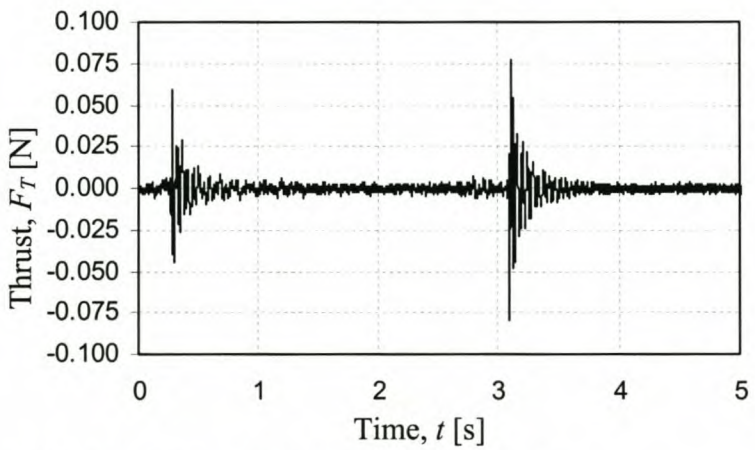

Figure 6.11 Effect of opening and closing of valve

The strain gauges mounted to measure pressure in the accumulator volume experienced no changes at all due to the opening of the thrust valve. This indicates that the Perspex tubing was very rigidly cantilevered as no bending moments were carried through the PVC block used to cantilever the tube. The PVC block would also have provided isolation from impulse effects in the cantilevered tube.

6.3.1.2 Effect of storage tank valve

The storage tank valve had no effect on any of the strain gauge bridges. This was due to the fact that this valve was relatively far away from any of the strain gauge bridges. In addition the PVC blocks used as supports of the perspex tubing provided good isolation from any impulse effects from the feed valve.

6.3.2 Pressure Calibration

The two graphs shown in Figure 6.12 depict the pressure calibration graphs for the accumulator and storage tank. The graphs were obtained by continuously sampling the output voltage V from the strain gauge bridges (described in section 6.2.3) while at the same time recording the absolute pressure in the system using a pressure transducer. The graphs depict pressure versus voltage and a straight line was fitted through each of the data sets to give the calibration equations 6.7 and 6.8 (units are V for voltage and kPa for pressure). The R^2 values are the coefficients of determination, an indicator ranging from 0 to 1 that reveals how closely a fitted curve corresponds to the actual data. A fitted curve is most reliable when R^2 is at or near 1.

Accumulator:

$$p = 191.409 \times V + 9.696 \tag{6.7}$$

$$R^2 = 1.00$$

Storage Tank:

$$p = 193.174 \times V + 9.443 \tag{6.8}$$

$$R^2 = 1.00$$

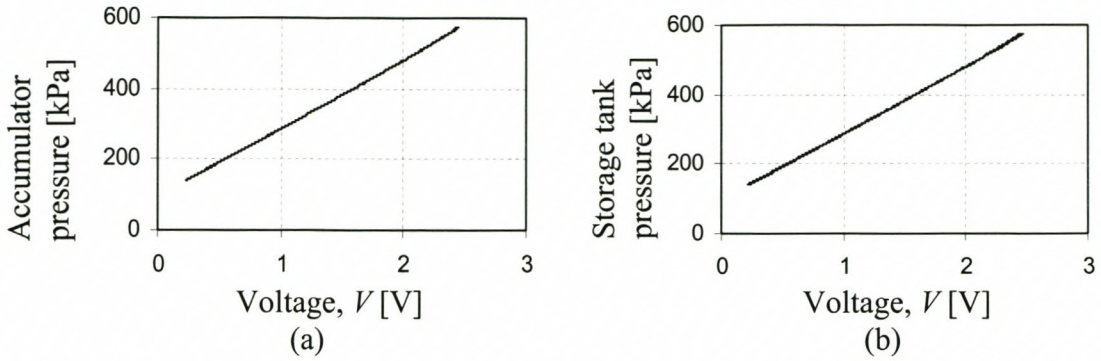

Figure 6.12 Pressure calibration graphs for accumulator (a) and storage tank (b)

7 RESULTS AND OBSERVATIONS

The observations and results obtained from the theoretical and experimental work are presented in this section. Theoretical results for air and butane are given, followed by experimental results for air and butane.

7.1 Air – Theoretical

Theoretical results for air were obtained using the program *AirSim.exe*. The mathematical modelling used in this program is discussed in section 4.3. A base case is defined and the resulting thrust and pressure graphs are shown in section 7.1.1. The effect of varying system parameters is presented in section 7.1.2.

7.1.1 Base Case Thrust Curve

Figure 7.1 depicts a thrust curve for air for the thruster model shown in Figure 4.5. The parameters used in generating this simulation are listed in Table 7.1, and are intended to serve as a base case set of values.

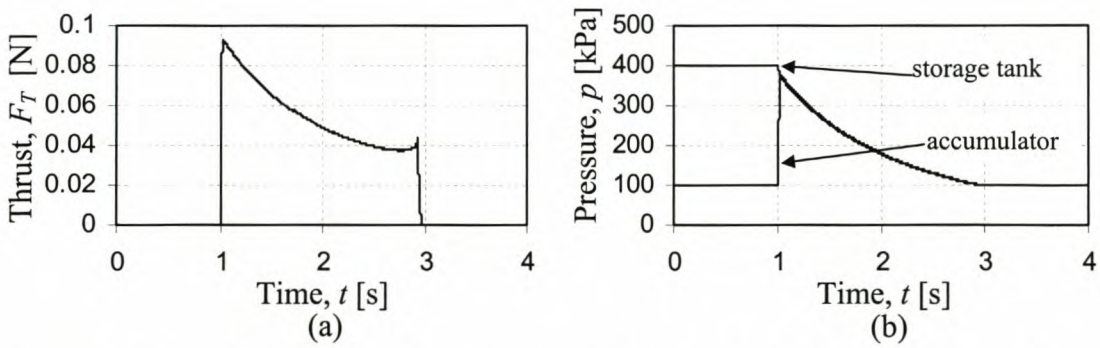

Figure 7.1 Theoretical thrust (a) and pressure (b) curves for base case air simulation

Table 7.1 Parameters for base case air simulation

Parameter	Value	Units
Starting pressure	400	kPa
Starting temperature	288	K
Back pressure	100	kPa
Nozzle throat diameter	1	mm

Nozzle exit diameter	5	mm
Solenoid valve orifice diameter	2.8	mm
Storage tank volume	251.3×10^{-6}	m^3
Accumulator volume	31.4×10^{-6}	m^3

7.1.2 Parameter Sensitivity Analyses

Simulations were run using *AirSim.exe* in order to investigate the effect of changes in various parameters on the thrust produced. Figure 7.2 to Figure 7.5 depict peak thrust produced as a function of one of the system parameters. In other words all the parameters of the base case presented in Table 7.1 were held constant while one of the parameters was varied, and the peak thrust was noted.

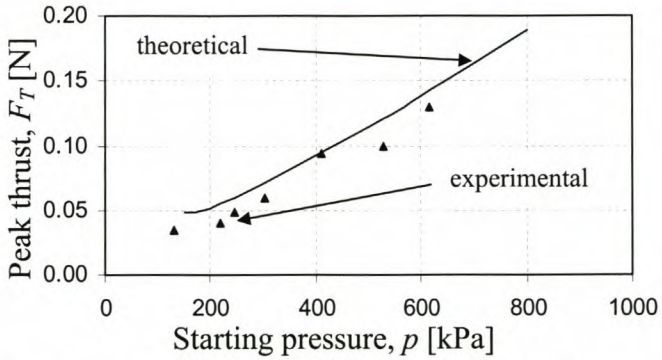

Figure 7.2 Theoretical and experimental peak thrust as a function of starting pressure for air

Figure 7.2 depicts the peak thrust produced against the initial pressure in the storage tank. The behaviour appears linear in nature, which is to be expected when considering that the equation describing the choked mass flow rate, equation 3.19, is linear in terms of initial pressure. The experimental data is fairly close to the theoretical data. However, in general the theory tends to overestimate the thrust by a constant offset of approximately +15 %.

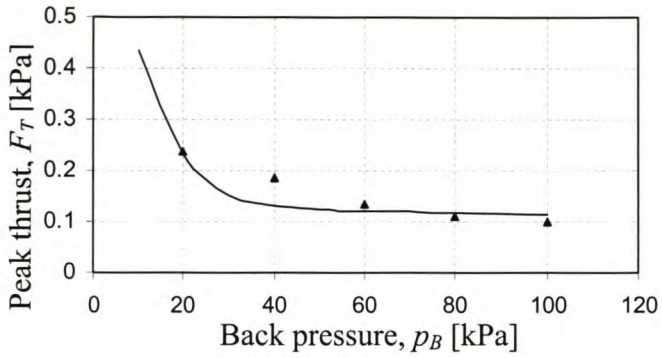

Figure 7.3 Theoretical and experimental peak thrust as a function of back pressure for air

Figure 7.3 indicates the effect of back pressure on peak thrust. For these curves the starting pressure used was 500 kPa. It can be seen from both the theoretical and experimental data that the relationship is not linear. However, the non-linearity is indicated to a greater extend by the theoretical data. The reason for the sudden increases in peak thrusts at lower back pressures is due to the fact that the lower the back pressure the closer the flow can get to being shock-free throughout the nozzle.

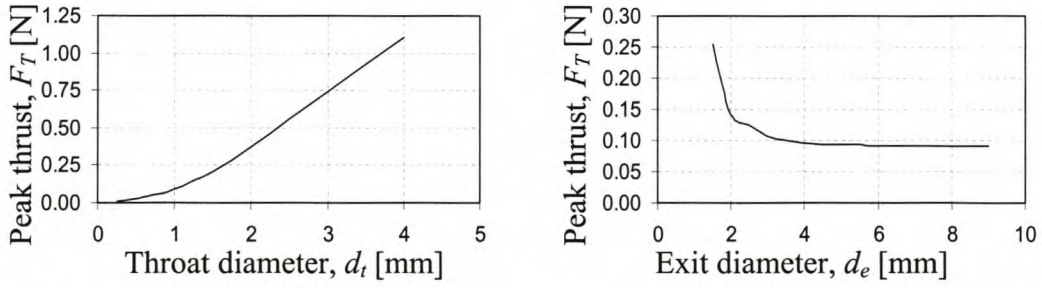

Figure 7.4 Theoretical effect of throat (a) and exit (b) diameters on peak thrust for air

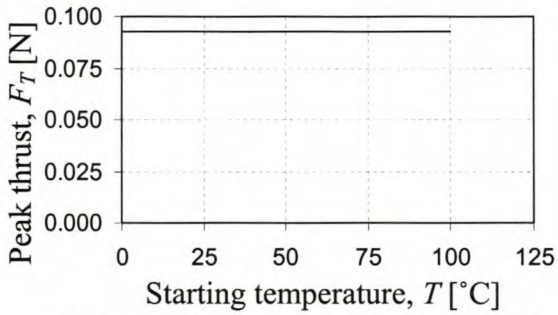

Figure 7.5 Theoretical peak thrust as a function of starting temperature for air

It can be seen that varying the starting temperature between 0 and 100 °C has no effect on the peak thrust. This can be accounted for by considering the low specific

heat C_p of air which is 1005 J/kg.K. The change in internal energy is given by the relation $u = C_p (T - T_{ref})$. Hence, a low value of C_p would result in a low increase in internal energy. Comparison of the graphs in Figure 7.2 and Figure 7.5 indicates that the effect initial temperature has on peak thrust is insignificant when compared to the effect of initial pressure when air is used as propellant.

7.2 Butane – Theoretical

Theoretical results for a thruster system using butane as propellant are presented in this section. Most results were obtained using the program *ButaneSim_B.exe* which employed idealised gas dynamic theory to analyse the flow through the nozzle. A base case is defined and resulting thrust and pressure graphs are shown in section 7.2.1. The effects of varying certain system parameters is presented in section 7.2.2.

7.2.1 Base Case Thrust Curve

Figure 7.6 depicts a thrust curve for butane for the model shown in Figure 6.1. The base case values are listed in Table 7.2. For this simulation the storage tank valve, in Figure 6.1, was held open and the nozzle valve was opened for two seconds.

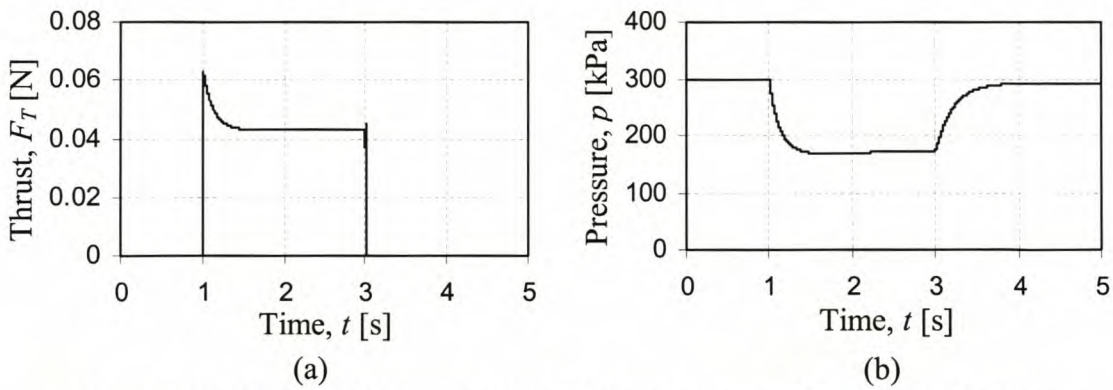

Figure 7.6 Theoretical base case thrust (a) and pressure (b) curve for butane

The thrust curve in Figure 7.6(a) depicts a sudden rise in the thrust to a peak of approximately 0.06 N, followed by a tapering off to a steady thrust of 0.043 N which is maintained for the duration of the firing. This constant level of thrust will be referred to as the *steady thrust*, and will be used as the dependant parameter in some of the parameter sensitivity analyses presented in section 7.2.2. This should be distinguished from the *peak thrust* which is also used in some of the parameter

sensitivity analyses. It can be seen that the pressure curve in Figure 7.6 (b) follows a similar trend to the corresponding thrust curve. There is an initial drop in the pressure following the opening of the valve which is followed by a period of constant pressure. After closing of the nozzle solenoid valve the pressure increases again to the initial pressure level, i.e. pressure is regained after a firing. This is in contrast to the air simulations where the pressure dropped continuously (as it should) during firing. [The pressure behaviour is verified experimentally in section 7.4 and can be seen in (amongst others) the following graphs: Figure 7.13(b), Figure 7.14(b) and Figure 7.15(b).]

Table 7.2 Parameters for base case butane simulation

Parameter	Value	Units
Starting pressure	300	kPa
Starting temperature	305	K
Back pressure	100	kPa
Nozzle throat diameter	1	mm
Nozzle exit diameter	5	mm
Solenoid valve equivalent lengths	100	mm
Storage valve orifice diameter	2.8	mm
Nozzle valve orifice diameter	1.6	mm
Storage tank volume	251.3×10^{-6}	mm
Accumulator volume	31.4×10^{-6}	mm
Valve chamber	2.36×10^{-6}	mm
Ideal gas constant	138	J/kg·K

7.2.2 Parameter Sensitivity Analyses

Simulations were run using *ButaneSim_A.exe* and *ButaneSim_B.exe* in order to investigate the effect of changes in various parameters on the thrust produced – i.e. all the parameters of the base case given in Table 7.2 were held constant while one of the parameters was varied.

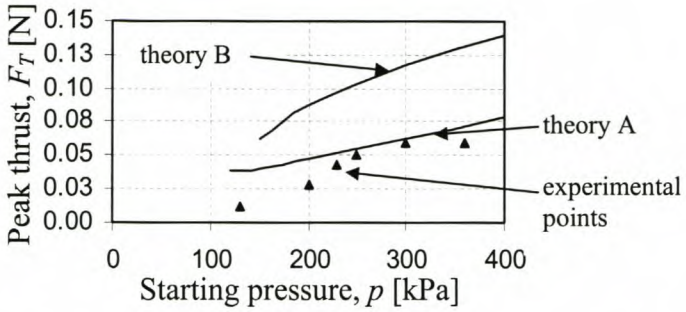

Figure 7.7 Theoretical and experimental peak thrust as a function of starting pressure for butane

Figure 7.7 shows the peak thrust as a function of the initial pressure in the storage tank and accumulator. Theoretical results using both theory A (*ButaneSim_A.exe* - using fundamental equations directly) and theory B (*ButaneSim_B.exe* - using ideal gas theory) are given. It can be seen that the ideal gas theory actually matches the experimental data better than the theory developed from the fundamental equations directly.

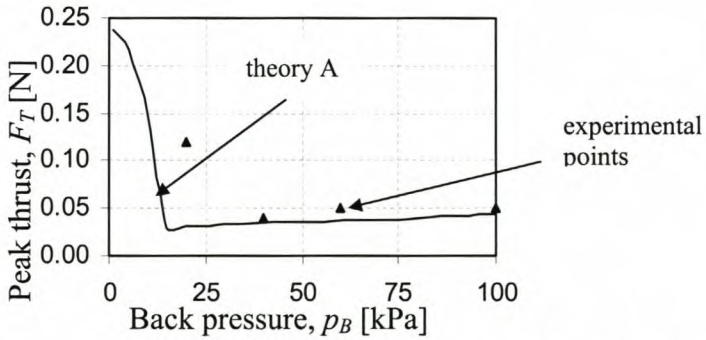

Figure 7.8 Theoretical and experimental peak thrust as a function of back pressure for butane

The theoretical and experimental effect of back pressure on peak thrust is depicted in Figure 7.8. It can be seen that the peak thrust actually decreases slightly with a decrease in back pressure (whereas in Figure 7.3 the peak thrust increased slightly with an decrease in back pressure). Below a back pressure of approximately 15 kPa the peak thrust suddenly increased dramatically [similar to that shown in Figure 7.3]. The sudden increase in peak thrust for back pressures can be attributed to an absence of shocks in the nozzle (to be discussed in section 8).

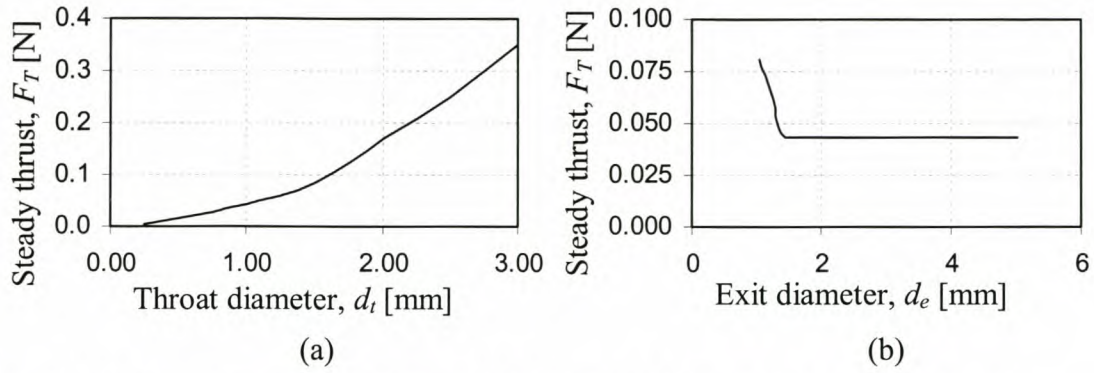

Figure 7.9 Theoretical effect of throat (a) and exit (b) diameters on steady thrust

Effects due to nozzle variations can be seen in Figure 7.9 where steady thrust as a function of throat diameter (a) and exit diameter (b) is depicted. It is seen that there is a non-linear increase in thrust with an increase in throat diameter in Figure 7.9(a). This can be attributed to the fact that a bigger nozzle allows for a larger mass flow rate and thus a bigger thrust (refer equation 3.4). From Figure 7.9(b) it is seen that the thrust is insensitive to increases in the exit diameter above about 2 mm. However, there is a dramatic increase in thrust for decreases in exit diameter less than about 1.5 mm – i.e. for nozzles with an exit diameter just slightly larger than the throat diameter of 1 mm.

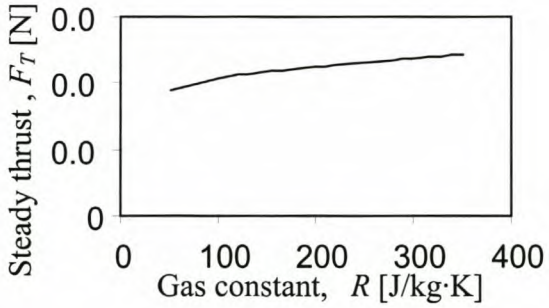

Figure 7.10 Theoretical effect of ideal gas constant on peak thrust

Variations in steady thrust resulting from using different values for gas constant R are shown in Figure 7.10, where R is varied over a wide range (50 to 350 J/kg·K), resulting in a total increase of 20 % in steady thrust. While the gas constant was varied, the specific heat ratio was held constant but the specific heats were still calculated as a function of temperature and pressure using the equations and method described in Appendix A. The choice of R for butane used for other simulations was

138 J/kg·K. This choice is discussed in appendix A, where the variations of R for the range worked in was from 125 to 143 J/kg·K. Thus, from the results shown in Figure 7.10, the variation in the steady thrust resulting from uncertainties in the precise value of R would be relatively small.

7.3 Air – Experimental

Experimental data for an experiment using air at an initial pressure of 410 kPa exhausting to a 100 kPa back pressure is presented in Figure 7.11. The solenoid valve was opened at time 1 s, held open for 2 s and closed at time 3 s. It can be seen in Figure 7.11(b) that after two seconds the pressures in both the storage tank and accumulator were down to 100 kPa (the environmental back pressure that the thruster exhausted to in this case), i.e. the propellant was effectively depleted. The shape of the thrust curve is very similar to that of the accumulator pressure curve. The peak thrust is quickly reached after opening the valve (approximately 0.02 s). After this the thrust drops off rapidly as the pressure in the accumulator drops. The results for a test exhausting to a back pressure of 20 kPa is shown in Figure 7.12. The general behaviour of thrust and pressure is very similar for the results of the test conducted at 100 kPa back pressure shown in Figure 7.11. However, the thrust values are much higher and a peak thrust of over 0.2 N was achieved.

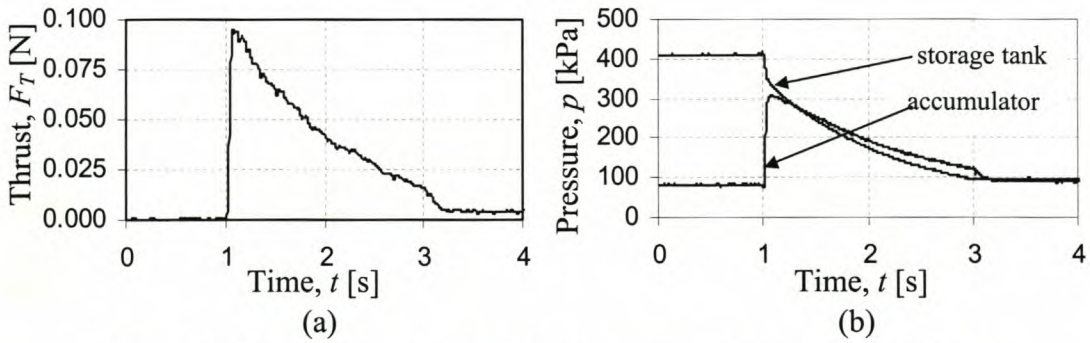

Figure 7.11 Experimental thrust (a) and pressure (b) against time for air

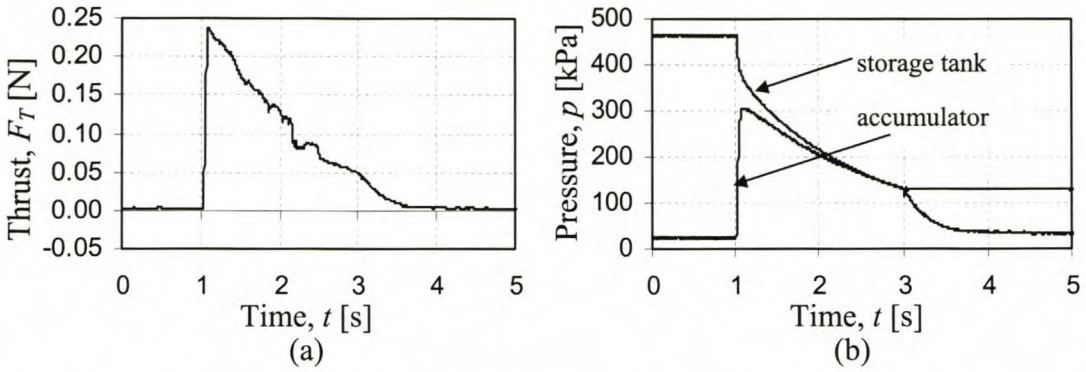

Figure 7.12 Experimental thrust (a) and pressure (b) for air in vacuum (20 kPa) test

7.4 Butane – Experimental

Experimental data for butane exhausting to a 100 kPa back pressure is depicted in Figure 7.13 and Figure 7.14. Refer to Figure 6.1 for a schematic diagram of the experimental model. The physical properties of the experimental model are the base case values listed in Table 7.1. The data in Figure 7.13 was obtained by removing the nozzle valve and operating the storage tank valve, whereas the data in Figure 7.14 was obtained by keeping the storage tank valve open and operating the nozzle valve. Storage tank valve refers to the solenoid valve between the storage tank and the accumulator. Nozzle valve refers to the solenoid valve between the accumulator and nozzle, as shown in Figure 6.1.

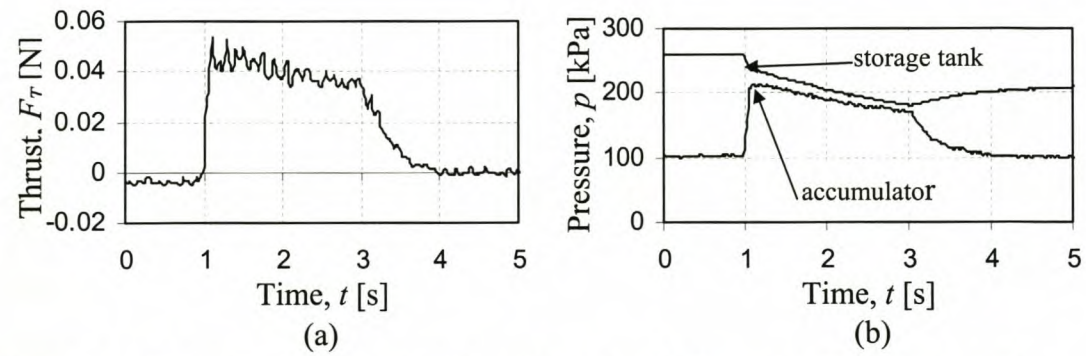

Figure 7.13 Thrust (a) and pressure (b) against time for butane using storage tank valve

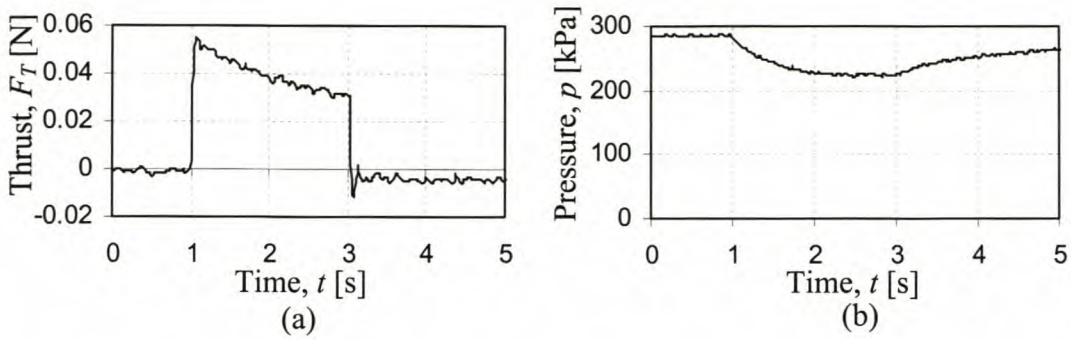

Figure 7.14 Thrust (a) and pressure (b) against time for butane with the storage tank valve held open as the nozzle valve is opened and closed

It can be seen from Figure 7.13(a) and Figure 7.14(a) that whilst similar levels of thrust are obtained, the shape of the thrust curves is different. The solenoid valves operated to generate the thrusts (i.e. the storage tank valve for Figure 7.13, and the nozzle valve for Figure 7.14) were both opened at time 1 s and closed at time 3 s. The thrust curves in Figure 7.14(a) are much steeper at these times (especially when the valves were closed). In Figure 7.13(a) there was thrust for about 0.5 s after the valve was closed. This is due to the fact that there was some liquid in the accumulator control volume and even after the valve was closed the liquid continued to evaporate providing a supply of gas at a higher pressure than the back pressure.

It is also interesting to compare the pressure graphs (Figure 7.13(b) and Figure 7.14(b)). Figure 7.13(b) is similar to the pressure graph shown in Figure 7.11(b), since in both cases the nozzle valve was removed and the storage tank valve was opened and closed. As was the case in Figure 7.11, the shape of the thrust curve in Figure 7.13(a) is very similar to the shape of the accumulator pressure curve in Figure 7.13(b). However, the most important difference between the pressure curves for butane, Figure 7.13(b) and Figure 7.14(b), and the pressure curve for air, Figure 7.11(b) is that the butane pressure recovers after it has dropped due to a firing of the thruster. This is due to the fact that when the butane pressure drops, the temperature of the liquid butane remaining is higher that the saturation temperature at the new pressure. Hence, liquid butane boils off, causing the pressure to increase until it reaches the saturation pressure corresponding to the temperature of the system. This is what Zakirov et al. (2001) refer to as the *self-pressurising effect* of liquefied-gas systems.

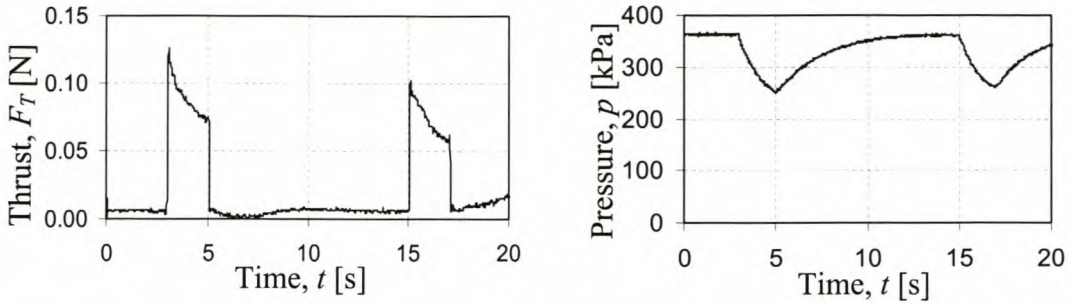

(a) (b)

Figure 7.15 Vacuum chamber testing (20 kPa) for butane using nozzle valve

Figure 7.15 presents the thrust and pressure curves for two consecutive butane firings in a vacuum environment (back pressure of 20 kPa absolute). Although the initial pressure in the system for these firings is about 20 % higher than that in Figure 7.14(b), the difference between the peak thrust for the vacuum testing is almost double for the test conducted in a 20 kPa environment. It can be seen from Figure 7.14(b) that the pressure appears to recover almost all of its original value during the ten second interval between the two pulses. However, the peak thrust for the second pulse is somewhat lower that that of the first pulse.

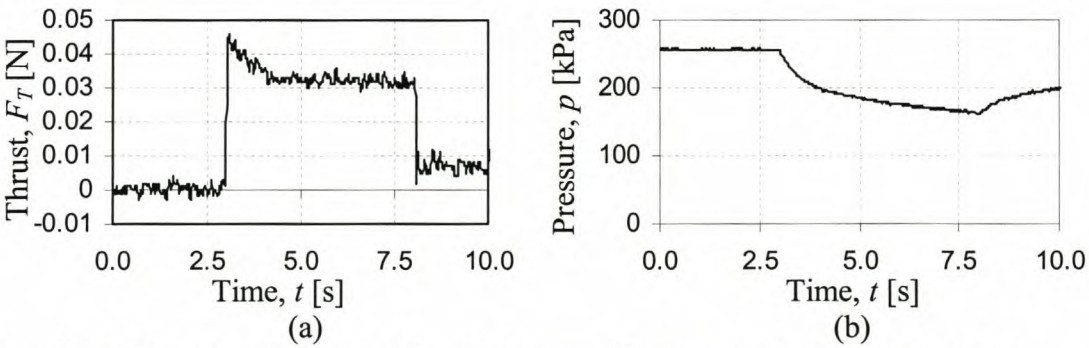

(a) (b)

Figure 7.16 Experimental thrust (a) and pressure (b) curve for butane for 5 s pulse using nozzle valve

The specific impulse of the butane in the system was estimated experimentally by conducting a test generating a 5 s pulsed thrust shown in Figure 7.16. The difference in mass of the liquid butane before and after the pulse was estimated, by observing the drop in the level of the liquid, to be 0.43 grams. The adjusted equation for specific impulse (equation 3.12) was given as

$$I_{sp} = \frac{\overline{F}_T}{\frac{\Delta m}{\Delta t} g} = \frac{\left(\int F_T dt \right) / \Delta t}{\frac{\Delta m}{\Delta t} g} \tag{7.1}$$

Using equation 7.1 the specific impulse is determined:

$$I_{sp} = \frac{0.03}{\frac{430 \times 10^{-6}}{5} 9.81} = 36 \text{ s}$$

The specific impulse I_{sp} as calculated using equation 7.1 gives a relative measure of how well the energy in the butane is being converted into thrust. The experimental value reported by Gibbon and Underwood (2001) was 43 s, about 20 % higher than the value of 36 determined for the curve in Figure 7.16.

In order to generate a correlation between initial pressure and duration of thrust, data from a number of experiments was used to generate a function describing the average thrust as a function of starting pressure and duration of thrust. The data from the experiments is given in Table G.1 in appendix G. It is important to note that for this purpose the thrust value used was the *average thrust*, defined as follows:

$$\overline{F}_T = \frac{\int F_T dt}{\Delta t} \tag{7.2}$$

Three typical experimental data sets used in generating the correlation are given and discussed in Figure 7.17, Figure 7.18 and Figure 7.19.

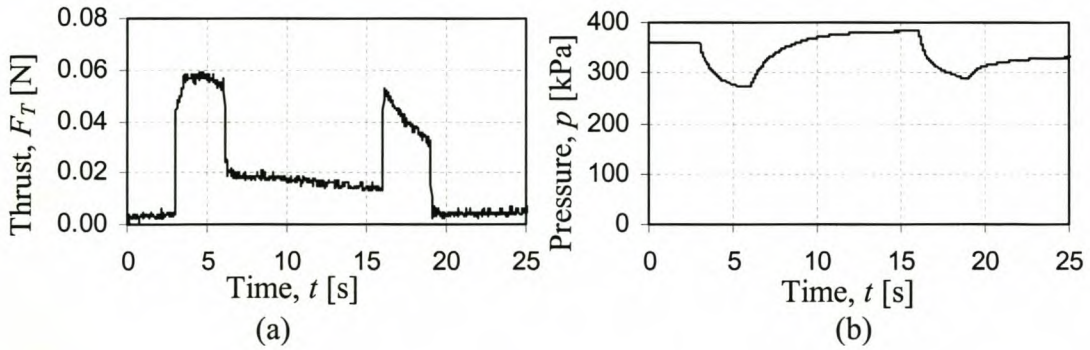

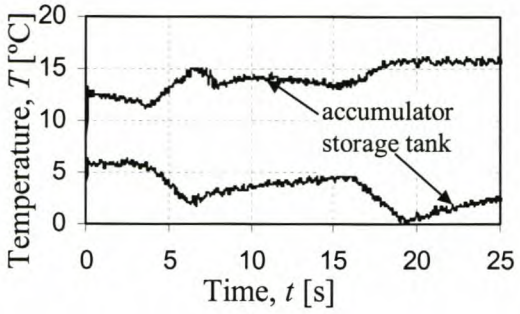

(c)

Figure 7.17 Experimental thrust (a), pressure (b) and temperature (c) for butane for two pulses of three pulses using nozzle valve

The results presented in Figure 7.17 are for an experiment in which the accumulator heater was used to increase the pressure and temperature of the butane vapour. It can be seen that in Figure 7.17(b) that a starting pressure of almost 400 kPa was obtained. It is interesting to examine the temperatures in Figure 7.17(c). The thermocouple in the storage tank measured the liquid temperature. It can be seen the storage tank temperature behaviour is similar to the pressure behaviour shown in Figure 7.17(b), i.e. when there was a pressure drop the temperature of the liquid dropped to the saturation temperature at the lower pressure. Similarly when there was a pressure recovery the temperature of the liquid increased slightly. In the accumulator the temperature increases when the valve is opened. This can be explained by considering the experimental layout of the model that is shown in Figure 6.1. It can be seen that the accumulator heater is some distance away (approximately 0.25 m) from the accumulator thermocouple. Thus, only when the valve is opened does the thermocouple register the increase in temperature due to the hot vapour flowing over it.

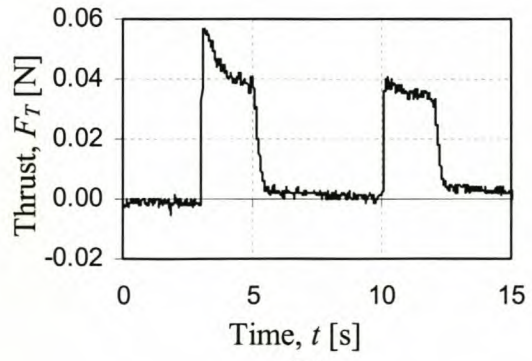

(a)

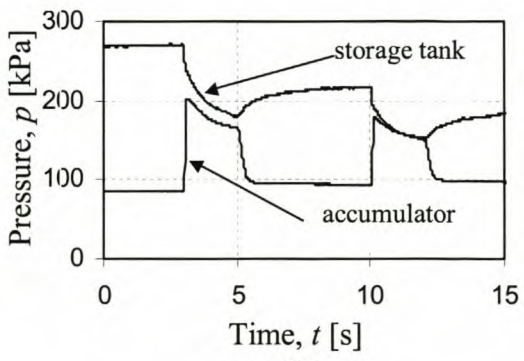

(b)

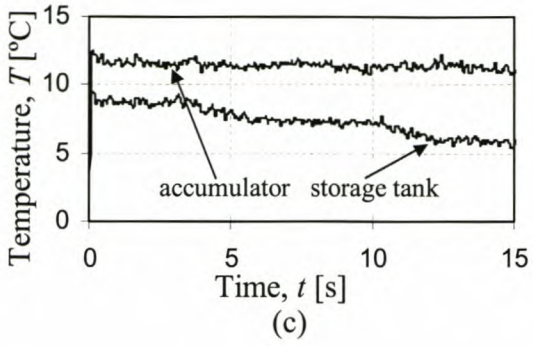

Figure 7.18 Experimental thrust (a), pressure (b) and temperature (c) for butane for two pulses of two seconds using storage tank valve

Results for two pulses of two seconds using the storage tank valve are shown in Figure 7.18. The first pulse in the thrust graph in Figure 7.18(a) bears a resemblance to the theoretical base case thrust curve shown in Figure 7.6(a). The thrust decreases more steeply initially (for the first 0.6 s in Figure 7.18(a) and for the first 0.3 s in Figure 7.6(a)) than for the remainder of the thrust duration. To a lesser extent the second thrust pulse also exhibits this trend. Examination of the temperature graph of Figure 7.18(b) indicates a drop in temperature of the liquid in the storage tank accompanying the pressure drops during firing. However, the accumulator temperature remains constant.

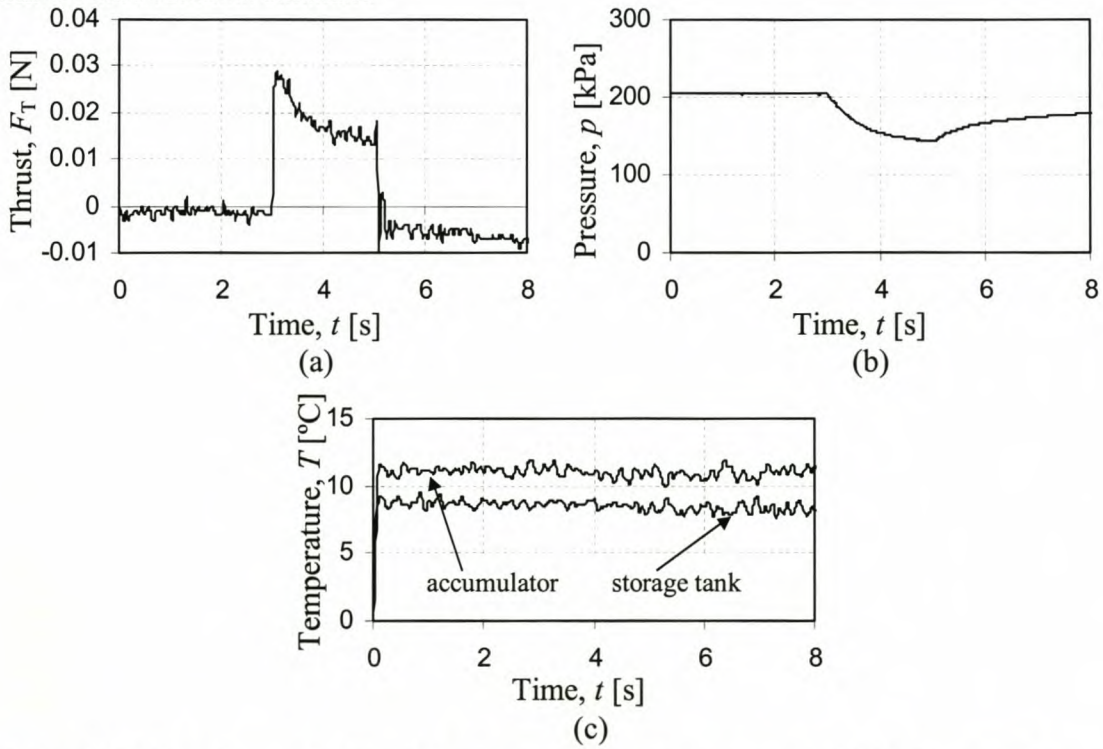

Figure 7.19 Experimental thrust (a), pressure (b) and temperature (c) for butane for a 2 s pulse using nozzle valve

Experimental data from a single two second firing using the nozzle valve is given in Figure 7.19. The thrust curve in Figure 7.19(a) depicts the tendency discussed in the previous paragraph and in section 7.1.1 in which the thrust decreases rapidly after the initial peak followed by a more gradual decrease in the thrust. A similar trend is observed in the pressure curve of Figure 7.19(b) where the self-pressurising effect can also be seen. The temperature data in Figure 7.19(c) suggests that the level of liquid in the storage tank had fallen to a level below that of the thermocouple, resulting in the thermocouple measuring the vapour temperature, since no significant drop in temperature is evident in the storage tank during firing.

The data in appendix G is used to develop a correlation for the experimental data describing the average thrust $\overline{F_T}$ as a function of the pulse duration Δt and the initial pressure p. It was assumed that the expression correlating average thrust in terms of pulse duration and pressure could be given as:

$$y = a\, x_1^b x_2^c \tag{7.3}$$

where y is the dependant variable (average thrust) which is a function of two independent variables x_1 and x_2 (pulse duration and initial pressure), and a, b and c are the constants. These constants are determined by performing a multi-linear regression analysis. The coefficient of determination R^2 indicating the accuracy of the fit was also calculated. The values for a, b, c and R^2 are given in Table 7.3. Examination of this table reveals that the value of b is much smaller than that of c (about 200 times) and is very close to zero. Hence, it is clear that x_2 (initial pressure) is the dominant variable in the correlation. In order to verify this, two further multi-linear regression analyses were performed assuming average thrust to be a function of pulse duration only ($c = 0$) and of initial pressure alone ($b = 0$). These results can also be found in Table 7.3. It can be seen that a low R^2 value of 0.14165 was obtained when average thrust is correlated as a function of pulse duration only – indicating a poor correlation. However, the results for the correlation using initial pressure as the only independent variable are very similar to that obtained using two independent variables. Hence, the following equation can be used to predict average thrust $\overline{F_T}$ in N as a function of the initial pressure p in kPa:

$$\overline{F}_T = 13.706 \times 10^{-6}\, p^{1.36229} \tag{7.4}$$

Table 7.3 Values for correlation as function of pulse duration and initial pressure

$\overline{F}_T = a\, t^b\, p^c$			
a	b	c	R^2
12.870×10^{-6}	0.007027	1.37199	0.56364
$\overline{F}_T = a\, t^b\, p^0$			
a	b	c	R^2
0.03525	-0.25313	0	0.14165
$\overline{F}_T = a\, t^0\, p^c$			
a	b	c	R^2
13.706×10^{-6}	0	1.36229	0.56356

Using the correlation given in equation 7.4 Figure 7.20 and Figure 7.21 are plotted to present graphically the accuracy with which equation 7.4 correlates the experimental data from which it was obtained. In Figure 7.20 it can be seen that the correlation appears to work reasonably well. There is one stray experimental data point for a 0.06 N average thrust. However, this was for the highest experimental average thrust used and is thus at the limit of the range. The comparison between the experimental data and the correlation against initial pressure shown in Figure 7.21 indicates a fair amount of scattering of the experimental data points about the correlation curve.

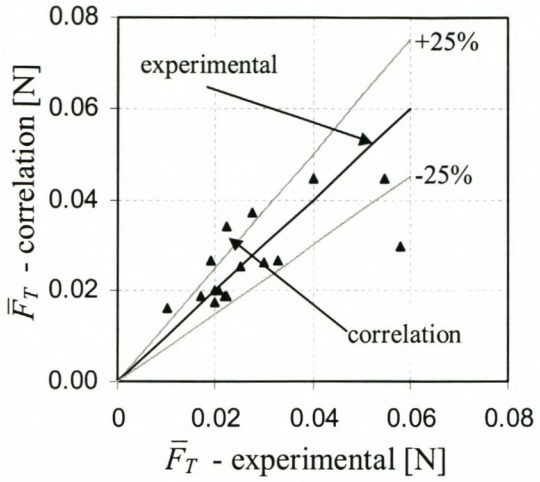

Figure 7.20 Graphical comparison between experimental data and correlation equation 7.4

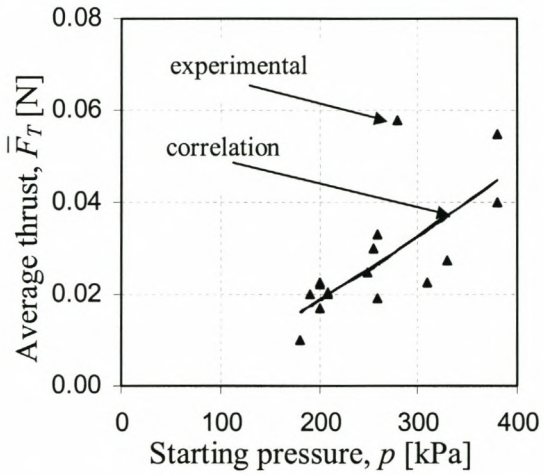

Figure 7.21 Experimental and correlated average thrust against starting pressure

8 DISCUSSIONS AND CONCLUSIONS

The outcomes of the project are discussed in this section and where possible conclusions are drawn. Whilst most of the focus is on the results obtained (section 7), some attention to other aspects is also given.

8.1 Thermo-fluid Modelling of the System

Detailed theoretical modelling of the system was given in section 4.4 and the results in section 7. Numerical simulation is important in the initial development of the thruster system because the capability to model the functioning of such a thruster system mathematically in order to predict the expected thrust delivered by the system is an extremely useful resource to have access to. Numerical simulation models allow the designer to observe the influence of design parameters without having to resort to physical model building and testing.

The three computer simulation programs (*AirSim.exe, ButaneSim_A.exe* and *ButaneSim_B.exe*) developed, all modelled the system as being one-dimensional and at most four control volumes were used. While these programs provided reasonable results with regards to the thrust, they did tend to over-predict the thrusts. In addition the butane program required an awkward assumption, namely that of non-thermodynamic equilibrium (section 3.3.2) between the liquid and vapour butane in the storage tank.

The equation used in modelling the mass transfer between liquid and vapour in the storage tank (equation 3.35) was also problematic in that in it required knowledge of the accommodation coefficient σ whose value is a source of concern, even for a common fluid such as water.

Another inaccuracy in the computer programs developed is that (with the exception of the nozzle) the momentum equation is not used as a governing equation. Although omitting the momentum equation could be viewed as acceptable in view of the fact that the velocities between the control volumes are low, it would nevertheless be

desirable to include it in a mathematical model as it would make the mathematical model more realistic.

8.2 Nozzle Geometry and Shock Waves

In the equation for thrust (equation 3.4), the dominating term is the momentum flux term $\dot{m}_e V_e$ which is generally much larger than the $A_e(p_e - p_B)$term. Since, the mass flow rate at the exit is limited due to choking when sonic flow is achieved in the throat (refer to equation 3.23), proper nozzle design is required to ensure a maximum value of V_e. The problem experienced in testing was that the nozzle design (i.e. exit to throat ratio) was inappropriate for the back pressures exhausted to since the nozzle design required a lower back pressure than what was being exhausted to. This resulted in the formation of shockwaves in the diverging portion of the nozzle.

Initially it was believed that it would be possible to achieve an absolute pressure of less than 1 kPa in the vacuum chamber. However, it was found out that the lowest pressure that could be achieved was about 20 kPa. The vacuum pump used to evacuate air from the vacuum chamber was a Genevac single stage vacuum pump, type G.R.S. 12, serial number 5291230. The specified displacement is 336 litres per minute.

The nozzle used for experimental testing had a throat diameter of 1 mm and an exit diameter of 5 mm. For a starting pressure of 500 kPa, the maximum back pressure that could be exhausted into, without the formation of normal shocks within the nozzle, using this nozzle would be about 27 kPa. This scenario was carried out experimentally (for a slightly lower back pressure of 20 kPa) and good correlation between theory and experiment was obtained using air – refer to Figure 7.3. However, for maximum exit velocity the back pressure should be equal or less to the design pressure (refer to section 3.2), in this case about 1 kPa.

It can be seen in Figure 7.4 that reducing the nozzle exit to throat ratio (i.e. by increasing the throat diameter as in Figure 7.4(a), or by reducing the exit diameter as in Figure 7.4(b), increases the thrust when exhausting to a back pressure of 100 kPa.

This is due to the fact that a lower exit to throat ratio does not require as low a back pressure to achieve supersonic shock-free flow in the diverging portion of the nozzle.

It is also interesting to note the effect of nozzle geometry on impulse per unit mass – i.e. how much impulse can be attained from one kilogram of propellant. This was investigated theoretically for butane for two second pulses using *ButaneSim_A.exe* and the base case set of values given in Table 7.2. The throat diameter d_t was varied from 0.25 to 3 mm. The impulse per unit mass may be calculated as follows:

$$I = \frac{\int_0^t F_T \, dt}{\int_0^t \dot{m} \, dt} \quad \text{N·s/kg} \tag{8.1}$$

Results using equation 8.1 were obtained for exhausting to a back pressure of 100 kPa Figure 8.1(a) and 100 Pa Figure 8.1(b). It can be seen in Figure 8.1(a) that when exhausting to a back pressure of 100 kPa, impulse per unit mass remains fairly constant below a throat diameter of about 1 mm, increases to a peak at about a throat diameter of about 1.5 mm and then drops with subsequent increases in throat diameter. However, when exhausting to a very low back pressure of 100 Pa as shown in Figure 8.1(b) the behaviour observed is very much different. For this back pressure the flow through the nozzle is shock free and hence thrust levels are much higher. Since the mass flow rates are limited to the choked value the resulting values of impulse per unit mass are also much higher (almost 6 times higher for a throat diameter of 1 mm). At small throat diameters the exit to throat area ratio is higher since the exit diameters are held constant. Hence, the exit velocities are higher since the flow is shock-free through the nozzle. The corresponding reduction in mass flow rate results in a higher impulse per unit mass. The difference between the results in Figure 8.1(a) and Figure 8.1(b) serve to stress the importance of the effect of the back pressure to which the thruster exhausts. For space environments it is important to have a large exit to throat area ratio in order to obtain as much impulse as possible per unit mass of propellant.

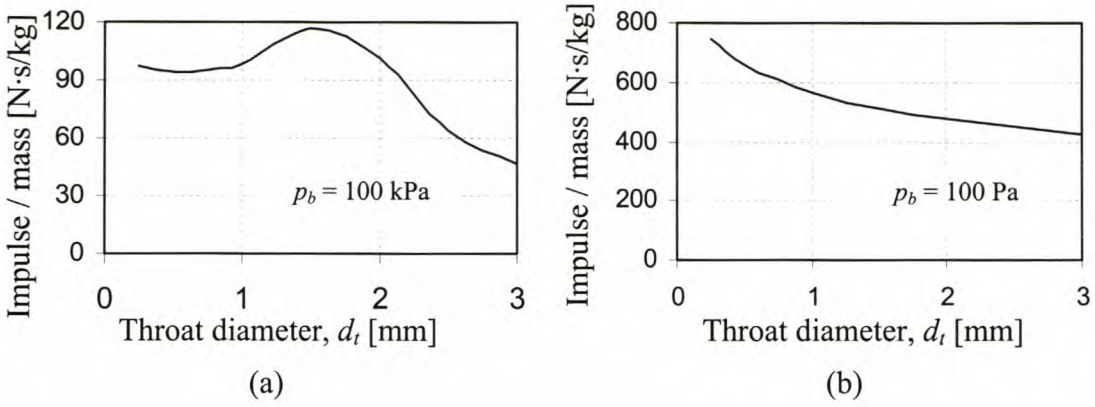

Figure 8.1 Graphs of impulse / mass as a function of throat diameter for back pressure of (a) 100 kPa and (b) 100 Pa

8.3 Butane Properties

In the numerical simulations the properties used for butane were those of normal butane (n-butane). For the experimental work butane used for refilling cigarette lighters was used for reasons of availability, cost and convenience. However, this butane is a mixture of normal butane, iso-butane and propane. The mass mixture ratio given by the manufacturer is: 54 % normal butane, 24 % isobutane and 22 % propane. Hence, the properties used in the simulation program would not be truly accurate, since the butane was assumed to be 100 % pure normal butane.

Even with this assumption there were still difficulties in determining the butane properties. These difficulties were related to obtaining equations to describe the required properties of butane in terms of known properties. Aside from saturation properties, properties of a pure substance are a function of two variables, e.g. $h=f(p,T)$.

Initially it was attempted to fit surfaces to the required properties in order to generate interpolation functions to give properties as functions of pressure and temperature for various pressure ranges using data for superheated normal butane obtained from a website: *http://webbook.nist.gov/chemistry/fluid.* Although these interpolation functions were in general very accurate (typically within 2 %), due to the fact that different functions were used for different pressure ranges, there were slight

discontinuities at the extreme points of the range. Often these discontinuities were large enough to cause simulation programs to run into infinite loops when iterating near an extreme point of a range, since satisfactory convergence could not be obtained because the required property would be determined using a different interpolation function every iteration. In order to solve this problem a more robust, less accurate method was used to estimate certain properties of butane (refer to appendix A.3). This method did not introduce discontinuities during iterations in the computer program. However, this method did not provide as accurate results as the surface fitting method. If a set of interpolation functions using the surface fitting method could be developed, the accuracy of simulations (using 100 % pure normal butane as the propellant) could be improved.

A comparison of various saturation properties for normal butane, iso-butane and propane at 10 °C is given in Table 8.1. It can be seen that for a given temperature the corresponding saturation pressure is approximately 50 % higher for iso-butane than for normal butane, and almost 5 times higher for propane. This explains why the temperature values measured in Figure 7.17, Figure 7.18 and Figure 7.19 were lower than the values given by tabulated data for the saturation temperature corresponding to the given pressure for normal butane.

Table 8.1 Comparison of various properties of saturated normal butane, iso-butane and propane at 10 °C.

	$p_{sat@T}$ [kPa]	h_{fg} [kJ/kg]	C_{p_vap} [kJ/kg·K]	C_{p_liq} [kJ/kg·K]	γ
normal butane	148.7	376.1	1.705	2.367	1.123
iso-butane	220.1	345.8	1.705	2.363	1.136
propane	636.5	359.9	1.869	2.591	1.219

An estimation of the mixture saturation pressure at a temperature of 10 °C can be made using theory of ideal gas mixtures (Çengel and Boles, 1994). A 1 kg mixture consists of normal butane, iso-butane and propane in the ratio specified in the first paragraph of this section. Hence, the mass of normal butane is 0.54 kg, the mass of

iso-butane is 0.24 kg and the mass of propane is 0.22 kg. It is assumed that before mixing, all components of the mixture are at saturation conditions at 10 °C. The specific volumes of the gasses are obtained from saturation property tables and are multiplied by the mass of the respective components to give the volume that each gas occupies before mixing,

$$V_{n-butane} = m_{n-butane}\, v_{n-\,butane} = 0.54 \times 0.25754 = 0.1391 \ \ \mathrm{m^3} \tag{8.2}$$

$$V_{iso-butane} = m_{iso-butane}\, v_{iso-butane} = 0.24 \times 0.17085 = 0.0410 \ \ \mathrm{m^3} \tag{8.3}$$

$$V_{propane} = m_{propane}\, v_{propane} = 0.22 \times 0.07249 = 0.01595 \ \ \mathrm{m^3} \tag{8.4}$$

Adding the three volumes together gives the total volume of the mixture, V_m:

$$\begin{aligned} V_m &= V_{n-butane} + V_{iso-butane} + V_{propane} \\ &= 0.1391 + 0.0410 + 0.01595 = 0.1960 \ \ \mathrm{m^3} \end{aligned} \tag{8.5}$$

In order to calculate the pressure of the mixture p_m the form of the ideal gas equation written in terms of the universal gas constant R_u and the number of moles in the mixture N_m must be used:

$$p_m = \frac{N R_u T_m}{V_m} \tag{8.6}$$

where the value of R_u is 8.314 kJ/(kmol·K) and number of moles N must be in kmol. The molar mass M of normal and iso-butane is 58.1 kg/kmol and the molar mass of propane is 44.1 kg/kmol. Hence, the number of moles each substance is:

$$N_{n-butane} = m_{n-butane} / M_{n-butane} = 0.54 / 58.1 = 0.009294 \ \ \mathrm{kmol} \tag{8.7}$$

$$N_{iso-butane} = m_{iso-butane} / M_{iso-butane} = 0.24 / 58.1 = 0.004131 \ \ \mathrm{kmol} \tag{8.8}$$

$$N_{propane} = m_{propane} / M_{propane} = 0.22 / 44.1 = 0.004989 \ \ \mathrm{kmol} \tag{8.9}$$

Adding the number of moles of each gas, gives the total number of moles for the mixture:

$$\begin{aligned} N_m &= N_{n-butane} + N_{iso-butane} + N_{propane} \\ &= 0.009294 + 0.004131 + 0.004989 = 0.018414 \ \ \mathrm{kmol} \end{aligned} \tag{8.10}$$

The mixture pressure p_m is calculated by substituting the values of N_m, R_u, T_m and V_m into equation 8.6

$$p_m = \frac{0.018414 \times 8.314 \times 283}{0.1960} = 221 \text{ kPa} \quad (8.11)$$

The mixture pressure 221 kPa is closest to the saturation pressure of iso-butane at the mixture temperature of 10 °C – 220 kPa. This is to be expected since the saturation pressure of iso-butane is between that of normal butane and propane. In Figure 7.19 it is suspected that the thermocouple in the storage tank was measuring the vapour pressure of the butane. It can be seen in Figure 7.19(b) that for a pressure of just over 200 kPa in the storage tank the corresponding temperature was about 8 °C. This correlates well with the value calculated previously in this section, i.e. a pressure of 221 kPa for a temperature of 10 °C.

8.4 Experimental and Numerical Results

Typical results for butane firings from a pressure of 200 to 300 kPa into a back pressure of 100 kPa showed a peak thrust of about 50 mN, dropping off to about 30 mN over a period of two seconds (see for example Figure 7.13, Figure 7.14 and Figure 7.16). The peak thrust of 50 mN agrees well with the measured value of 46 mN for butane at 200 kPa reported by Gibbon et al. (2000). However, other details concerning the thruster discussed by Gibbon et al. (2000) are not known. Rise times (from zero to peak thrust) of under 10 ms when operating the nozzle valve were noted (refer Figure 7.14). The correlation of numerical and experimental data was reasonable for butane, and theoretical results for steady thrust were typically 30 % higher than that measured experimentally (compare the theoretical results in Figure 7.6 to the experimental results in Figure 7.14).

In contrast, it can be seen in Figure 7.2 and Figure 7.3 that very good correlation between experimental and numerical results were obtained when using air as a propellant when comparing the theoretical results in Figure 7.1 to the experimental results in Figure 7.11. However, one of the shortcomings of the numerical simulations for air, was that of the transition from super to subsonic flow in the nozzle. It can be seen in Figure 7.1 that just before time 3 s, the thrust profile has a very sudden drop down to zero. The exit to throat area ratio of the nozzle is 25. From the ideal gas dynamics theory used, the minimum stagnation pressure required to induce supersonic flow through the throat is only 100.038 kPa. Hence, sonic flow is

able to be maintained almost all the time until the pressure just about equals the back pressure (100 kPa). By the time the flow becomes subsonic the thrust delivered rapidly decreases since the pressure ratio is very small. However, it must be borne in mind that the mathematical model used did not account for any frictional effects, which would have caused the transition from super to subsonic flow earlier allowing for a more gradual tapering off of the flow without the sharp decline after the transition. But since it is not intended to use air as a propellant for practical applications it is not considered feasible to introduce an additional complexity to the theoretical modelling of the air propulsion system.

8.5 Validity of the Experimental Measurements

As discussed in the previous section, the theoretical results can be construed as being not completely reliable. For that reason the validity of the experimentally measured values is important. In this section the thrust measurement and data acquisition systems will be discussed.

8.5.1 Thrust Measurement Method

The method used to measure thrusts (section 5) was relatively simple and low cost in comparison to most of the other methods discussed previously in section 2.3. The only specialist equipment required was a bridge amplifier and a DAQ card. In addition no numerical differentiation or integration of the signal was required, as would have been the case had a method using an accelerometer been used (for example in the method used by Ziemer et al. (1997), section 2.3). However, the method used does have a number of limitations. A material with a very low Young's modulus must be used in order to ensure that the structure is flexible enough to be affected by the relatively low thrusts produced. In addition this method is susceptible to factors such as strain gauge alignment, vibration of the solenoid valve and nozzle after opening and closing and additional stiffness added to the system by electrical wiring (strain gauges, thermocouples and valve power supply).

8.5.2 DAQ Card Resolution and Noise

An additional limitation of the method used was that the thrust strain resolution due to the DAQ card was limited to 0.005 N (section 6.2.5). In addition there was a problem with interference with noise from the bridge amplifier contaminating the signal. Fortunately, this could be alleviated to a large extent by numerical filtering of the data through a low pass filter.

Temperature measurements taken using the DAQ card were affected by noise from the card with an amplitude equivalent to 1 °C. Filtering using a low pass filter was able to remove most of this high frequency noise from the temperature measurements (section 6.2.4). This problem could be alleviated by the use of commercially available signal conditioning equipment that could be used to amplify the signals from the thermocouples.

8.5.3 Thrust Vector Alignment

A concern when measuring thrusts was that of the alignment of the nozzle, and hence the subsequent thrust vector. Figure 8.2 depicts an ideal thrust F_T aligned along the x-axis. It is assumed that there may be an alignment error of an angle θ of the ideal thrust vector with both the y and z-axis. The thrust due to misalignment is represented by the vector F_T – *actual*, and comprises of the component thrusts in the x, y and z directions – represented by F_x, F_y and F_z respectively.

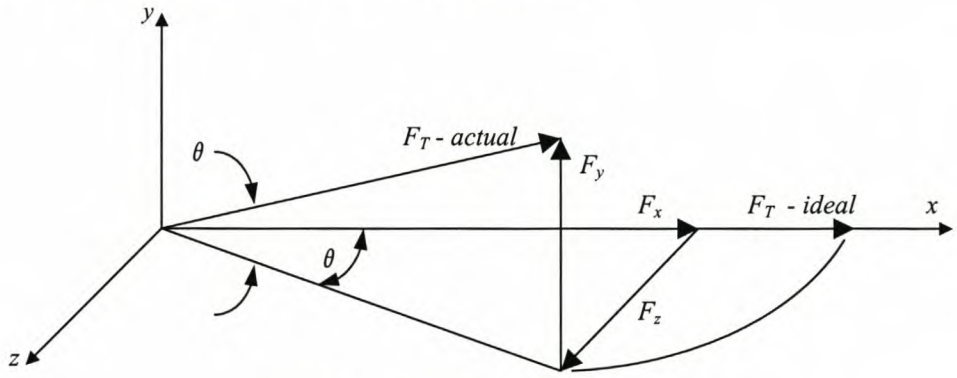

Figure 8.2 Thrust vector alignment

It is desired that the thrust be in the direction of the x-axis. The misalignment results in a reduced value of the thrust in the x-direction F_x given by the following equation:

$$F_x = F_T \cos^2 \theta \tag{8.12}$$

The equation for F_y and F_z, the thrusts in the y and z direction resulting from the misalignment (for small angles) are given by:

$$F_y = F_T \sin \theta \tag{8.13}$$

$$F_z = F_T \cos\theta \sin\theta \approx F_T \sin\theta \tag{8.14}$$

Using equations 8.12, 8.13 and 8.14 the effect of changes in θ on F_x, F_y and F_z can be observed, refer to Figure 8.3. It can be seen from Figure 8.3 that the effect of misalignment on the required thrust F_x is minimal – a 10° misalignment angle only results in a 3 % decrease in thrust. However, the increase in F_y and F_z is more noticeable – 10° misalignment results in an increase in F_x and F_y from zero to 0.2 N, 20 % of the value of ideal thrust in the x direction. Since the effect of the required thrust F_x is minimal and is less than for example the influence of the DAQ card noise, the possible misalignment was not a source of concern for the thrust measurements made in this project.

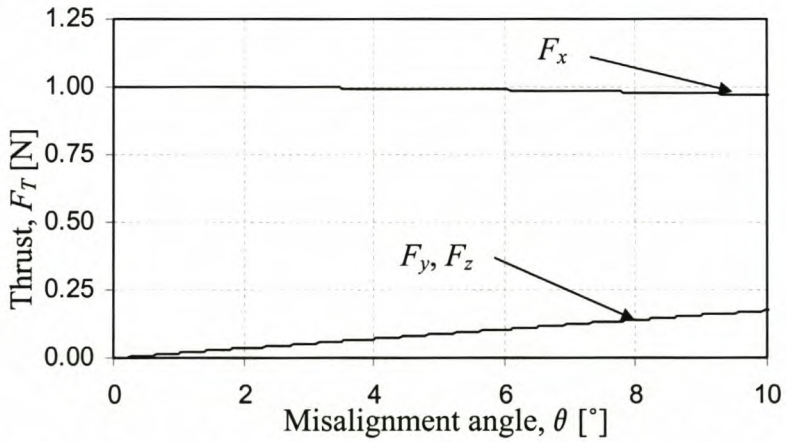

Figure 8.3 Effect of misalignment angle on thrust for a thrust of 1 N

8.6 DAQ Software Limitations

All control and measurements on the experimental model were done through a computer communicating with the DAQ card. The software used for communication with the DAQ card was *LabVIEW 6.1*. The basic structure of the program is discussed in appendix D, where it is shown that because control of the valves was

necessary, the maximum sampling frequency that could be attained (irrespective of computer speed) was 1 000 Hz. For the computer used in the laboratory (clock speed of 633 MHz), the maximum sampling speed that could be achieved when conducting butane experiments (measurement of pressure strains, thrust strain and temperature) was 50 Hz. This is regarded as being somewhat low for thrust measurement. Use of a faster computer with a clock speed in the region of 2.4 GHz would make it possible to sample at a faster rate, possibly as high as 100 Hz. Alternatively, the use of different software for control and sampling could be investigated.

8.7 Use of Perspex

As mentioned in section 6.1, most of the experimental model was constructed from perspex. There were two main reasons for the choice of perspex. Firstly, perspex allowed one to observe the behaviour of the propellant inside the storage tank and accumulator. Secondly, the low Young's modulus ($E = 3\times10^9$ N/m^2) of perspex was suitable for the measurement method used. However, there were disadvantages associated with the use of perspex.

From a manufacturing and handling point of view perspex is a difficult material to work with as it is brittle and has a low strength (yield strength typically 50 MPa). Frequent breaking of components occurred during machining and handling. In addition special teflon ferrules had to be manufactured for use on the perspex tubing when connecting it to male pipe connector fittings. This was because the standard brass ferrules supplied with the fittings could not be used as they would have cracked the perspex.

It was also noted that there was an adverse reaction of the perspex to the butane. After a few weeks of testing many fine cracks and stress lines could be seen on parts on the perspex, particularly in the storage tank. However, the damage was only on the surface and did not directly result in any material failures occurring.

8.8 Heating Elements

The construction of the electrical heating elements was discussed in section 6.1. These heating elements (especially the one in the storage tank) were found to be extremely unreliable and prone to breakages. It is likely that these breakages were due to the fact that the heating elements were self-made. The purchase of a heating element made by a specialist company would probably have been a better option. In addition there was an associated danger due to the possibility of the highly flammable butane coming into contact the hot resistance wires. These two problems (unreliability and danger) could be solved by use of a heat pipe to provide heat input to the propellant. This was done theoretically and is discussed in section 4.4.6. A heat pipe is far more robust than an electrical heating element. In addition the possibility of the butane coming into contact with hot electrical wires would not exist.

Referring to Figure 4.15 the effect of required heat input $\dot{Q}$ on the evaporator and condenser lengths L_e and L_c of the heat pipe can be investigated. The following scenario was assumed: 0.1 kg of butane at 10 °C is to be heated with a heat pipe of diameter d 0.01 m to 20 °C. A constant heat input $\dot{Q}$ can be supplied to provide a constant temperature difference between the condenser section of the heat pipe and the butane. The convective heat transfer coefficient between the condenser section and the butane h_c is assumed to be 1000 W/m^2·K (refer to section 4.4.6). In addition it is assumed that the maximum allowable heat flux input to the evaporator section is 1 W/cm^2. It is required to determine the following: the time t required to heat the butane, the minimum length of the evaporator section L_{e_min} to ensure that the heat flux input to the evaporator section does not exceed 1 W/cm^2 and the required length of the condenser section L_c. The heat flux and temperature difference were varied and the effects on time, evaporator length and condenser length observed. Results for the minimum evaporator length can be found in Figure 8.4(a). Time required for heating is presented in Figure 8.4(b). Minimum evaporator length and time required are both independent of temperature difference for a specified heat flux. Required condenser length for different temperature differences as a function of heat input is depicted in Figure 8.5.

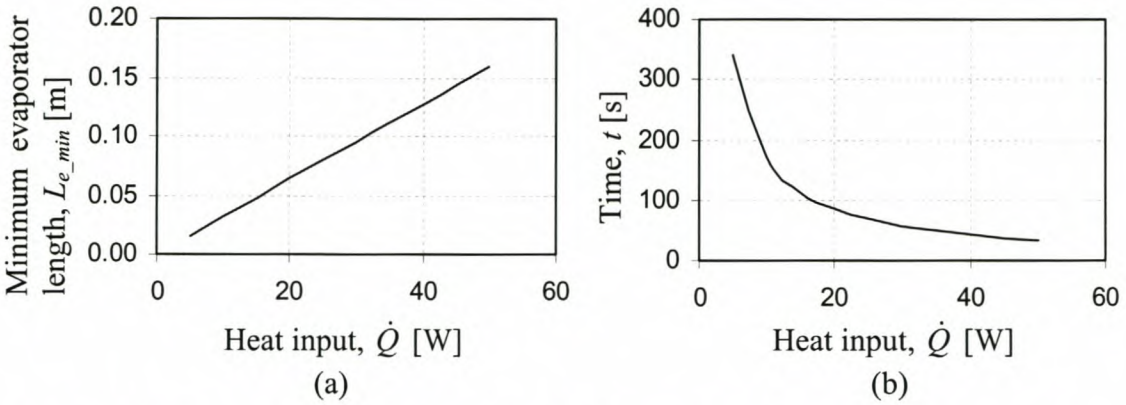

Figure 8.4 Minimum evaporator length (a) and time required (b) as a function of heat input

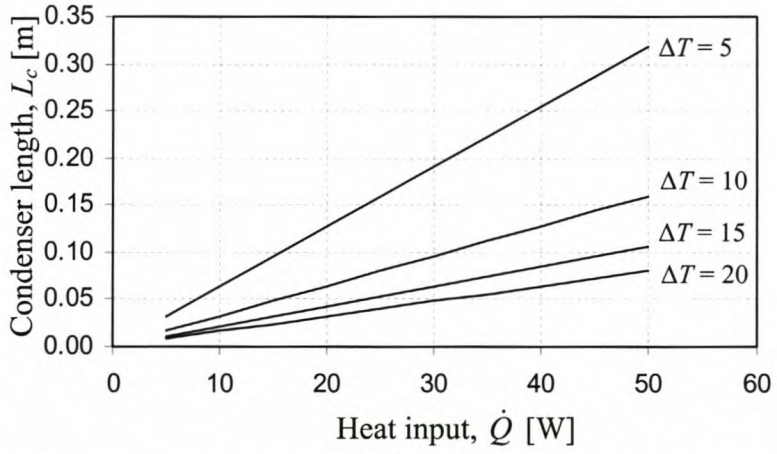

Figure 8.5 Required condenser length for various temperature differences as a function of heat input

It can be seen in Figure 8.4(a) that the minimum evaporator length increases linearly with heat input to a maximum value of just over 0.15 m for a heat input of 50 W. Making use of a heat pipe with a larger diameter would decrease the required length. Similarly a smaller heat pipe diameter would increase the required length. In Figure 8.4(b) it is seen that the time required for heating is inversely proportional to increases in the heat input. Figure 8.5 shows that while the required condenser length increases linearly with heat input, it is inversely proportional to increases in temperature difference between the condenser section and the butane.

9 RECOMMENDATIONS

This section presents the recommendations made for future work to be undertaken relating to this project, based on the experience drawn from this project. It is intended to serve as a starting point for any further work relating to the design, development and optimisation of a liquefied-gas thruster system for a micro-satellite. Recommendations are made regarding the main aspects focussed on for this project, e.g. numerical simulation, thrust measurement, experimental models, measurement and control.

9.1 Thermo-Fluid Modelling of System

Based on the limitations discussed in the section 8.1 and 8.3 it is recommended that a project be undertaken with the sole focus on the detailed numerical simulation of the thermo-fluid behaviour of the propellant in the thruster system. Specifically, it is recommended that attention be given to the following aspects: modelling of the two-phase behaviour of the propellant inside the storage tank, development of a procedure to model the mass transfer between liquid and vapour under changing pressure environments, subdivision of the main control volumes into smaller control volumes, i.e. making use of a finer grid, incorporation of the momentum equation as one of the governing equations. Use of commercially available computational fluid dynamics (CFD) software could also be considered as it will make more detailed analyses possible.

9.2 Experimental Work

Whilst a numerical model is a powerful tool, the importance of experimental work using physical models should not be neglected. Due to the many complexities involved in predicting the thrust, any simulation program should always be checked against experimental work. The experimental work conducted for this project used locally available components that were relatively cheap (when compared to space-qualified components). Nevertheless, reasonable experimental results were obtained that compared well to those given by Gibbon and Underwood (2001) (refer to section

2 for more details). This serves to stress the usefulness of even relatively crude practical models. However, it is recommended that a system incorporating as many of the actual components intended to be flown in space be designed and built for experimental testing. In particular the purchase of genuine space-qualified thruster valves is recommended in order to examine their effect on thrust produced.

9.3 Thrust Measurement

The measurement method used (section 5.1) required the use of a material with a low Young's modulus (in this case perspex with E = 3 GN/m^2) in order for the resultant strains to be large enough to be picked up by the strain gauges. However, it is likely that a much stronger material would be used on the actual system intended to be flown in space. Hence, if it is intended to test a more realistic model (using typically titanium or aluminium for the tubing of the system) a different method of measurement would be required, since these materials are much stiffer than perspex. The air-bearing table being considered by the Electrical Engineering Department at the University of Stellenbosch could be a possible option. However, this would not allow for testing under vacuum conditions. Use of the method described by Toyoda et al. (2001) could be investigated as a possible method since it allows for testing in a vacuum chamber and does not require any numerical integration or differentiation of the measured signal.

9.4 General Recommendations

9.4.1 Use of Heat Pipes

The use of a heat pipe to provide energy to the propellant has already been mentioned (refer section 4.4.6 and 8.8). However, in the experimental work conducted all heating of the propellant was achieved making use of self-made electrical heating elements. Hence, it is recommended that for future experimental models heat pipes are used to transfer energy to the propellant. It would also be preferable to experiment with a number of different heat pipes in order to be able to compare performance.

9.4.2 Vacuum Chamber Testing

Results between atmospheric and vacuum testing are compared in section 7, where the significance of the back pressure to which the nozzle exhausts is illustrated in Figure 7.3 and Figure 7.8. However, the minimum pressure that could be achieved in the vacuum chamber used was 20 kPa absolute. This is mainly due to the fact that the actual size of the vacuum chamber was relatively large in volume in comparison to the capacity of the pump used, as well as the condition of the pump itself, to evacuate air from the chamber. Using a smaller vacuum chamber would allow for the use a smaller vacuum pump with lower investment and maintenance costs. Such a system should be able to achieve a pressure of lower than 20 kPa, say 1 kPa, which would make it possible to adequately verify thruster performance in simulated space conditions.

A lot of breakages on the physical model were also experienced in attaching and removing the experimental model to and from the vacuum chamber due to limited access through the portholes to the base-plate on which the model was mounted. If it is intended to perform an extensive reliability testing program on thruster systems then attention should be given to design of improved access to the vacuum chamber.

10 REFERENCES

Agrawal, B.N., *Design of Geosynchronous Spacecraft*, Prentice-Hall, New Jersey, 1986

American Society of Heating, Refrigerating and Air-Conditioning Engineers, Inc, *2001 ASHRAE Handbook – Fundamentals*, Atlanta, 2001

Anderson, J.D., *Modern Compressible Flow with Historical Perspective*, 2nd Edition, McGraw-Hill, Boston, 1990

Baruh, H., *Analytical Dynamics*, McGraw-Hill, Singapore, 1999

Bayt, R.L., Ayon, A.A., Breuer, K.S., *A Performance Evaluation of MEMS-based Micronozzles*, AIAA 97-3169, Proceedings of 33rd AIAA/ASME/SAE/ASEE Joint Propulsion Conference, Seattle, 1997

Benham, P.P, Crawford, R.J., Armstrong, C.G, *Mechanics of Engineering Materials*, Longman, London, 1999

Boctor, S.A., Ryff, P.F., Hiscocks, P.D., Ghorab, M.T., Holmes, M.R., *Electrical Concepts and Applications*, West, St. Paul, 1997

Braslow, A.L., *Propellant Slosh Loads*, NASA SP-8009, 1968

Cardin, J.M., Acosta, J., *Design and Test of an Economical Cold Gas Propulsion System*, Proceedings of the 14th Annual AIAA/USU Conference on Small Satellites, Logan, Utah, 2000

Carey, V.P., *Liquid-Vapour Phase-Change Phenomena*, Hemishphere, Washington, 1992

Cengel, Y.A., Boles, M.A., *Thermodynamics – an Engineering Approach*, 2nd Edition, McGraw-Hill, New York, 1994

Chi, S.W., *Heat Pipe Theory and Practice*, Washington, Hemisphere Publishing Company, 1976

Dobson, R.T., Scowby, S.T., *Thermal Modelling of an Axial Flux Permanent Magnet (AFPM) Machine*, Applied Thermal Engineering, at printers, 2003

Dodge, F.T., Garza, L.T., *Experimental and Theoretical Studies of Liquid Sloshing at Simulated Low Gravity*, Journal of Applied Mechanics, 1967, pp. 555-562

Dunn, P.D., Reay, D.A., *Heat Pipes*, 4th Edition, Pergamon, Oxford, 1994

Faghri, A., *Heat Pipe Science and Technology*, Taylor and Francis, Washington, 1995

Garrison, P.W., Stocky, J.F., *Future Spacecraft Propulsion*, Journal of Propulsion, Vol 4., No.6., 1998

Gerald, C.F., Wheatley, P.O., *Applied Numerical Analysis*, Addison-Wesley, 6th Edition, Reading, Massachusetts, 1999

Gibbon, D., Underwood, C., *Low cost butane propulsion systems for small spacecraft*, Proceedings of the 15th Annual AIAA/USU Conference on Small Satellites, Logan, Utah, 2001

Gibbon, D., Ward, J., Kay, N., *The Design, Development and Testing of a Propulsion System for the SNAP-1 Nanosatellite*, Proceedings of the 14th Annual AIAA/USU Conference on Small Satellites, Logan, Utah, 2000

Hansen, F., *Small Satellite Propulsion System*, Danish Space Research Institute, 1999

Inman, D.J., *Engineering Vibration*, Prentice-Hall, New Jersey, 1996

Köhler, J., Bejhed, J., Kratz, H., Bruhn, F., Lindberg, U., Hjort, K., Stenmark, L., *A hybrid cold gas microthruster system for spacecraft*, Sensors and Actuators A 3199, 2003, pp. 1 - 12

Larson, W.J., Wertz, J.R., *Space Mission Analysis and Design*, 2nd Edition, Microcosm, 1992

Megson, T.H.G., *Aircraft Structures for Engineering Students*, Butterworth Heinemann, Oxford, 1999

Meirovitch, L., *Analytical Methods in Vibration*, Macmillan, New York, 1967

Mills, A.F., *Heat and Mass Transfer*, Richard D. Irwin, Chicago, 1995

Mukerjee, E.V., Wallace, A.P., Yan, K.Y., Howard, D.W., Smith, R.L., Collins, S.D., *Vaporizing liquid microthruster*, Sensors and Actuators 83, 2000, pp. 231 – 236

Müller, J.C., *Draft Specification for a Thruster System for a Micro-Satellite*, Sunspace, Stellenbosch, 2003

Peterson, G.P., *An Introduction to Heat Pipes*, Wiley-Interscience, New York, 1994

Pisacane, V.L., Moore, R.C., *Fundamentals of Space Systems*, Oxford University Press, New York, 1994

Potter, M.C., Wiggert, D.C., Hondzo, M., Shih, T.I-P., *Mechanics of Fluids*, 3rd Edition, Wadsworth, Crawfordsville, 2002

Rhee, M.S., Zakrzwski, C.M., Thomas, M.A., *Highlights of Nanosatellite Propulsion Development Program at NASA-Goddard Space Flight Centre*, Proceedings of 14th Annual AIAA/USU Conference on Small Satellites, Logan, Utah, 2000

Toyoda, K., Komurasaki, K., Arakawa, Y., *Thrust peformance of a CW laser thruster in a vacuum*, Vacuum 0, 2001, pp. 1 – 6

Whalley, P.B., *Boiling, Condensation and Gas-Liquid Flow*, Claredon Press, Oxford, 1987

White, F.M., *Fluid Mechanics*, McGraw-Hill, Singapore, 1999

Ye, X.Y., Tang, F., Ding, H.Q., Zhou, Z.Y., 2001, *Study of a vaporizing water micro-thruster*, Sensors and Actuators A 89, 2001, pp. 159 – 165

Younger, D.W., Lu, S.T., Choueiri, E., Neidert, J.B., Black, R.E., Graham, K.J., Fahey, D., Lucus, R., Zhu, X., *MEMS Mega-pixel Micro-thruster Arrays for Small Satellite Stationkeeping*, Proceedings of the 14th Annual AIAA/USU Conference on Small Satellites, Logan, Utah, 2000

Zakirov, V., Sweeting, M., Erichsen, P., Lawrence, T., *Specifics of Small Satellite Propulsion: Part 1*, Proceedings of the 15th Annual AIAA/USU Conference on Small Satellites, Logan, Utah, 2001

Ziemer, J.K., Cubbin, E.A., Choueiri, E.Y., Birx, D., *Performance Characterisation of a High Efficiency Gas-Fed Pulsed Plasma Thruster*, AIAA-97-2925, Proceedings of 33rd AIAA Joint Propulsion Conference, Seattle, Washington, 1997

APPENDIX A: CORRELATIONS FOR BUTANE PROPERTIES

In order to run the simulations discussed in section 4 certain thermodynamic properties of butane were required. In addition it was necessary to investigate if the ideal gas equation of state was valid in the range that was worked in.

A.1 Validity of Ideal Gas Equations

If it is known that the ideal gas equation is valid then it would make computation of certain properties of butane much simpler. The ideal gas equation of state relates the pressure p, density ρ and temperature T to each other through the use of gas constant R as follows:

$$R = p / \rho T \tag{A.1}$$

It is desired to determine a value of R that will hold over the working range of temperature and pressures. To do this, a number of random states were chosen by specifying temperature and pressure. The density corresponding to each state was then obtained from a table of properties for superheated butane. The value of R was then determined using equation A.1. The average value of R was calculated and the percentage error of R at each point was calculated relative to R_{ave}. Data for the properties for superheated butane was obtained from an internet website: http://webbook.nist.gov/chemistry/fluid.

A table containing p, T, ρ and R, R_{ave} and percentage error of R relative to R_{ave} is presented in Table A.1. The range from which pressure and temperature points were chosen was (p_{min} = 10 kPa, $T_{min@pmin}$ = 195 K), (p_{max} = 500 kPa, $T_{max@pmax}$ = 375 K). It can be seen that for R_{ave} = 137.875 J/kg·K. Errors were typically in the order of a few percent with the maximum error of just under 9 %. However, this was at the maximum pressure and hence on the extreme limit of the specified range. Based on these results it was decided that the ideal gas equation of state was valid for the specified working range.

Table A.1 Properties of superheated butane at selected states

p [Pa]	T [K]	ρ [kg/m^3]	R [J/kg·K]	% error
1000	195	0.036514	140.4449	1.930674
1000	300	0.023308	143.0124	3.794097
10000	225	0.31315	141.927	3.006347
10000	300	0.23368	142.6452	3.527594
50000	260	1.3771	139.6469	1.35148
50000	330	1.0703	141.5633	2.742341
100000	275	2.6473	137.3612	-0.30737
100000	350	2.0321	140.6005	2.043606
300000	310	7.348	131.7014	-4.41509
300000	360	6.1202	136.1611	-1.17836
500000	325	12.255	125.5375	-8.8887
500000	375	10.039	132.8154	-3.60662
			R_{ave} =137.7847	

A.2 Saturation Properties for Butane

Since it was required to numerically simulate the two-phase behaviour of both liquid and vapour butane, correlations for the saturation properties were required. The source data for these correlations was obtained from the 2001 ASHRAE Handbook of Fundamentals. Properties for normal butane were used,. The following correlations were required:

Enthalpy of saturated vapour given pressure: $h_{g\_sat@P}$

$$h_{g\_sat@P} = a_0 + a_1 p + a_2 p^2 + a_3 p^3 + a_4 p^4 + a_5 p^5 + a_6 p^6 \qquad \text{(A.2)}$$

p in MPa, $h_{g\_sat@}$ in kJ/kg, Range: $170 - 2.214\times10^6$ Pa

Enthalpy of saturated vapour given temperature: $h_{g\_sat@T}$

$$h_{g\_sat@T} = a_0 + a_1 T \qquad \text{(A.3)}$$

T in K, $h_{g\_sat@T}$ in kJ/kg, Range: 173 – 393 K

Enthalpy of saturated liquid given temperature: $h_{f\_sat@T}$

$$h_{f\_sat@T} = a_0 + a_1 T \qquad \text{(A.4)}$$

T in K, $h_{f\_sat@T}$ in kJ/kg, Range: 173 – 393 K

Saturation temperature given pressure $T_{sat@P}$

$$T_{sat@P} = a_1 P^{a_2} \tag{A.5}$$

$T_{sat@P}$ in K, p in MPa, Range: 170 – 2.214×10^6 Pa

Saturation pressure given temperature $P_{sat@T}$

$$P_{sat@T} = a_0 + a_1 T + a_2 T^2 + a_3 T^3 + a_4 T^4 + a_5 T^5 + a_6 T^6 \tag{A.6}$$

$P_{sat@T}$ in Pa, T in K, Range 173 – 393 K

Specific heat at constant pressure of saturated vapour given pressure: $C_{p\_v\_sat@p}$

$$C_{p\_v\_sat@p} = a_0 + a_1 p + a_2 p^2 + a_3 p^3 + a_4 p^4 + a_5 p^5 + a_6 p^6 \tag{A.7}$$

p in Pa, $C_{p\_v\_sat@p}$ in kJ/kg·K, Range: 176 – 2.214×10^6 Pa

Specific heat at constant pressure of saturated vapour given temperature: $C_{p\_v\_sat@T}$

$$C_{p\_v\_sat@T} = a_0 + a_1 T + a_2 T^2 + a_3 T^3 + a_4 T^4 + a_5 T^5 + a_6 T^6 \tag{A.8}$$

T in K, $C_{p\_v\_sat@T}$ in kJ/kg·K, Range: 173 – 393 K

Specific heat at constant volume of saturated liquid given temperature: $C_{v\_f\_sat@T}$

$$C_{v\_f\_sat@T} = a_0 + a_1 T + a_2 T^2 + a_3 T^3 + a_4 T^4 + a_5 T^5 + a_6 T^6 \tag{A.9}$$

$C_{v\_f\_sat@T}$ in kJ/kg·K, T in K, Range: 173 – 293 K

Specific heat at constant volume of saturated vapour given pressure: $C_{v\_v\_sat@p}$

$$C_{v\_v\_sat@p} = C_{p\_v\_sat@p} / \gamma_p \tag{A.10}$$

Specific heat at constant volume of saturated vapour given temperature: $C_{v\_v\_sat@T}$

$$C_{v\_v\_sat@T} = C_{p\_v\_sat@T} / \gamma_T \tag{A.11}$$

Specific heat ratio given temperature: γ_T

$$\gamma_T = a_0 + a_1 T + a_2 T^2 + a_3 T^3 + a_4 T^4 + a_5 T^5 + a_6 T^6 \tag{A.12}$$

T in K, Range 173 – 293 K

Specific heat ratio given pressure: γ_p

$$\gamma_p = a_0 + a_1 p + a_2 p^2 + a_3 p^3 + a_4 p^4 \tag{A.13}$$

p in Pa, Range: 176 – 2.214×10^6 Pa

Table A.2 Constants required for determining enthalpies

	$h_{g\ sat@P}$ [kJ/kg]	$h_{g\ sat@T}$ [kJ/kg]	$h_{f\ sat@T}$ [kJ/kg]
a_0	499.41673369	212.22472	-450.33821885
a_1	1827.4387928	1.36767845	2.4110470043
a_2	-16465.82189		
a_3	89290.223628		
a_4	-262437.31858		
a_5	389372.43172		
a_6	-228405.22681		

Table A.3 Constants required for determining specific heats

	$C_{P\ v\ sat@P}$ [kJ/kg·K]	$C_{P\ v\ sat@T}$ [kJ/kg·K]	$C_{v\ f\ sat@T}$ [kJ/kg·K]
a_0	1.33245678	50.8875374016	3.500620668544
a_1	$3.77708027 \cdot 10^{-6}$	-1.2013129348	0.153463107274
a_2	$-1.04854641 \cdot 10^{-11}$	0.01191107577	$1.753976967145 \times 10^{-3}$
a_3	$1.60893995 \cdot 10^{-17}$	$-6.215878596 \cdot 10^{-5}$	$1.010031394758 \times 10^{-5}$
a_4	$-1.23453909 \cdot 10^{-23}$	$1.805204062 \cdot 10^{-7}$	$3.114709960910 \times 10^{-8}$
a_5	$4.58090578 \cdot 10^{-30}$	$-2.76595000 \cdot 10^{-10}$	$4.962068207859 \times 10^{-11}$
a_6	$-6.52050107 \cdot 10^{-37}$	$1.74927500 \cdot 10^{-13}$	$-3.22362514455 \times 10^{-14}$

Table A.4 Constants required for determining saturation temperature and pressure

	$T_{sat@P}$ [K]	$P_{sat@T}$
a_0		146337.85507
a_1	110.1415923372	-3203.925443
a_2	0.07949860116759	29.168518197
a_3		-0.14130314584
a_4		0.0003841524572
a_5		$-5.5610914151 \cdot 10^{-7}$
a_6		$3.3583863294 \cdot 10^{-10}$

Table A.5 Constants required for determining specific heat ratio

	γ_p	γ_T
a_0	1.1205904037	21.723847276
a_1	$5.6676487041 \cdot 10^{-9}$	-0.49384643117
a_2	$1.427359818 \cdot 10^{-13}$	0.0048840127034
a_3	$-8.6220467835 \cdot 10^{-20}$	$-2.5481543164 \cdot 10^{-5}$
a_4	$2.4367340036 \cdot 10^{-26}$	$7.3940979415 \cdot 10^{-8}$
a_5		$-1.132010704 \cdot 10^{-10}$
a_6		$7.1548320528 \cdot 10^{-14}$

A.3 Determining Enthalpy of Superheated Vapour

For a calorically perfect gas the enthalpy is a function of temperature alone. However, for a non-calorically perfect gas the enthalpy is a function of both temperature and pressure, i.e. $h=f(p,T)$. It is possible to fit surfaces to tabulated data, however, this leads to a problem with discontinuities between different pressure or temperature ranges which in turn leads to problems with convergence in iteration algorithms. Thus, a method had to be used that would not give discontinuities.

Refer to the *T-s* diagram in Figure A.1, and consider the point 1 and temperature T_1 and pressure p_1. The saturated fluid and vapour state at the given temperature are given by f_T and g_T respectively. The saturated fluid and vapour state at the given pressure are given by f_p and g_p respectively.

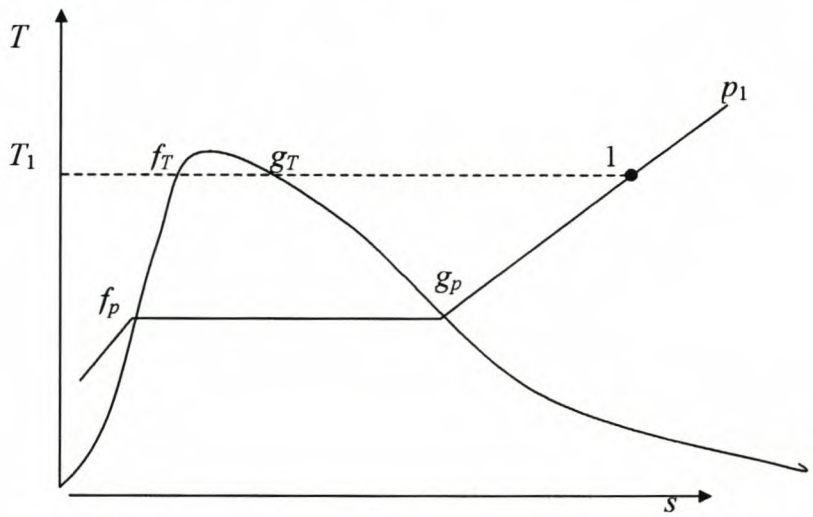

Figure A.1 Method to determine enthalpy in superheated state

It is necessary to estimate the enthalpy h of a superheated vapour whose temperature and pressure are known. This is achieved by working up along the isobaric line of pressure P_1. It is easy using saturated property tables to obtain by curve-fitting a function giving h_g as a function of pressure. With h_g known, the additional enthalpy due to superheating is determined by moving up along is the isobar from g_P to 1. This is done by making use of the relation for change in enthalpy:

$$\Delta h=C_p\,\Delta T \tag{A.14}$$

Although the value of C_p varies in moving from g_P to 1, it is approximated by averaging the values of C_p at saturated pressure and temperature, i.e.

$$C_p = 0.5\left(C_{p\,@\,Psat} + C_{p\,@\,Tsat}\right) \tag{A.15}$$

Hence, the formula used to determine the enthalpy h of superheated vapour is

$$h = h_{g\,@\,Psat} + 0.5\left(C_{pg\,@\,P} + C_{pg\,@\,T}\right)\left(T - T_{sat\,@\,P}\right) \tag{A.16}$$

APPENDIX B: NUMERICAL METHODS IMPLEMENTED

B.1 Secant Method For Solving Equations

The secant method is an iterative method used to determine a root x which will satisfy the relation $y = f(x) = C$. Unlike Newton's method, the secant method does not require an analytical expression for df / dx.

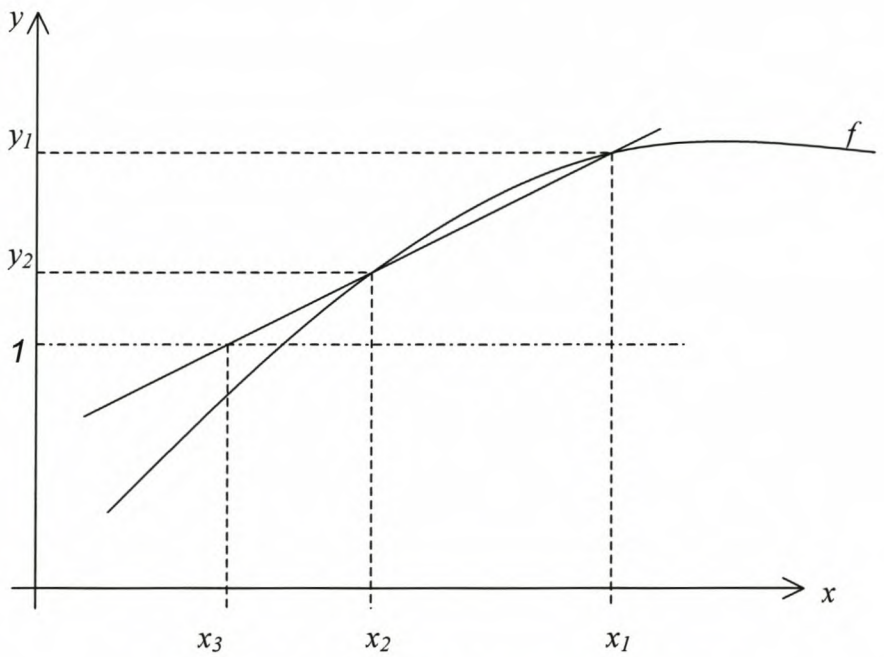

Figure B.1 Sketch illustrating secant method

Given a function $y = f(x)$, it is required to find a root x which will satisfy the relation $y = C$, within in a specified tolerance. Before this method can be implemented it is necessary to find by iterations the roots x_1 and x_2. A new root x_3 is then found by constructing a straight line through the points (x_1, y_1) and (x_2, y_2) and finding the value of the x where this line intersects with the horizontal line $y = C$. The gradient m of the line connecting points (x_1, y_1) and (x_2, y_2) is

$$m = \frac{y_2 - y_1}{x_2 - x_1} \tag{B.1}$$

It can be seen that since the point (x_3, C) lies on the same straight line, the equation for x_3 is

$$x_3 = \frac{C - y_2}{m} + x_2 \tag{B.2}$$

Using the above procedure, subsequent roots x_4, x_5, ... x_n can be determined until $f(x_n)$ is sufficiently close to C.

Algorithm for Implementation of the Secant Method

x_1 = guessed value from user
x_2 = guessed value from user
$y_1 = f(x_1)$
$y_2 = f(x_2)$
$i = 2$
$Error = |C - f(x_2)|$
While $Error > Error\_tolerance$
    $i = i + 1$
    $m = (y_{i-1} - y_{i-2})/(x_{i-1} - x_{i-2})$
    $x_i = (C - y_{i-1})/m + x_{i-1}$
    $Error = |C - f(x_i)|$
Loop

$x_{root} = x_i$

B.2 Bisection Method for Equation Solving

The bisection method (or interval halving method) is an alternative procedure for determining a root x that satisfies the relation $f(x) = 0$. In some cases the secant method described in the previous section is unsuitable if the gradient of the function is very steep. An example of a case where the secant method was found to unsuitable was in attempting to solve for the exit Mach number in the Mach area relation (equation 3.20). In this case the bisection method was more suitable. This method requires that two values enclosing the root are known, i.e. if x_1 and x_2 are the values enclosing the root, then $f(x_1) \cdot f(x_2) < 0$. This interval is halved to give the new root $x_3 = (x_1 + x_2)/2$. If $f(x_3) \cdot f(x_2) < 0$ then the root will lie in the interval between x_1 and x_3. Otherwise the root will lie in the interval between x_3 and x_2. This process of halving

the interval enclosing the root is continued until the interval is within a specified tolerance value. For more details refer Gerald and Wheatley (1999).

Algorithm for Bisection Method

In this method it is required to determine root of $f(x) = 0$ that is accurate to within specified tolerance values, given the values x_1 and x_2 such that $f(x_1) \cdot f(x_2) < 0$,

Repeat

$x_3 = (x_1 + x_2)/2$

If $f(x_3) \cdot f(x_2) < 0$ then

$x_2 = x_3$

Else

$x_1 = x_3$

End if

Until ($|x_1 - x_2| < 2 \times$ tolerance value) or $f(x_3) = 0$

B.3 Solving Ill-Conditioned System of Linear Equations

The numerical method used to solve the non-linear system of equations describing the flow between two points in the nozzle, requires that a linear system of equations be solved in order to determine the difference vector **d**. The matrix **A** was determined by partially differentiating each of the three governing equations with respect to the three unknown values. Since the governing equations all have differing units (continuity: kg/s, momentum: N, energy: J), as well as the unknown values (Pa, K, m/s) this leads to large differences in orders of magnitude between the elements of the matrix. This is referred to as an *ill-conditioned system*, and is extremely sensitive to computer round-off errors. If computers had infinite precision then no additional steps would be required and the solution could be obtained by a direct solution technique. However, computer accuracy is limited and two techniques were used to minimise possible round-off errors: *partial pivoting* and *scaling* (refer Gerald and Wheatley, 1999).

Partial pivoting places a coefficient of larger magnitude by making use of row interchanges. It guarantees a nonzero divisor if there is a solution to the set of equations, and has the additional advantage of improved arithmetic precision.

Scaling is the operation of adjusting the coefficients of a set of equations so that they are all of the same order of magnitude. If pivot elements are selected without scaling, pivoting may put numbers of the diagonal that are not large compared to others in their row. Scaling is achieved by dividing each row by the magnitude of the largest coefficient in that row.

Once scaling and pivoting have been performed on the system, it is necessary to solve the system. Since, the system worked with was only a 3 x 3 system, Gaussian elimination could be used.

Algorithm for scaling, pivoting and solving system of *n* linear equations: Ax = b

```
{perform scaling on system}
For i = 1 To n
        max_coeff = |A_i,1|

        For j = 2 To n
                If |A_i,j| > max_coeff Then
                        max_coeff = |A_i,j|
                End If
        End For j

        For j = 1 To n
                A_i,j = A_i,j / max_coeff
        End For j

        b_i = b_i / max_coeff
End For i

{perform partial-pivoting on system}
For j = 1 To (n - 1)
        pvt = |A_j,j|
        pivot_j = j
        ipvt_temp = j

        For i = (j + 1) To n
                If |A_i,j| > pvt Then
                        pvt = |A_i,j|
                        ipvt_temp = i
                End If
```

End For i

{switch rows if necesary:}
If $pivot_j$ <> $ipvt\_temp$ Then

For $i = 1$ To n
$temp\_1_i = \mathbf{A}_{j,i}$
$temp\_2_i = \mathbf{A}_{ipvt\_temp,i}$
End For i

For $i = 1$ To n
$\mathbf{A}_{j,i} = temp\_2_i$
$\mathbf{A}_{ipvt\_temp,i} = temp\_1_i$
Next i

$b\_temp\_1 = \mathbf{b}_j$
$b\_temp\_2 = \mathbf{b}_{ipvt\_temp}$
$\mathbf{b}_j = b\_temp\_2$
$\mathbf{b}_{ipvt\_temp} = b\_temp\_1$

End If

{Store multipliers}
For $i = j + 1$ To n
$\mathbf{A}_{i,j} = \mathbf{A}_{i,j} / \mathbf{A}_{j,j}$
End For i

{Create zeros below the main diagonal}
For $i = j + 1$ To n
For $k = j + 1$ To n
$\mathbf{A}_{i,k} = \mathbf{A}_{i,k} - \mathbf{A}_{i,j} * \mathbf{A}_{j,k}$
Next k
$\mathbf{b}_i = \mathbf{b}_i - \mathbf{A}_{i,j} * \mathbf{b}_j$
End For i

End For j

{Back Substitution:}
$\mathbf{x}_n = \mathbf{b}_n / \mathbf{A}_{n,n}$

For $j = n - 1$ Down To 1
$\mathbf{x}_j = \mathbf{b}_j$

For $k = n$ Down To j + 1
$\mathbf{x}_j = \mathbf{x}_j - \mathbf{x}_k * \mathbf{A}_{j,k}$
Next k

$\mathbf{x}_j = \mathbf{x}_j / \mathbf{A}_{j,j}$

End For j

APPENDIX C: CALIBRATION CALCULATIONS

When using a bridge amplifier to measure strains from strain gauges it is necessary to set a calibration signal corresponding to a specified voltage change over the bridge. For the experimental measurements done for this project this calibration signal was always set to the maximum value of 10 V for a change of 1 mV/V over the bridge, and then the calibration equations were used to convert the sampled voltages to engineering units. The bridge amplifier used was a Hottinger Baldwin Messtechnik 5kHz TF-Messverstärker, type DIN 57411, serial number 92189. In this section the value of the calibration signals are determined from theoretical principles.

C.1 Theoretical Thrust Calibration

In this section the value to which the calibration signal on the bridge amplifier must be set to for thrust measurements is calculated using the theory presented in section 5.3. From equation 5.43 the expression for the ratio of output to input voltage in terms of the axial strain ε_x and gauge factor K is

$$\frac{V_{out}}{V_{in}} = \frac{K}{2}\varepsilon_x \tag{C.1}$$

For the bridge amplifier used the input voltage V_{in} applied over the bridge is 1 V. The calibration signal on the bridge amplifier allows the user to set the calibration signal for a 1 mV/V change over the bridge. It is required to work out what this calibration signal must be. Table C.1 lists the parameters of the cantilevered arm used to measure thrust.

Table C.1 Parameters of cantilevered arm for thrust measurement

Parameter	Value	Units
Total length, L	0.14	m
Offset from end, x	0.015	m
Outer diameter, d_o	0.013	m
Inner diameter, d_i	0.010	m
Young's modulus, E	3×10^9	N/m^2
Poisson's ratio, v	0.35	
Gauge factor, K	2	

Assuming a thrust of F_T of 0.1 N is applied to the cantilever, the axial strain ε_x is calculated by rearranging equation 5.5:

$$\varepsilon_x = \frac{F_T(L-x)y}{I_{yy}E} = -\frac{(0.1)(0.14-0.015)(-0.0065)}{(\pi/64)(0.013^4-0.01^4)(3\times10^9)} \tag{C.2}$$

$$= 2.973\times10^{-5} \text{ m/m}$$

Thus, for a thrust of 0.1 N the expected strain would be 29.73 μm/m. Substituting this value into equation C.1 gives the output voltage from the strain gauge bridge for an input of voltage of 1 V:

$$V_{out} = (1)\frac{2}{2}2.973\times10^{-5} = 2.973\times10^{-5} \text{ V} \tag{C.3}$$

Since the output voltage is a linear function of thrust, it can be said that for a thrust of 1 N, the expected output voltage would be equal to 297.3 μV. The calibration signal on the bridge amplifier allows the user to set the calibration signal for a 1 mV/V change over the bridge. A V_{out} of 297.3 μV corresponds to a thrust of 1 N. Thus, for a linear relationship the thrust corresponding to an output over the bridge of 1 mV would be:

$$F_{T\_1mV/V} = \frac{1000}{297.3}\times1 = 3.364 \text{ N} \tag{C.4}$$

A gain of 1000 was used to provide higher output voltage from the bridge amplifier to ensure better accuracy and resolution during data sampling. Hence, when the output calibration signal is activated to 3.364 V, the output voltage of the bridge amplifier in V will be the value of the thrust in N. This was checked by setting the calibration signal to 3.364 V and hanging 5, 10 and 20 gram mass pieces from the thrust arm and recording the output voltage. The results for this experiment can be found in Table C.2 which gives the measured output voltage as well as the theoretical output voltage for the various loads applied. The last column lists the percentage error relative to the theoretical results.

Table C.2 Theoretically and experimentally meausured outputs for thrust

Mass [kg]	Theoretical [V]	Measured [V]	% Error
0.005	0.049	0.042	-14.3
0.01	0.098	0.085	-13.3
0.02	0.196	0.165	-15.8

C.2 Theoretical Pressure Calibration for Storage Tank

In this section the value to which the calibration signal on the bridge amplifier must be set to for pressure measurement on the storage tank is calculated using the theory presented in section 6.2.3.1.

From equation 6.3 the expression for the ratio of output to input voltage in terms of the axial strain ε_x and gauge factor K is

$$\frac{V_{out}}{V_{in}} = \frac{K}{2}\left[\varepsilon_\theta - \varepsilon_x\right] \tag{C.5}$$

The axial and hoop strains ε_x and ε_θ can be expressed in terms of the axial, hoop and radial stresses σ_x, σ_θ and σ_r from stress-strain relationships as follows (Benham et al., 1999):

$$\varepsilon_x = \frac{\sigma_x}{E} - \frac{\nu}{E}\left(\sigma_r + \sigma_\theta\right) \tag{C.6}$$

$$\varepsilon_\theta = \frac{\sigma_\theta}{E} - \frac{\nu}{E}\left(\sigma_x + \sigma_r\right) \tag{C.7}$$

The expressions for the axial, hoop and radial stresses (σ_x, σ_θ and σ_r) are obtained from thick-walled cylinder theory (Benham et al., 1999). The expressions for the stresses on the outer wall of the cylinder are:

$$\sigma_x = \frac{p_i r_i^2 - p_o r_o^2}{r_o^2 - r_i^2} \tag{C.8}$$

$$\sigma_\theta = \frac{p_i r_i^2 - p_o r_o^2}{r_o^2 - r_i^2} + \frac{\left(p_i - p_o\right) r_i^2 r_o^2}{r_o^2\left(r_o^2 - r_i^2\right)} \tag{C.9}$$

$$\sigma_r = \frac{p_i r_i^2 - p_o r_o^2}{r_o^2 - r_i^2} - \frac{\left(p_i - p_o\right) r_i^2 r_o^2}{r_o^2\left(r_o^2 - r_i^2\right)} \tag{C.10}$$

The values required for computation of stresses, strains and output voltage for the storage tank are given in Table C.3.

Table C.3 Parameters for storage tank pressure strain calculation

Parameter	Value	Units
Outer radius, r_o	0.025	m
Inner radius, r_i	0.020	m
Young's modulus, E	3×10^9	N/m^2
Poisson's ratio, v	0.35	
Gauge factor, K	2	

Assuming an internal pressure p_i of 500 kPa and an outer pressure p_o equal to the environmental pressure of 100 kPa, the stresses can be calculated using equations C.8, C.9 and C.10:

$$\sigma_x = \frac{(500)(0.02)^2 - (100)(0.025)^2}{0.025^2 - 0.020^2} = 611.11 \text{ kPa} \tag{C.11}$$

$$\sigma_\theta = \frac{(500)(0.02)^2 - (100)(0.025)^2}{0.025^2 - 0.020^2} + \frac{(400)(0.020)^2 (0.025)^2}{0.025^2 \left(0.025^2 - 0.020^2\right)} \tag{C.12}$$

$$= 1322.22 \text{ kPa}$$

$$\sigma_r = \frac{(500)(0.020)^2 - (100)(0.025)^2}{0.025^2 - 0.020^2} - \frac{(400)(0.020)^2 (0.025)^2}{0.025^2 \left(0.025^2 - 0.020^2\right)} \tag{C.13}$$

$$= -100 \text{ kPa}$$

Substituting the stresses calculated in equations C.11 to C.13 into the stress-strain relationships of equations C.6 and C.7 gives the axial and hoop strains:

$$\varepsilon_x = \frac{611.11\times10^3}{3\times10^9} - \frac{0.35}{3\times10^9}\left(-100\times10^3 + 1322.22\times10^3\right) \tag{C.14}$$

$$= 61.14\times10^{-6} \text{ m/m}$$

$$\varepsilon_\theta = \frac{1322.22\times10^3}{3\times10^9} - \frac{0.35}{3\times10^9}\left(611.11\times10^9 + \left(-100\times10^3\right)\right) \tag{C.15}$$

$$= 381.05\times10^{-6} \text{ m/m}$$

Substituting the values of axial and hoop strain calculated in equations C.14 and C.15 into equation C.5 gives the output voltage from the strain gauge bridge for an input voltage of 1 V over the bridge:

$$V_{out} = (1)\frac{2}{2}\left(381.05\times10^{-6} - 61.14\times10^{-6}\right) = 320.0 \ \mu\text{V}$$

The calibration signal on the bridge amplifier allows the user to set the calibration signal for a 1 mV/V change over the bridge. A V_{out} of 320.0 μV corresponds to a

pressure of 500 kPa. Thus, for linear relationship the pressure corresponding to an output over the bridge of 1 mV would be

$$p_{1mV/V} = \frac{1000}{320} \times 500 = 1563 \text{ kPa} = 1.563 \text{ MPa} \quad \text{(C.16)}$$

Thus, when the calibration signal is set to 1.563 V and the gain is set to 1000, the output voltage V_{out} from the bridge amplifier will be the value of the absolute internal pressure in MPa. This was investigated by using this calibration to measure the pressure in the storage tank and comparing it to the pressure measured simultaneously using a pressure transducer. Figure C.1 is a plot of the pressure measured using both the pressure transducer and the strain gauge. The pressure measured using the strain gauge is plotted on both x and y axes. Curves showing the pressure measured using the pressure transducer and the strain gauge bridge are shown. It can be seen that the strain gauge pressure measurements are fairly accurate and the absolute value of the error increases linearly with pressure. The maximum difference is at 300 kPa, where the pressure measured using the strain gauges is approximately 10 % less than that measured using the pressure transducer.

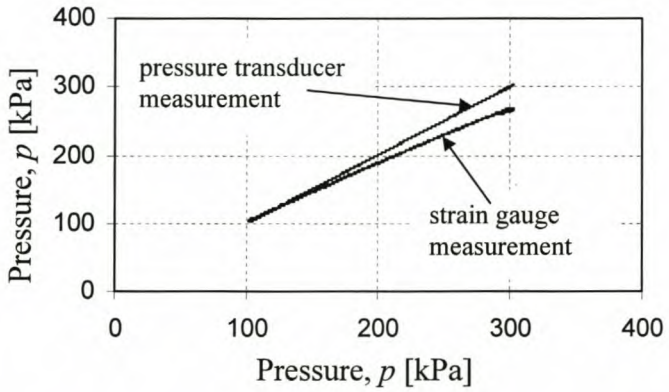

Figure C.1 Strain gauge against transducer pressure measurement for storage tank

C.3 Theoretical Pressure Calibration of Accumulator

In this section the value to which the calibration signal on the bridge amplifier must be set to for pressure measurement on the accumulator is calculated using the theory presented in section 6.2.3.1.

From equation 6.3 the expression for the ratio of output to input voltage in terms of the axial strain ε_x and gauge factor K is:

$$\frac{V_{out}}{V_{in}} = \frac{K}{2}\left[\varepsilon_\theta - \varepsilon_x\right] \tag{C.17}$$

The expressions for axial and hoop strains ε_x and ε_θ were given in equation C.6 and C.7. The expressions for the axial, hoop and radial stresses necessary to determine the strains were given in equations C.8 to C.10.

The values required for computation of stresses, strains and output voltage for the storage tank are given in Table C.4.

Table C.4 Parameters for accumulator pressure strain calculation

Parameter	Value	Units
Outer radius, r_o	0.013	m
Inner radius, r_i	0.010	m
Young's modulus, E	3×10^9o	N/m^2
Poisson's ratio, v	0.35	
Gauge factor, K	2	

Assuming an internal pressure p_i of 500 kPa and an outer pressure p_o equal to the environmental pressure of 100 kPa, the axial, hoop and radial stresses can be calculated using equations C.8, C.9 and C.10 and the values listed in Table C.4:

$$\sigma_x = \frac{(500)(0.005)^2 - (100)(0.0065)^2}{0.0065^2 - 0.005^2} = 479.71 \text{ kPa} \tag{C.18}$$

$$\sigma_\theta = \frac{(500)(0.005)^2 - (100)(0.0065)^2}{0.0065^2 - 0.005^2} + \frac{(400)(0.005)^2\,(0.0065)^2}{0.0065^2\left(0.0065^2 - 0.005^2\right)} \tag{C.19}$$

$$= 1059.42 \text{ kPa}$$

$$\sigma_r = \frac{(500)(0.020)^2 - (100)(0.025)^2}{0.025^2 - 0.020^2} - \frac{(400)(0.020)^2\,(0.025)^2}{0.025^2\left(0.025^2 - 0.020^2\right)} \tag{C.20}$$

$$= -100 \text{ kPa}$$

Substituting the stresses calculated in equations C.18 to C.20 into the stress-strain relationships of equations C.6 and C.7 gives the axial and hoop strains:

$$\varepsilon_x = \frac{479.71\times10^3}{3\times10^9} - \frac{0.35}{3\times10^9}\left(-100\times10^3 + 1059.42\times10^3\right) \tag{C.21}$$
$$= 47.97\times10^{-6} \text{ m/m}$$

$$\varepsilon_\theta = \frac{1059.42\times10^3}{3\times10^9} - \frac{0.35}{3\times10^9}\left(479.91\times10^3 + \left(-100\times10^3\right)\right) \qquad \text{(C.22)}$$
$$= 308.84\times10^{-6} \text{ m/m}$$

Substituting the values of axial and hoop strain calculated in equations C.21 and C.22 into equation C.17 gives the output voltage from the strain gauge bridge for an input voltage of 1 V over the bridge:

$$V_{out} = (1)\frac{2}{2}\left(308.42\times10^{-6} - 47.97\times10^{-6}\right) = 260.87 \text{ μV} \qquad \text{(C.23)}$$

The calibration signal on the bridge amplifier allows the user to set the calibration signal for a 1 mV/V change over the bridge. A V_{out} of 260.87 μV corresponds to a pressure of 500 kPa. Thus, for linear relationship the pressure corresponding to an output over the bridge of 1 mV would be:

$$p_{1mV/V} = \frac{1000}{260.87}\times500 = 1917 \text{ kPa} = 1.917 \text{ MPa} \qquad \text{(C.24)}$$

Thus, when the calibration signal is set to 1.917 V and the gain is set to 1000, the output voltage V_{out} from the bridge amplifier will be the value of the absolute internal pressure in MPa. This was investigated by using this calibration to measure the pressure in the storage tank and comparing it to the pressure measured simultaneously using a pressure transducer. Figure C.2 is a plot of the pressure measured using both the pressure transducer and the strain gauge. The pressure measured using the strain gauge is plotted on both x and y axes. Curves showing the pressure measured using the pressure gauge and the strain gauge bridge are shown. It can be seen that the strain gauge pressure measurements are fairly accurate and the absolute value of the error increases linearly with pressure. The maximum difference is at 300 kPa, where the pressure measured using the strain gauges is approximately 10 % less than that measured using the pressure transducer. This behaviour is virtually identical to that of the storage tank.

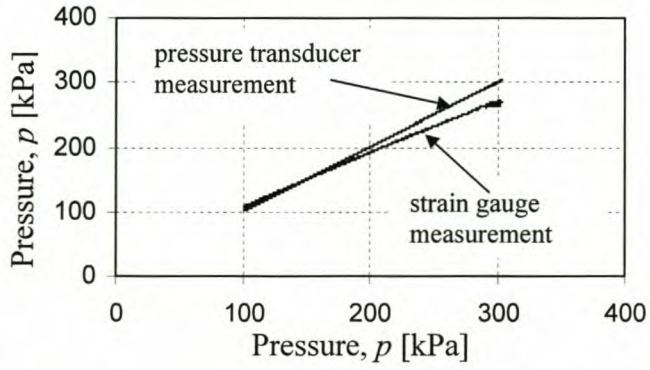

Figure C.2 Strain gauge versus transducer pressure measurement for accumulator

APPENDIX D: LABVIEW PROGRAM STRUCTURE

It was mentioned in section 6.2 that the software package *LabVIEW 6.1* was used for controlling the solenoid valves and for sampling the data from the bridge amplifier. In this section a brief overview of the program written for this task is given.

Ideally, when it is required to simultaneously control and sample (where the control and sampling are independent of each other, i.e. not a feedback system), it would be preferable to run two independent procedures – one for control and one for sampling. An illustration of this scenario is illustrated in Figure D.1

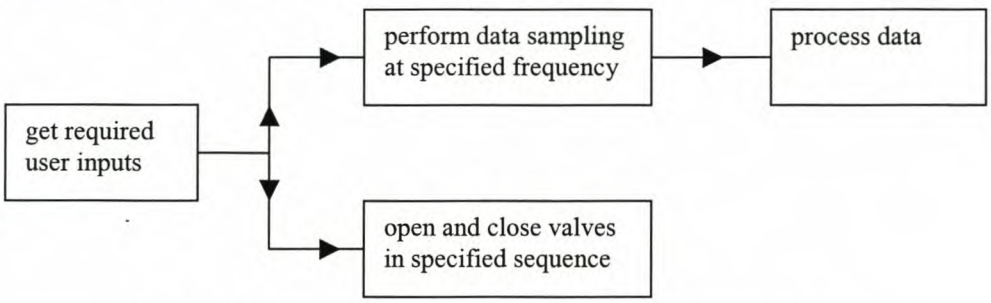

Figure D.1 Idealised scenario for control and sampling

This scenario would make it possible to sample at a high frequency (typically 10 kHz) on the computer used. However, the ability to run two procedures simultaneously was not available in *LabVIEW* as the program would first complete the first procedure before starting on the second one. Hence, it was necessary to make use of a *for* loop containing the necessary commands for sampling and control. Every time the loop is run one sample is obtained from each input channel and a procedure is run to decide what the valve states must be and to switch the valves on or off if necessary (the algorithm for deciding when to open and close valves can be found in section E.3.) The timing is controlled by employing a timer function that allows the user to specify the wait interval between each execution of the loop. The time specified must be a integer value in milliseconds. Thus, the shortest possible wait interval is 1 ms. Therefore, the fastest possible sampling frequency (irrespective of computer and DAQ card ability) is 1 kHz. However, if the commands in the for loop require more time to be executed than that specified for the wait interval, then the actual sampling speed will be slower than that specified. It was determined experimentally that the

fastest sampling speed that could be obtained on the computer used was 50 Hz. A flow chart of the program developed for control and sampling is given in Figure D.2.

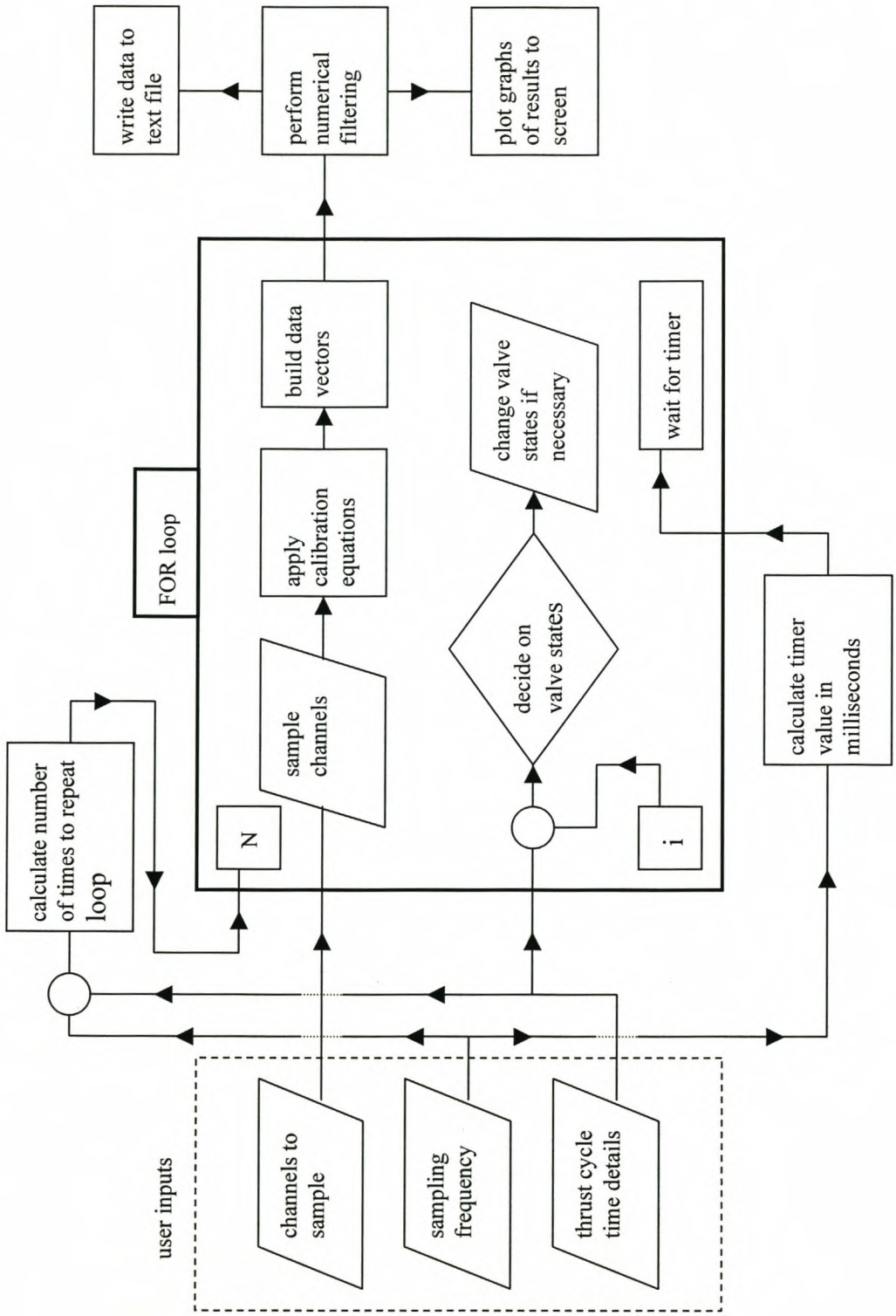

Figure D.2 Flowchart of LabVIEW program

APPENDIX E: SELECTED ALGORITHMS

E.1 One-Dimensional Transient Explicit Simulation

This algorithm is for the explicit numerical simulation of a one-dimensional transient system discussed in section 4.1:

For j = 1 to (Total_Time / Δt)

$time = j * \Delta t$

{determine the following properties using "old" values:}
$\rightarrow \dot{m}_W$, $\dot{m}_E$, $\dot{E}_W$, $\dot{E}_E$ @ old values

{determine the "new" values for mass and energy:}

$$m_i^{new} = m_i^{old} + \left(\dot{m}_W - \dot{m}_E\right)\Delta t$$
$$E_i^{new} = E_i^{old} + \left(\dot{E}_W - \dot{E}_E\right)\Delta t$$

{set "new" values to "old" for next time step:}
$$m_i^{old} = m_i^{old}$$
$$E_i^{old} = E_i^{new}$$

End For

E.2 Solution to Beam Vibration Equation

The following are the Matlab routines used for the solution of the equation describing the vibration of the cantilevered beam used to measure thrust (equation 5.28 in section 5.21). The program *freq.m* was used to call function *dd.m*. *Freq.m* runs through a for loop in a range of values of β (refer equation 5.29) specified by the user. For each value of β the function *dd.m* determines the value of the determinant of the matrix **A** in equation 5.28 and 5.29. This allows the user to iteratively solve for the value of be that gives a value of the determinant of **A** close enough to zero.

Code for freq.m:

```
%Program name: freq.m
%Function to determine the natural vibration frequencies of cantilever beam
clear all;
for ii = 1:1001
        x(ii) = (ii-1) * 0.001;
        z(ii) = dd(x(ii));
end

plot(x,z,'red')
```

Code for dd.m:

```
function y = dd(beta)
%function to evaluate determinant of matrix
L = 0.125;
m = 0.18;
rho = 1.2;
A = 3.14159 * 0.25 * (0.013^2 - 0.01^2);
D = m*beta/(rho * A);
BL = beta * L;
col_1 = [0 beta -beta^2*sin(BL) (-cos(BL)+ D*sin(BL))]';
col_2 = [1 0 -beta^2*cos(BL) (sin(BL)+D*cos(BL))]';
col_3 = [0 beta beta^2*sinh(BL) (cosh(BL) + D*sinh(BL))]';
col_4 = [1 0 beta^2 * cosh(BL) (sinh(BL) + D * cosh(BL))]';

A = [col_1 col_2 col_3 col_4];
y = det(A);
```

E.3 Algorithm for Valve Control in LabVIEW

The structure of the LabVIEW program used for control of the valves and data sampling was given in Appendix D. It was necessary to introduce a section of code into the "for" loop of the program to decide whether the valve should be opened or closed. This code had to be in programmed in C. This code made use of the following algorithm:

Algorithm for Pulsed Thrust Control

User inputs:

f	-	sampling frequency [Hz]
no_cylces	-	number of cycles
thrust_time	-	thrust time [s] (Δt_{on})
int_time	-	time interval between thrusts [s] (Δt_{off})
v1_wait_start	-	wait time before opening valve 1 [s]
v1_wait_end	-	time for sampling to continue after valve 1 closed [s]
v0_wait_start	-	wait time before first opening of valve 0 [s]
v0_wait_end	-	time to continue sampling after last cycle completed [s]

Description of variables used in program:

t	-	time elapsed [ms]
cycle_time	-	time required for one cycle [ms] (Δt_{cycle})
dt	-	time interval between sampling [ms]
total_time	-	total time for which sampling occurs [ms]
i	-	counter
N	-	number of times for loop must be completed
cycle_count	-	records number of cycles completed

Algorithm

Get user inputs:
f, no_cycles, thrust_time, int_time, v1_wait_start, v1_wait_end,
v0_wait_start, v0_waitF_end

//convert values in seconds to milliseconds:
thrust_time = thrust_time * 1000
int_time = int_time * 1000
v1_wait_start = v1_wait_start * 1000
v1_wait_end = v1_wait_end * 1000
v0_wait_start = v0_wait_start *1000
v0_wait_end = v0_wait_end * 1000

//calculate values of constants for program
cycle_time = thrust_time + int_time

```
total_time = v0_wait_start + (no_cycles * cycle_time) + v0_wait_end
dt = 1000 / f
N = total_time / dt + 1
cycle_count = 0
t = 0

FOR i = 0 to N

        IF v1_wait_start <= t <= total_time – v1_wait_end THEN
                OPEN valve 1
        ELSE
                CLOSE valve 1
        END IF


        IF ((t-v0_wait_start – (cycle_time * cycle_count) <= thrust time )
           AND (t –v0_wait_end – (no_cycles * cycle_time <= 0)
           AND (v0_wait_start <= t <= total_time – v0_wait_end) THEN
                OPEN valve 0
        ELSE
                CLOSE valve 0
        END IF

        x = t – v0_wait_start – (cycle_count * cycle_time)

        IF (t – v0_wait_start – (cycle_count * cycle_time)) => cycle_count
                THEN
                cycle_count = cycle_count + 1
        ELSE
                cycle_count = cycle_count
        END IF

        t = i * dt

LOOP
```

APPENDIX F: PHOTOGRAPHS OF EXPERIMENTAL WORK

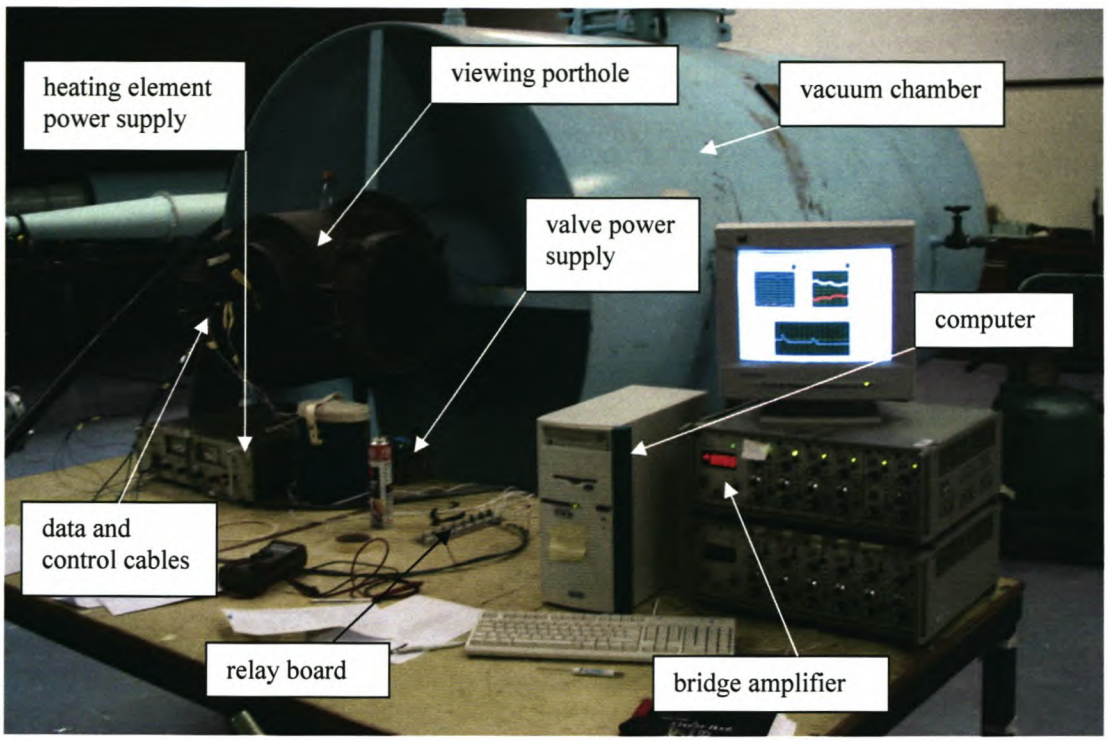

Figure F.1 View of measurement and control set-up

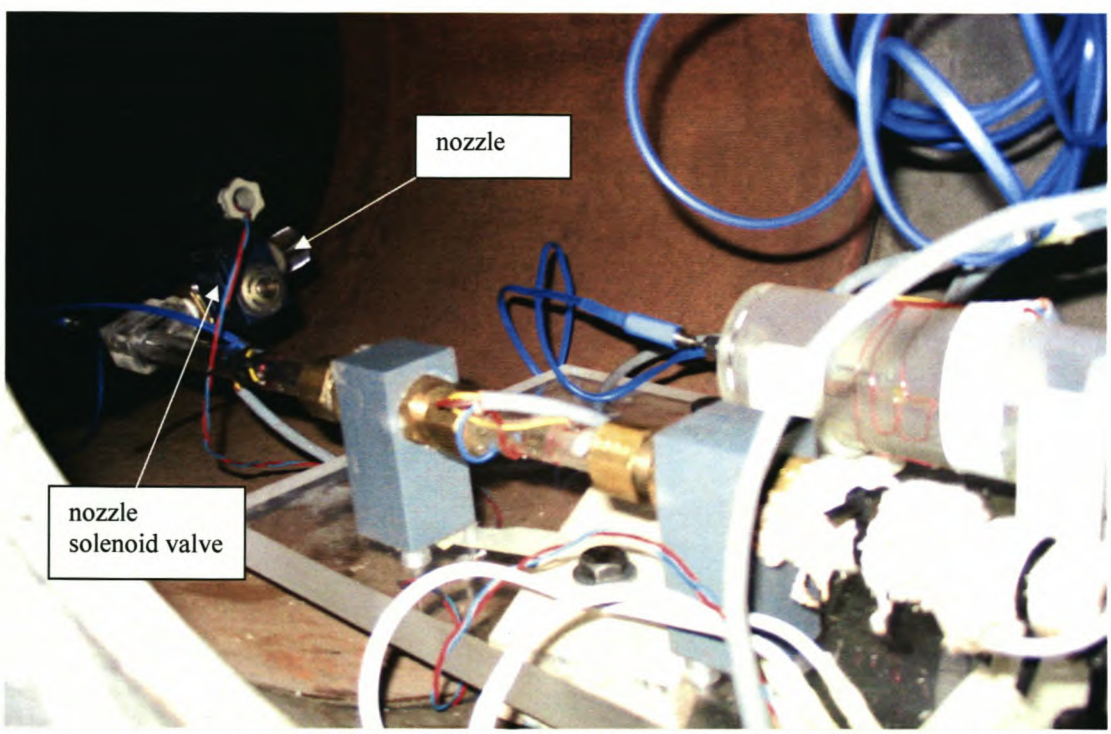

Figure F.2 Cantilevered thrust measurement arm and nozzle in vacuum chamber

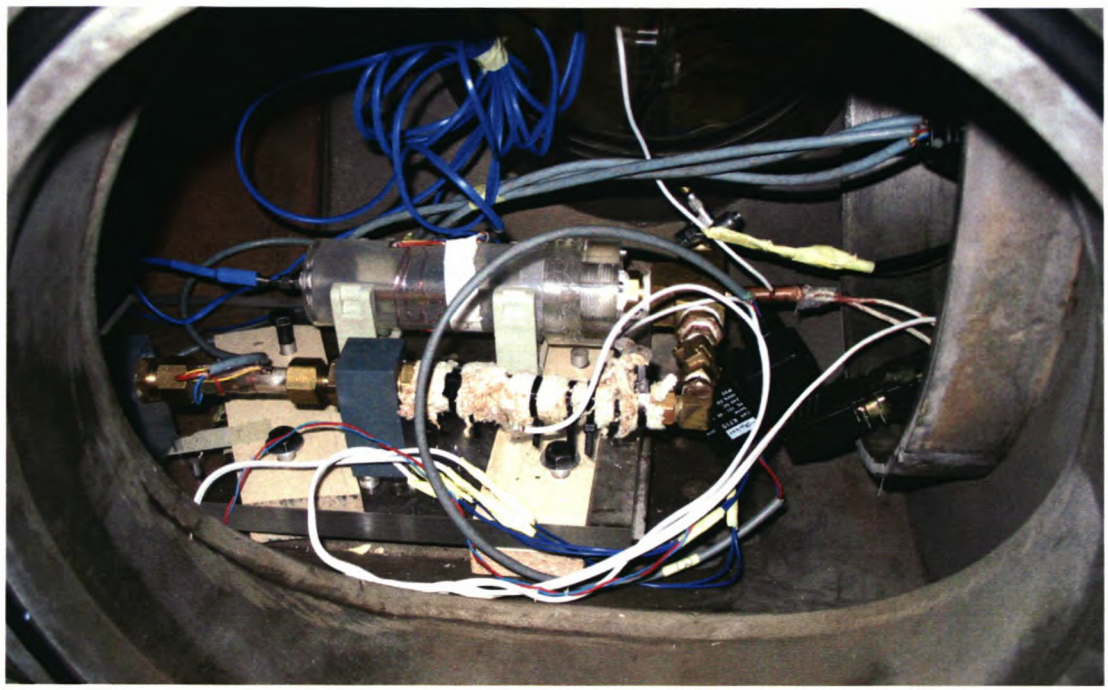

Figure F.3 Experimental model in vacuum chamber

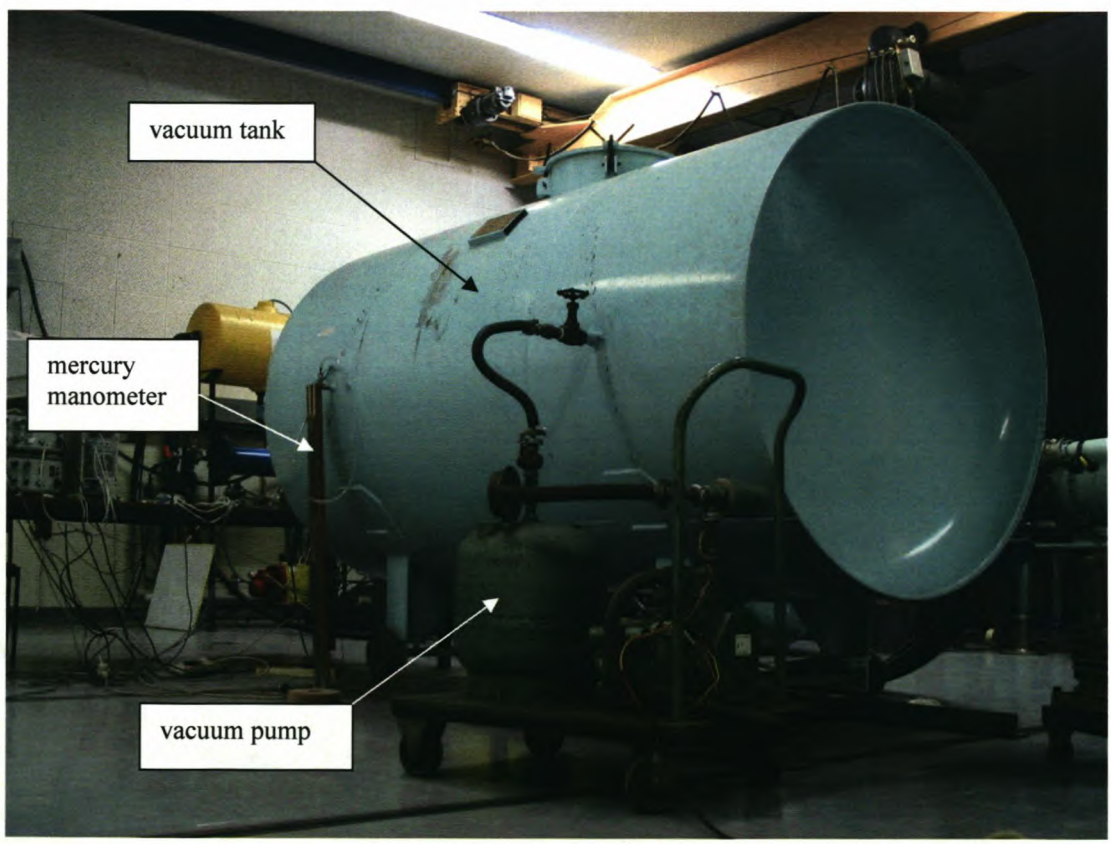

Figure F.4 Vacuum apparatus

Figure F.5 Preparing to perform a pressure test on the experimental model

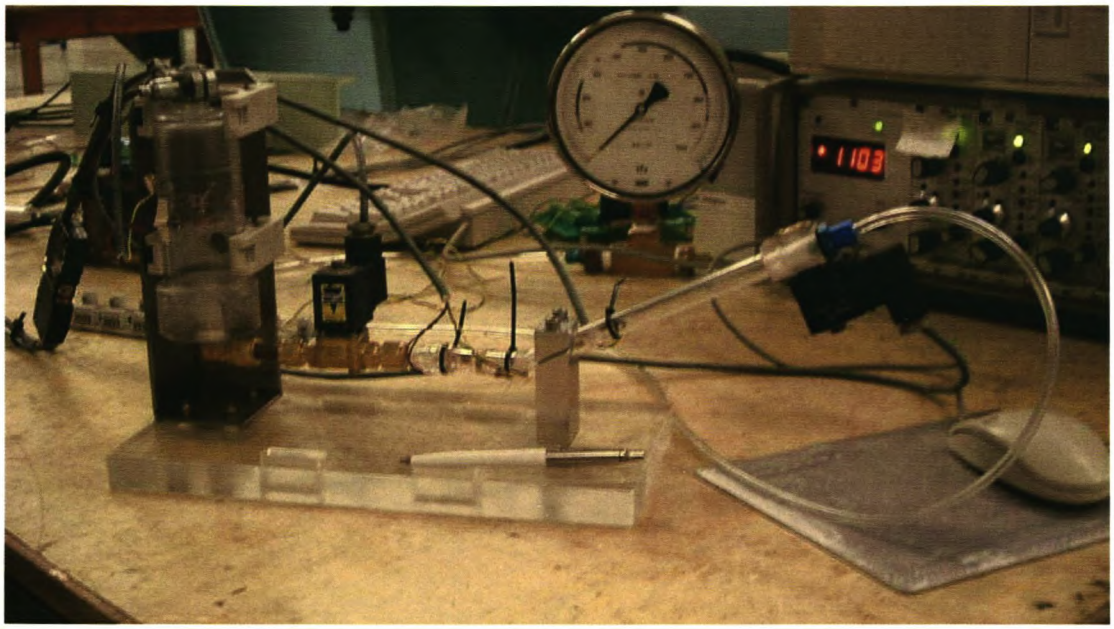

Figure F.6 Initial experimental model

APPENDIX G: EXPERIMENTAL CORRELATION DATA

Table G.1 gives the experimental data used to develop the experimental correlation discussed in section 7.4. The expression correlating average thrust $\overline{F}_T$ in terms of pulse duration Δt and initial pressure p was assumed to be given as:

$$\overline{F}_T = a(\Delta t)^b p^c \tag{G.1}$$

Taking natural logarithms on both sides of equation G.1:

$$\ln \overline{F}_T = \ln a + b \ln(\Delta t) + c \ln p \tag{G.2}$$

Thus, the natural logarithms of the data in Table G.1 were taken and a regression analysis performed. The regression analysis yielded the *intercept coefficient* (equal to ln a), as well as two *X variable coefficients* (equal to b and c). Hence, the regression analysis yielded the values of b and c directly. The value of a was calculated as follows:

$$a = e^{intercept\ coefficient} \tag{G.3}$$

Table G.1 Experimental data points used for correlation

Thrust time [s]	Initial pressure [kPa]	Average thrust [N]
2	250	0.025
2	260	0.019
2	200	0.022
2	280	0.058
2	260	0.033
3	380	0.055
3	380	0.040
3	310	0.023
3	330	0.028
5	255	0.030
5	210	0.020
5	180	0.010
5	210	0.021
5	200	0.020
15	190	0.020
15	200	0.023

APPENDIX H: ENGINEERING DRAWINGS

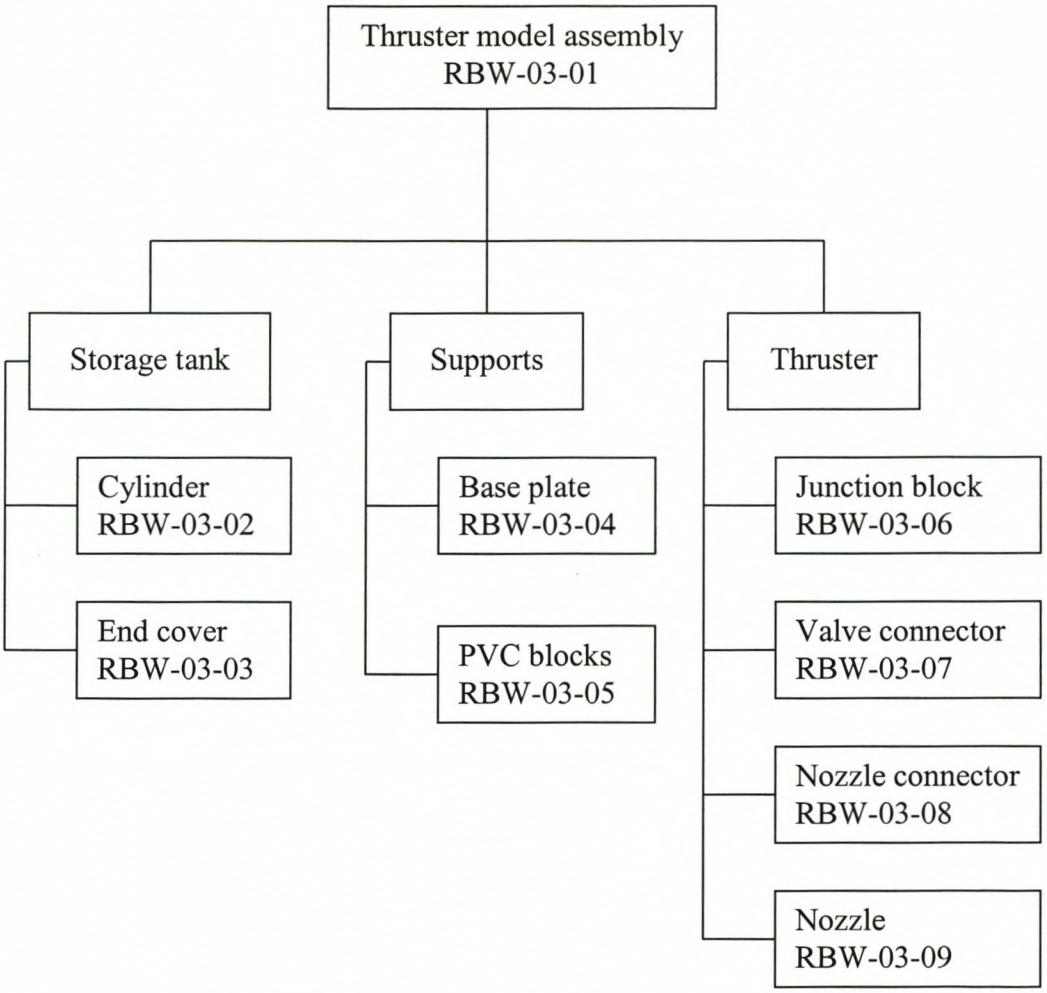

Figure H.1 Drawing tree

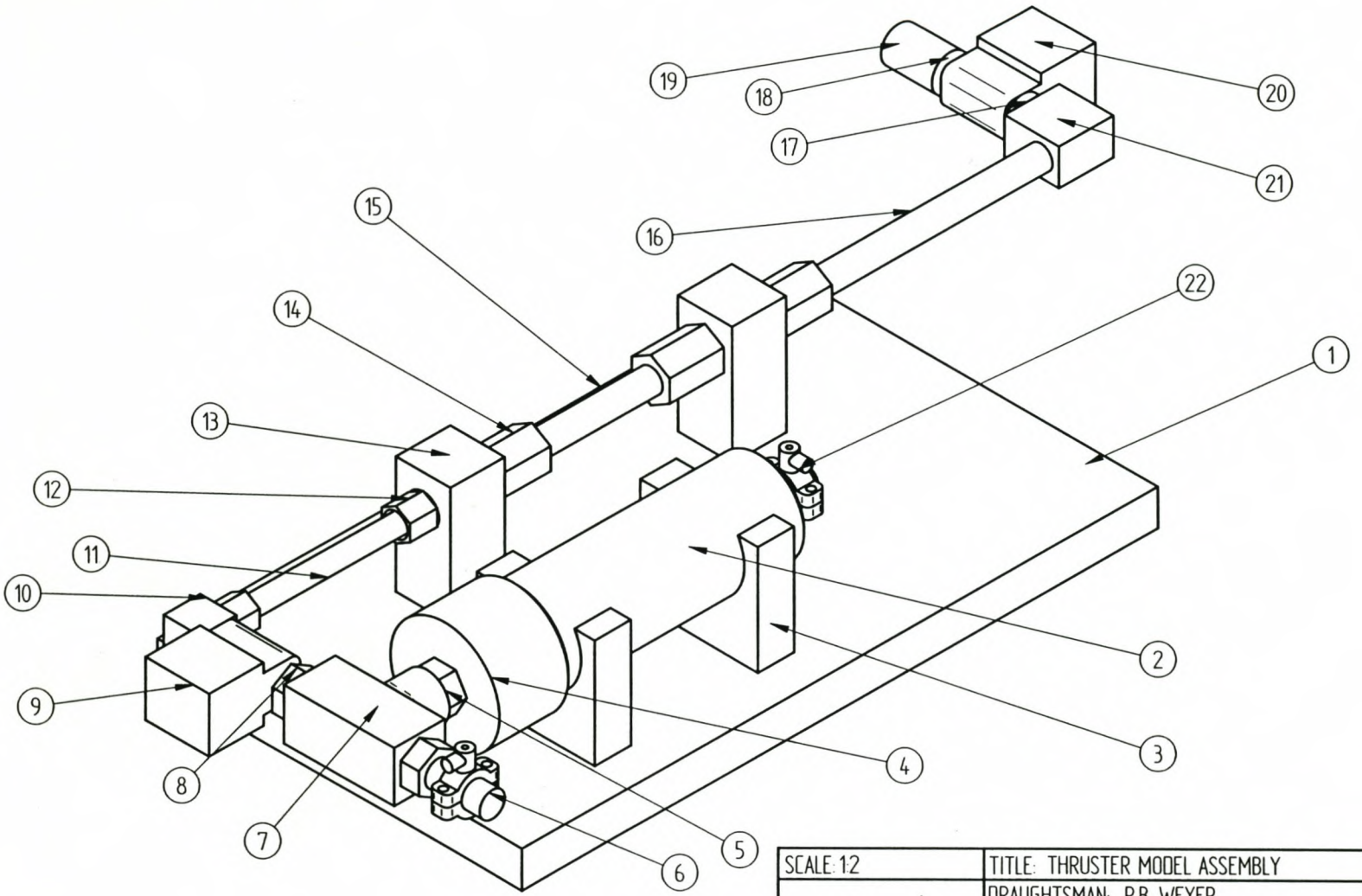

SCALE: 1:2	TITLE: THRUSTER MODEL ASSEMBLY	
	DRAUGHTSMAN: R.B. WEYER	
	MATERIAL:	DATE: 24/06/2003
	DIMENSIONS IN: mm	DWG No.: RBW-03-01

Table H.1 Parts list for assembly drawing (RBW-03-01)

Item	Description	No. Of	Remarks
1	Base plate	1	RBW-03-04
2	Cylinder	1	Ref dwg RBW-03-02
3	50 mm PVC clamps	2	
4	End cover	1	Ref dwg RBW-03-03
5	Male nipple fitting	1	½" BSPT
6	Butt weld connector	1	½" BSPT to OD 15 mm
7	Female tee-piece	1	½" BSP
8	Taper male connector	1	½" BSPT to 3/8" BSPP
9	Ø2.8 mm solenoid valve	1	Parker VE 131 – VE 161
10	Elbow	1	Male 3/8" BSPP to 3/8" pipe
11	Copper tube	1	Ø3/8" x 110
12	BSP Taper male connecter	1	½" BSPT to 3/8" pipe
13	PVC block	2	Ref dwg RBW-03-05
14	BSP Taper male connector	3	½" BSPT to ½" pipe
15	Perspex tube	1	13 OD x 10 ID x 80
16	Perspex tube	1	13 OC x 10 IC x 140
17	Valve connector	1	Ref dwg RBW-03-07
18	Nozzle connector	1	Ref dwg RBW-03-08
19	Nozzle	1	Ref dwg RBW-03-09
20	Ø1.6 mm solenoid valve	1	Sirai Z610A
21	Junction block	1	Ref dwg RBW-03-06
22	Fill valve	2	Quik-tap QT-2

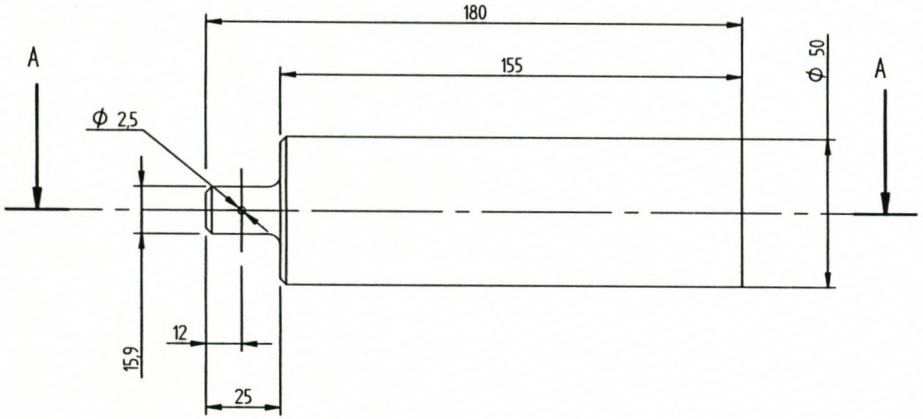

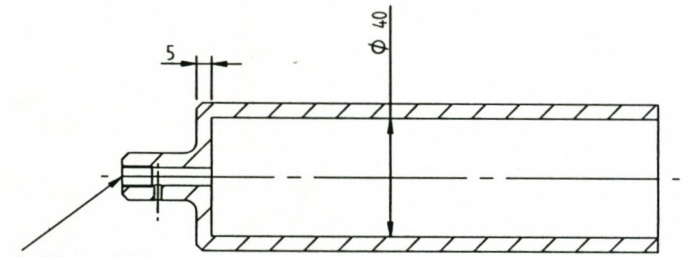

SECTION A-A

ALL CHAMFER 2x45°
ALL FILLET R4

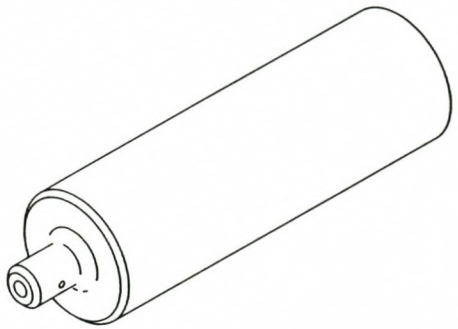

SCALE: 1:2	TITLE: CYLINDER	
	DRAUGHTSMAN: R.B. WEYER	
	MATERIAL: PERSPEX	DATE: 24/06/2003
	DIMENSIONS IN: mm	DWG No.: RBW-03-02

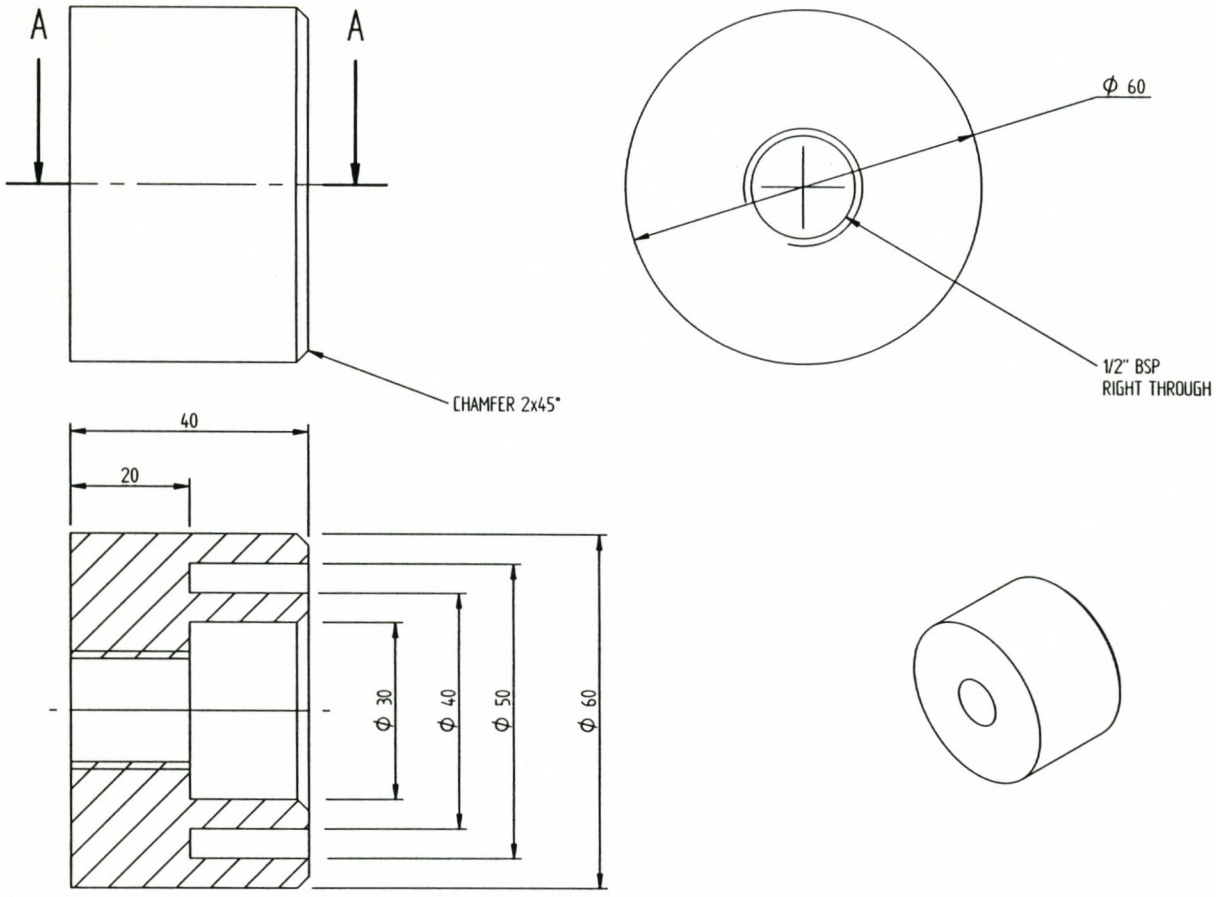

SECTION A-A

SCALE: 2:1	TITLE: END COVER	
	DRAUGHTSMAN: R.B. WEYER	
	MATERIAL: PERSPEX	DATE: 24/06/2003
	DIMENSIONS IN: mm	DWG No.: RBW-03-03

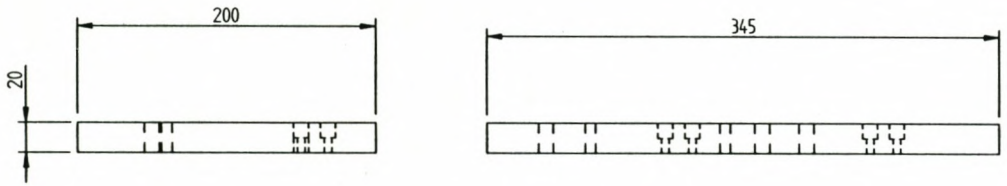

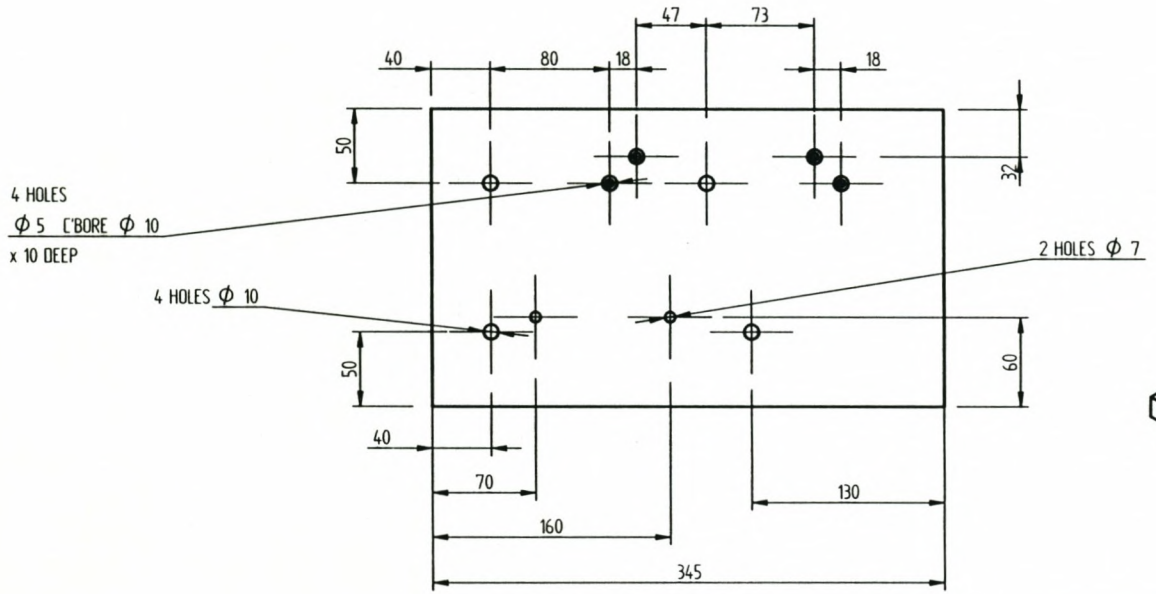

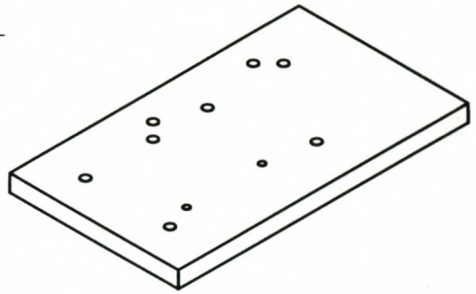

SCALE: 1:5	TITLE: BASE PLATE	
	DRAUGHTSMAN: R.B. WEYER	
	MATERIAL: PERSPEX	DATE: 24/06/2003
	DIMENSIONS IN: mm	DWG No.: RBW-03-04

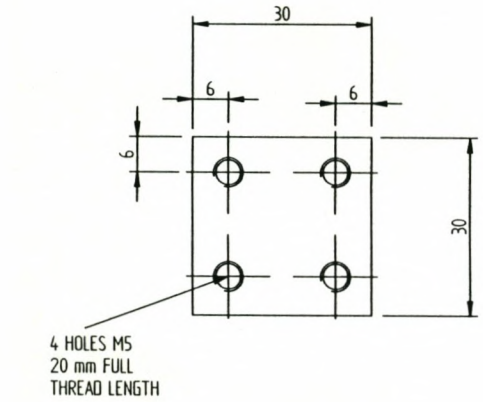

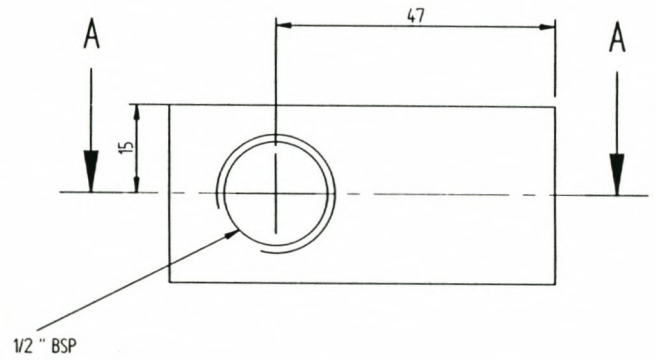

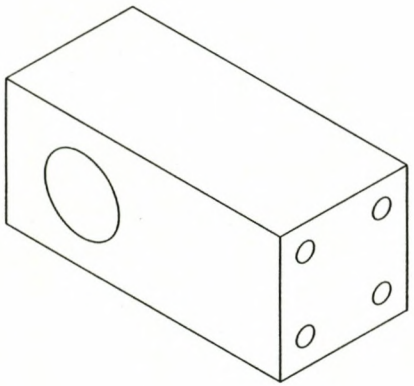

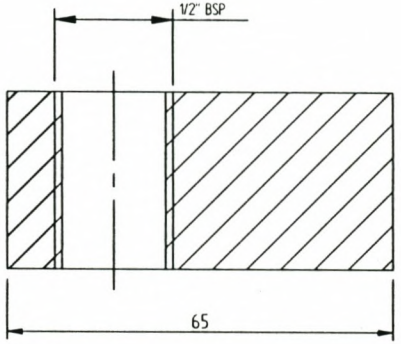

SECTION A-A

SCALE: 1:1	TITLE: PVC BLOCK	
	DRAUGHTSMAN: R.B. WEYER	
	MATERIAL: PVC	DATE: 24/06/2003
	DIMENSIONS IN: mm	DWG No.: RBW-03-05

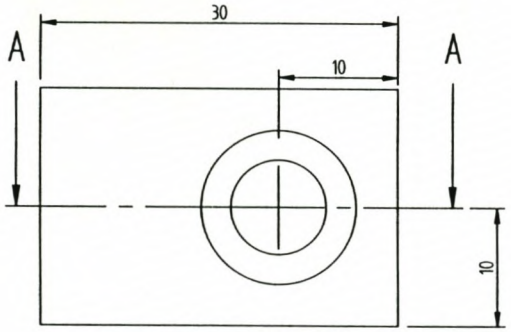

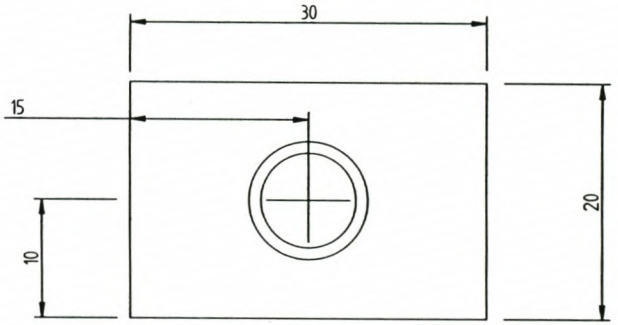

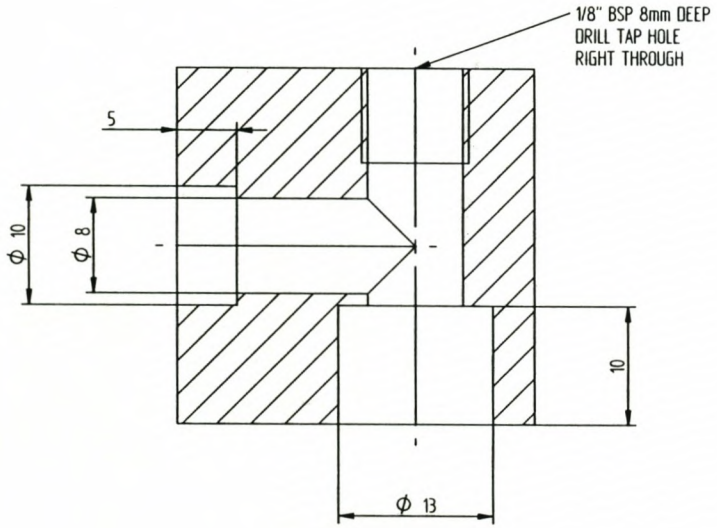

SECTION A-A

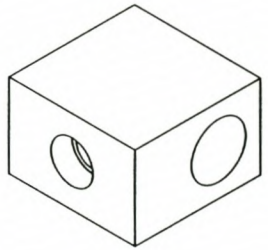

SCALE: 2:1	TITLE: JUNCTION BLOCK	
	DRAUGHTSMAN: R.B. WEYER	
	MATERIAL: PERSPEX	DATE: 24/06/2003
	DIMENSIONS IN: mm	DWG No.: RBW-03-06

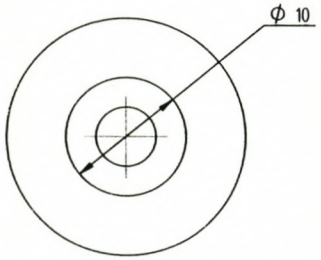

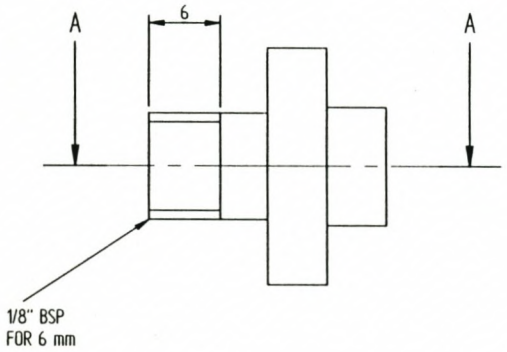

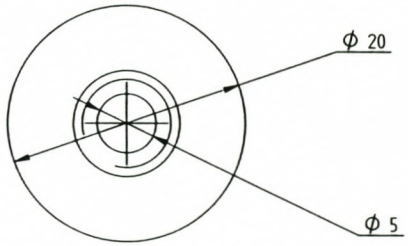

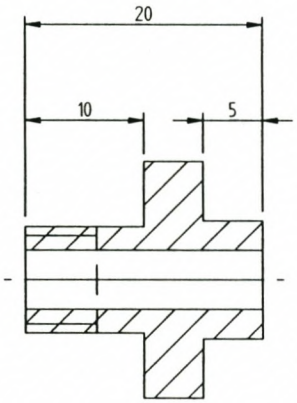

SECTION A-A

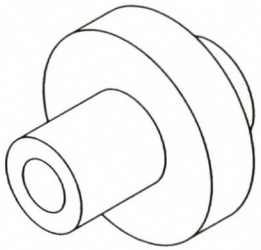

SCALE: 2:1	TITLE: VALVE CONNECTOR	
	DRAUGHTSMAN: R.B. WEYER	
	MATERIAL: PERSPEX	DATE: 24/06/2003
	DIMENSIONS IN: mm	DWG No.: RBW-03-07

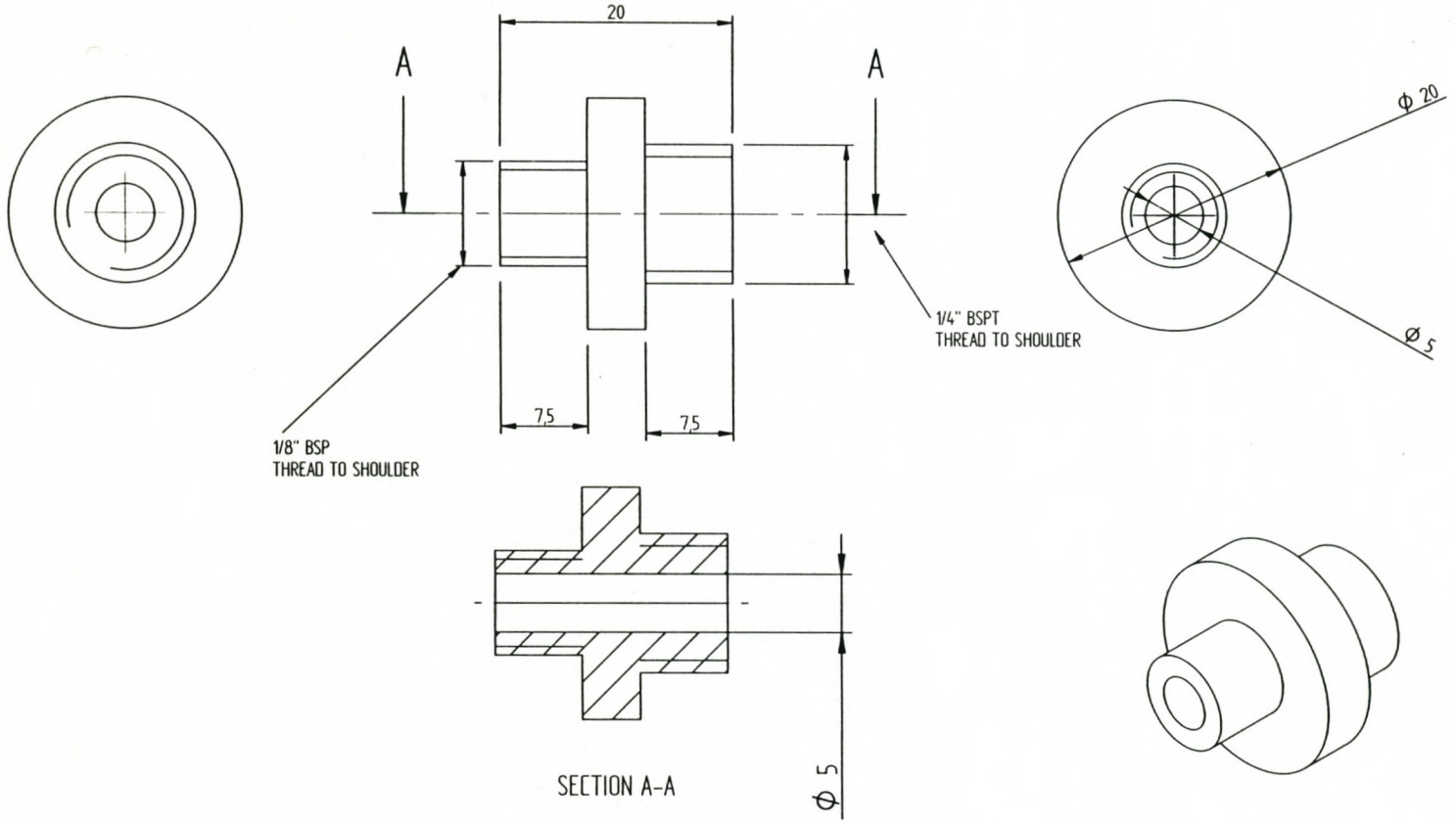

SCALE: 2:1	TITLE: NOZZLE CONNECTOR	
	DRAUGHTSMAN: R.B. WEYER	
	MATERIAL: PERSPEX	DATE: 24/06/2003
	DIMENSIONS IN: mm	DWG No.: RBW-03-08

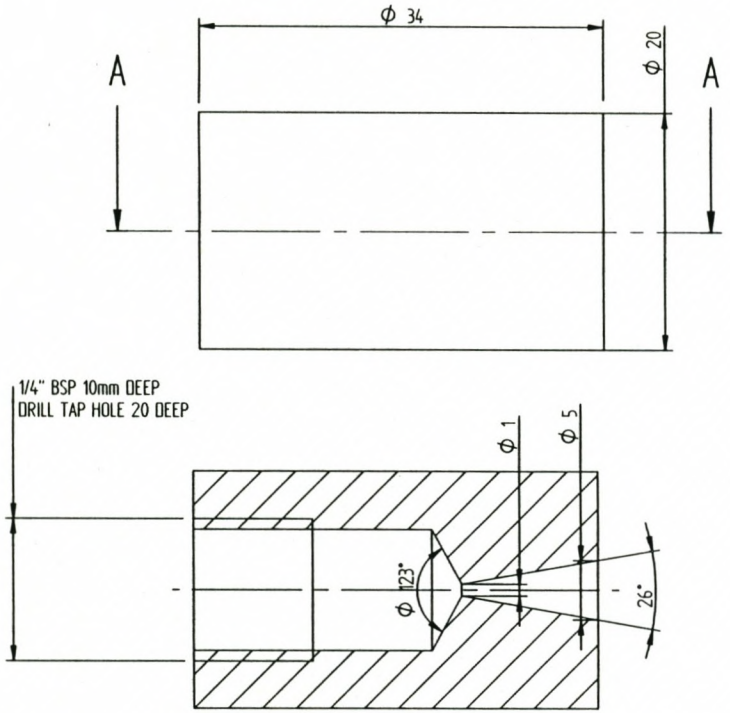

SECTION A-A

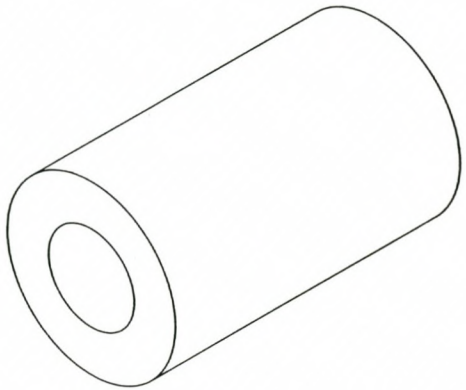

SCALE: 2:1	TITLE: NOZZLE	
	DRAUGHTSMAN: R.B. WEYER	
	MATERIAL: PERSPEX	DATE: 24/06/2003
	DIMENSIONS IN: mm	DWG No.: RBW-03-09